Quantitative Crystal Investigations: Surface Dissolution and Nucleation Processes

Alexander Stuart Parker

Thesis submitted for the degree of

Doctor of Philosophy

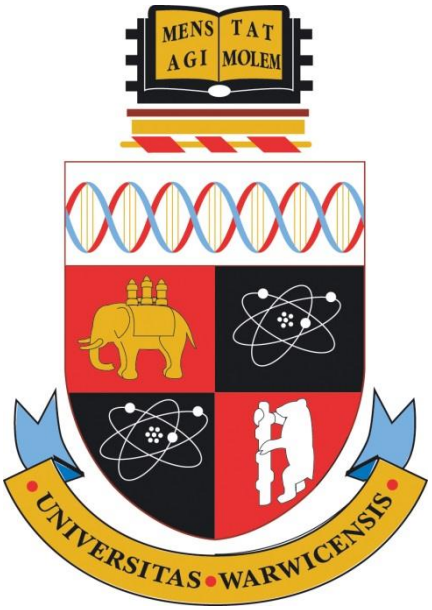

Electrochemistry and Interfaces Group,

Department of Chemistry,

University of Warwick.

June 2016

For my loving family

Quantitative Crystal Investigations: Surface Dissolution and Nucleation Processes

Alexander Stuart Parker

I. Table of Contents

II. List of figures

III. List of Tables

IV. Declaration and Inclusion of Published Work

This thesis is submitted to the University of Warwick in support of my application for the degree of Doctor of Philosophy. It has been composed by myself and has not been submitted in any previous application for any degree

Beyond general advice and guidance from my supervisor, the work presented (including data generated and data analysis) was carried out by the author except in the cases outlined below:

- The FEM model used in chapter 2 and 3 was based on that originally developed by Michael E. Snowden but was modified for the systems used in this work. Advice on FEM modelling was provided by Rehab Al Botros.
- Chapter 3 ICP-OES analysis was carried out by Anisha N. Patel
- Chapter 4 FEM modelling and analysis was carried out by David Perry and the program to calculate $T_{0.5}$ was written by Ashley Page.

Parts of this thesis have been published by the author:

Chapter 2

- Alexander S. Parker, Rehab Al Botros, Sophie Kinnear, Michael Snowden, Kim Mckelvey, Alexander Ashcroft, Mel Carvell, Andrew Joiner, Massimo Peruffo, Carole Philpotts, Patrick R. Unwin. *"Combinatorial Localized Dissolution Analysis: Application to Acid-induced Dissolution of Dental Enamel and the Effect of Surface Treatments"* *Journal of Colloid and interface Science* **2016** doi: http://dx.doi.org/10.1016/j.jcis.2016.05.018

Chapter 3

- Alexander S. Parker, Anisha N. Patel, Rehab Al Botros, Michael E. Snowden, Kim McKelvey, Patrick R. Unwin, Alexander T. Ashcroft, Mel Carvell, Andrew Joiner, Massimo Peruffo. "*Measurement of the efficacy of calcium silicate for the protection and repair of dental enamel*" *Journal of*

Dentistry 42(supplement 1) **2014** S21-S29. doi: http://dx.doi.org/10.1016/S0300-5712(14)50004-8

Chapter 4

Alexander S. Parker, David Perry, Ashley Page, Patrick R. Unwin *"Electrochemical control of calcium carbonate crystallization and dissolution in nanopipettes" ChemElectroChem* **2016** doi: 10.1002/celc.201600547

V. Acknowledgements

First and foremost, I would like to thank my supervisor Pat Unwin who has given me great support throughout my PhD and pushed me when I needed it. Thank you to the entire chemistry department for making my time here so pleasurable. Thanks to BrassSoc for giving me my musical release during my PhD and being such a great group of friends.

To Rachel, Thank you for keeping me on the straight and narrow with my head down on the ground. Without you, I would never have stayed the course.

I would also like to thank my grandparents who are my inspiration. To achieve a fraction of what they have and their love drives me on at my lowest points. Thank you both to those who have been here to give me the love and support to get me through, as well as those who I know would have been so proud so see me reach the end of this great journey and whose love I carry with me always.

Finally to my parents. Words can't express how much I want to thank you for getting me to this point through love and support, the extra handwriting, spelling and reading support (whilst not entirely successful) and of course hours and hours spell checking my work have meant my dyslexia has never been a barrier to me, something I'm incredibly proud of. But, more than that thanks for being at the end of the phone and being there whenever I needed you with your love.

VI. Definition of Acronyms

SECCM - scanning electrochemical cell microscope

AFM - atomic force microscopy

FEM - finite element method

NaF - sodium fluoride

$ZnCl_2$ - zinc chloride

SEM - scanning electron microscopy

SECCM - scanning electrochemical cell microscopy

$CaCO_3$ - calcium carbonate

SICM - scanning ion conductance microscope

ACC - amorphous calcium carbonate

TEM - transmission electron microscope

Cryo-TEM - cryo-transmission electron microscopy

SPM - scanning probe microscopy

STM - scanning tunnelling microscope

SECM - scanning electrochemical microscopy

DC - direct current

IC-SECM - intermittent contact SECM

FE-SEM - field emission scanning electron microscopy

PDE - partial differential equation

RD - rotating disk

AC - alternating current

QRCE - quasi reference counter electrode

HAP - hydroxy apatite ($Ca_{10}(PO_4)_6(OH)_2$)

FPGA - field programmable gate array

VII. Glossary of Symbols

λ - wavelength of light

NA - numerical aperture

d - distance limit

F - current force

l - deflection

k - spring constant

D - diffusion coefficient

Z - charge

m_w - meniscus contact width

m_h - meniscus height

E_f - fraction of the potential that falls across the simulation boundaries

p_h - pipette height

c - concentration

u_i - ionic mobility

F - Faraday constant

V - electric field

VIII. Abstract

The aim of this thesis is twofold with both elements related to industrially relevant crystal systems and processes. The first element utilized a combined scanning electrochemical cell microscope (SECCM) and atomic force microscopy (AFM) method to study the dissolution of enamel surfaces with controlled proton flux to the surface. This was then extended to investigate the effect of both known surface treatments, fluoride and zinc ions, but also a novel treatment of calcium silicate and its methods of action. The second element investigated the use of a nanopipette to investigate the early nucleation and initial growth of calcium carbonate crystals.

For the dissolution of enamel, an SECCM probe to selectively etch a surface for a defined period of time with a high spatial resolution was used. The extent of the etching in the resultant pits was then monitored through AFM to measure the volume of material removed along with other pit dimensions. The method allowed for multiple independent measurements on a single sample, which could be selectively treated to eliminate comparability issues associated with measurements on multiple samples. The system could be modelled via finite element method (FEM) to calculate an intrinsic rate of reaction for the proton induced dissolution of enamel. A proton induced rate constant of dissolution of k_0= 0.099 ±0.008 cm s^{-1} for bare untreated enamel was established, whereas treatment with 1000 ppm sodium fluoride (NaF) and/or zinc chloride ($ZnCl_2$) decreased this rate constant.

The work also characterised the use of calcium silicate as a novel additive in toothpaste and to determine its effect as both a remineralising agent and as a dissolution inhibitor. The release of Ca^{2+} ions into solution was measured which acts to promote the remineralisation of tooth enamel. The addition of phosphate buffer into this solution combined with micro-Raman spectroscopy was then used to confirm the formation of hydroxyapatite (HAP ($Ca_{10}(PO_4)_6(OH)_2$)) material.

The extent of adhesion of calcium silicate onto rough and polished samples was also observed, showing the preference of particles to adhere to rough surfaces, and was quantified by investigating the effect of infilling of etch pits formed via the SECCM method above, which showed an average pit volume reduction of 77±12%.

The second element of the thesis involved investigation into the initial phase of nucleation, nanoprecipitation and growth of calcium carbonate crystals using voltage driven ion migration within a nanopipette (~50 nm opening) geometry to control the mixing of constituent ions to selectively control and induce the nucleation and dissolution of crystals and monitor their growth. This was achieved using oppositely charged CO_3^{2-} and Ca^{2+} ions, inside and outside the pipette respectively, which could be either driven together or apart depending on the applied polarity.

This process was modelled using FEM to give quantitative information about the growth rate and nanocrystal size during growth as well as analysis of the saturation levels within the probe geometry. The nanocrystals formed were studied in situ using micro-Raman spectroscopy

to give information about the polymorph of calcite produced. The effect of the driving bias was demonstrated and rationalised through simulation along with the effect of constituent ion concentration.

This method was used to assess the effect of maleic acid as an inhibitor to the formation of calcium carbonate. Its potent effect was shown by the significantly larger time taken to block the pipette by crystal growth. This also provided evidence for the mechanism of crystal growth inhibition by comparison with ion concentrations expected as a result of a pure chelation effect.

1 Introduction

This thesis is presented in the form of published work, so much of the introduction and methods used are introduced in each chapter. The aim of this chapter is to give a deeper introduction to the subjects of dental remineralisation, crystallisation, and experimental techniques which are investigated within this thesis. The structure of enamel will be discussed, along with the mechanisms by which dissolution and remineralisation occur in the dental cavity. Toothpaste additives designed to remineralise the enamel surface will also be considered. In addition a background to crystal growth and dissolution will be given, with a focus on nucleation and initial growth. The industrial application of both these subjects will also be outlined. The various microscopic methods utilised will be discussed to provide detail of both the strengths and weaknesses of the different techniques. Calcium carbonate crystallization within the defined geometry of a nanopipette will be investigated using an electrochemical driving force and Raman spectroscopy to probe the growth kinetics.

This chapter will also cover the theoretical background of the experimental techniques utilised throughout this thesis.

1.1 Surface Science

Surface science or interfacial science is a broad term that encompasses any phenomenon occurring at an interface. This thesis deals with solid/liquid interfaces although other combinations are possible within the discipline. The interfacial processes investigated are the dissolution and nucleation of crystals and crystalline materials.

The origins of modern surface science can be considered to have begun with Benjamin Franklin in the 17th century with his seminal studies on the spread of oil on water. However since ancient times, beginning with the industrial production of salt (1), the study of crystals has remained of interest consistently. This even leads to the word crystal having an ancient Greek linguistic origin. Since Franklin's work many other areas have been introduced to the sphere of surface science in the intervening time. This means that interfacial science has hugely impacted on the field of crystal science areas of pre-nucleation, nucleation and crystal growth. An early practitioner was Ostwald who contributed to the theory of preferential growth of large crystals over smaller ones.(2) The developments in the field of surface science have gone hand in hand with the development of instrumentation that has allowed visualisation of surface structure.

Control of crystals either growth or dissolution from an electrolyte solution is one of the fundamental natural processes (3) but also benefits industries such as building materials (4), pharmaceuticals and household

products. In nature, crystals are moulded into service for a variety of differing functions and shapes such as teeth (5), bones and shells (6, 7) using a variety of molecules to influence their growth.(8, 9) Understanding the processes would allow us to subjugate crystals towards our needs by creating new materials with new properties. However, studying these systems is intrinsically difficult due to the array of chemical species used in nature to influence the processes involved.

1.2 Enamel

1.2.1 Structure of the Tooth

Human teeth consist of two major sections; the crown, which is the part projecting visibly from the gum, and the root, which attaches the tooth within the gum. The structure is shown in Figure 1.

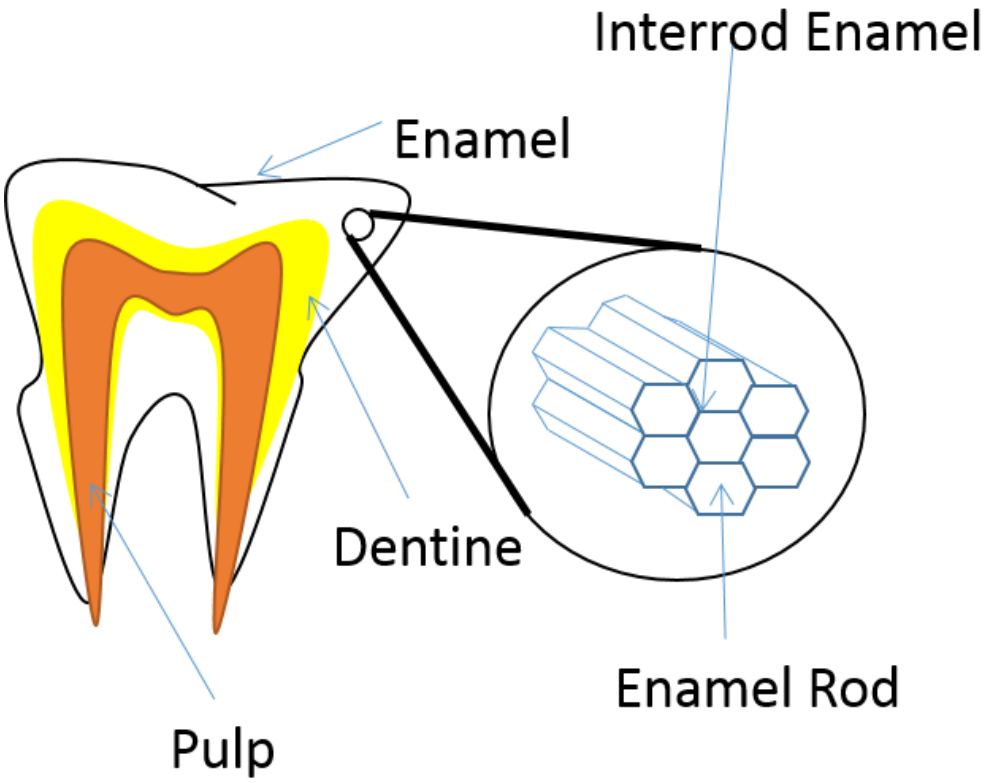

Figure 1 Showing model structure of tooth and rod structure. White shows enamel, yellow shows dentine and red shows pulp and nerve tissue

The crown is covered with enamel, the hardest naturally occurring mineral in the human body, forming the outer protective layer of teeth.(10) It consists of calcium hydroxyapatite (HAP, $Ca_{10}(PO_4)_6(OH)_2$) which makes up more than 95% by weight (5), with the rest composed of a matrix of organic molecules, macromolecules and water. Dental enamel is constructed as a series of units known as enamel rods or prisms, each comprising a tightly packed mass of hydroxyapatite nanocrystallites in a highly orientated and organised structure shown in the inset of Figure 1. Once formed, enamel has no vascular or nerve system, and can only regenerate through

remineralisation processes in the oral cavity.(11) Conversely, the enamel layer can be affected adversely through dissolution processes associated with dental caries or erosion from the modern diet.(12)

The percentage weight amount of HAP varies both between individuals and even from tooth to tooth from an individual.(13) This is because teeth develop during the early stages of life and can be affected by both nature and variations in the local environment.

The enamel covers the dentine to a thickness of ~2.5 mm. This layer is formed from an array of closely packed enamel rods shaped like a keyhole which tessellate together.(14) Each rod is 6-8 µm across and joining each rod is a region called the inter rod enamel ~100 nm across. In this region there are a higher proportion of organic molecules such as proteins. This microstructure is shown in Figure 2 through 2 atomic force microscope (AFM) images. The first is of acid eroded enamel to reveal the microstructure and the second is highly polished to reveal the microstructure.

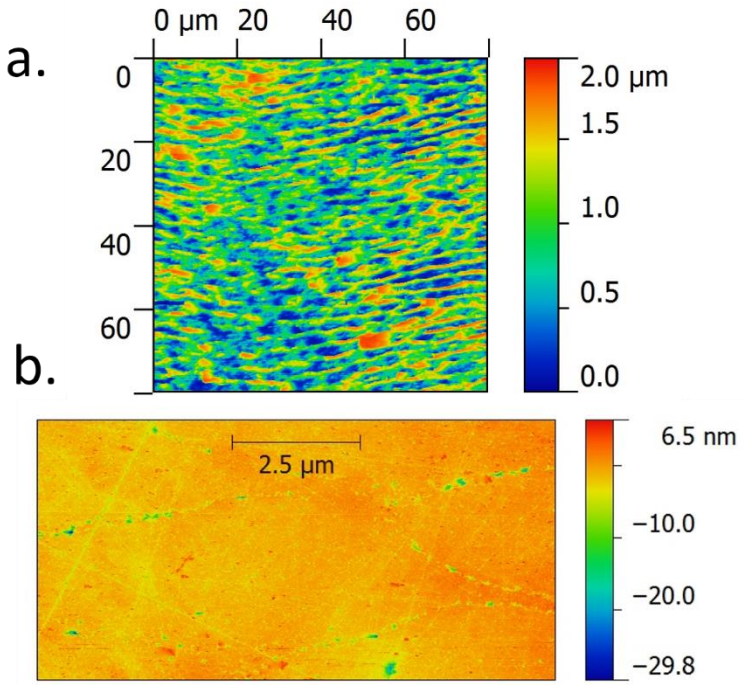

Figure 2 showing AFM image of a. acid eroded and b. highly polished enamel surface which reveals the interlocking rod structure. Data collected by the author

Even though enamel is the most resistant mineral in the body, environmental conditions can cause demineralisation. This principally falls into 2 categories acid induced categories; (i) erosion, which happens in pH below 3 and (ii) caries, which occurs in pH 4-6.5.(15) In this thesis we only deal with the acid erosion of enamel. However, with the aid of saliva, it can be remineralised when conditions permit. This is because saliva contains both calcium and phosphate which are critical in rebuilding the surface of a tooth. Whilst being very hard, enamel is brittle so is supported by the underlying dentine which, whilst still containing ~70% HAP, has a larger proportion of organics, including collagen, which aids in this supporting role.

1.2.2 Prevalence of acid dissolution in the oral cavity

Dental caries(10) is one of the most widely spread diseases in the western world. As a problem disease it is relatively modern. Although there is evidence of caries for thousands of years, the prevalence has risen dramatically in the modern era. Studies of skulls from the ancient world show that caries affected ~10% of the population whilst in modern times this has risen close to 100% in westernised cultures.(16) Occurrences remain lower in poorer developing nations where a less “advanced” diet helps to prevent exposure to an environment that encourages caries formation.

Dental caries is defined as a disease of the mineralised tissues of teeth.(17, 18) In this thesis we are only concerned with the enamel layer. The principal cause of this demineralisation effect occurs due to the action of bacteria which ferment carbohydrates and produce the demineralising acid.(19) Eventually if the demineralisation process is left to continue and no counter remineralisation process takes place, the tissues and inner layers of the teeth can become infected causing pain, aggravation and eventually tooth loss.

One role of saliva is to repair this damage cause by acid because it contains the constituents of calcium and phosphate needed to promote enamel remineralisation.

1.2.3 Introduction to Acid Erosion and Remineralisation

The dissolution of HAP is a principal source of tooth decay via acid attack (20) Figure 3 shows the effect acid erosion can have on enamel with a macro scale treatment: the rough area has been treated with 5 mM citric acid. Figure 3 shows the transition from polished to eroded enamel imaged via interferometry with insets produced via AFM. There are 2 principal methods used to prevent acid attack. First is the use of a protective layer to prevent dissolution. The second is to encourage remineralisation.(21) There is significant commercial interest in remineralisation enhancements. The global market size for toothpaste exceeded US$ 12.6 billion in 2015.(22) Therefore it is commercially important to develop methods of further encouraging this remineralisation effectively.

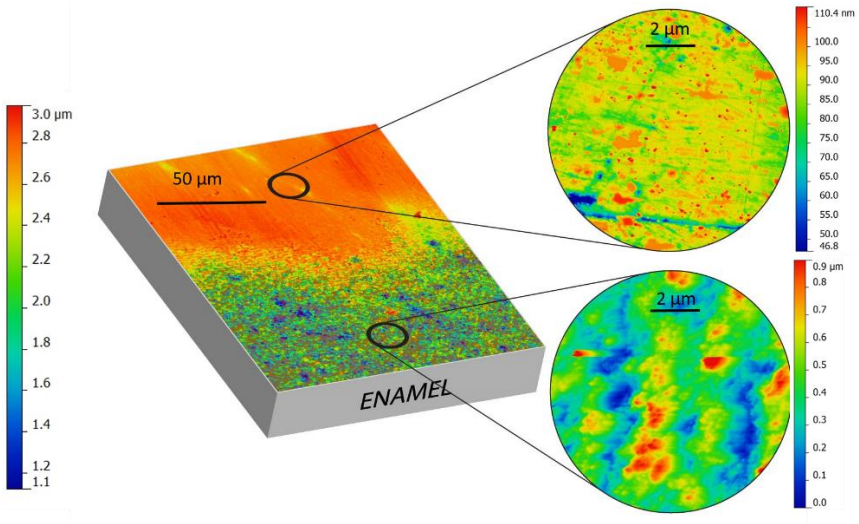

Figure 3 showing effect of acid on polished enamel using interferometry to show the boundary between acid etched part of an

enamel sample and untreated enamel. Close up imaged produced from AFM

Enamel dissolution occurs for a variety of reasons, but most importantly because of acid induced dissolution where HAP is dissolved into the saliva via Equation 1.

$$Ca_{10}(PO_4)_6(OH)_2 + 8H^+ \rightleftarrows 10Ca^{2+} + 6HPO_4^{2-} + 2H_2O \quad 1)$$

This process is the primary mechanism of tooth demineralisation so it is important to minimise its impact by reducing its rate and increasing the opposite reaction known as remineralisation. It's worth noting that remineralisation is the direct reverse reaction not including the inclusion of any extra ions and is grown as a template on the existing enamel although it can also form in the saliva however this is then not retained on the tooth. It has been well documented that the use of fluoride can increase this remineralisation by catalysing the diffusion of calcium and phosphate into the tooth surface thus remineralising the crystalline structure in a dental cavity.(23) This is because the fluoride ion can be included in the crystal lattice displacing the OH^-. The resulting crystal is fluoridated hydroxyapatite and fluorapatite (23, 24), with the added benefit that the new crystal resists acid attack better than natural enamel.

It is also known that different solution pH values affect the way acid attack occurs.(25) At pH 2-4 over short periods of time (hours), significant acid attack is observed resulting in rapid dissolution this is called erosion.

Under pH 4.5-6.5, subsurface demineralisation called caries is observed over considerable periods of time (years) and finally in the presence of strong acid (< pH 2) at time periods less than 2 minutes surface etching is observable.

1.2.3.1 Remineralisation

Remineralisation is a process that occurs naturally in saliva, which contains the substituent ions needed for the formation of enamel i.e Ca^{2+} and PO_4^{2-} .(26, 27) Remineralization occurs at all times when the salivary conditions permit i.e. sufficient super saturation of ions and neutral pH. However as most human saliva is deficient in calcium ions increasing this concentration is a primary method of enhancing remineralisation.(15, 28)

The calcium and phosphate salts present in the saliva are thought to be particularly important to prevent dissolution of the HAP crystals. This ionic presence in the saliva helps to stabilise enamel as their presence in the oral cavity drives against the dissolution process, by driving the reaction towards a remineralisation process. Dicalcium phosphate (DCP), tricalcium phosphate (TCP), octacalcium phosphate (OPC), decacalcium phosphate and HAP have all been shown to be present in saliva with HAP dominating. It is believed that these act as intermediary forms within the remineralisation process. At a neutral pH the equilibrium constants dictate that DCP reforms into TCP, then onto OCP before ultimately forming HAP.

1.2.4 Enamel Dissolution

The majority of research has focused on enamel dissolution through acid challenge or the effect of varying compositions of bathing solution to vary the saturation.(29, 30) Very early quantitative studies of enamel dissolution using undersaturation began to show the importance of diffusion of species from the surface to the bulk solution. However the importance of surface kinetics was largely ignored.(20, 31-36)

These early studies showed that the dissolution rate for powdered enamel was dependant on the rate of stirring which led to the conclusion that a mechanism of dissolution was limited to the rate of diffusion of ionic species to the enamel surface.

To understand the kinetics of the surface reactions, studies of dissolution under highly controlled hydrodynamics were undertaken.(32, 37-39) Nancollas principally carried out research using the rotating disc method so that the controlled hydrodynamic flow over the enamel surface was established.(39) This allowed the dissolution rate to be monitored through observation of the solution pH and thus calculating the uptake of protons by the enamel surface. This found that varying the undersaturation of the solution by varying the calcium and phosphate concentration changed the rate of dissolution, whilst varying the spin speed (and thus the rate of mass transport) also had an effect on the rate.

Several mechanisms have been proposed to quantitatively explain HAP dissolution. However, the model that dominates is the “diffusion” or “kinetically limited” model.(29, 39) The diffusion model suggests that dissolution of HAP is due either to the transport rate of the protons from the bulk solution to the surface or the rate the products, Ca^{2+} and phosphate species move away from the surface. This explains that under diffusion-controlled conditions, the dissolution is essentially limited by the transport of species to or from the HAP crystal surface, but the kinetically controlled limit of the dissolution rate is limited by the chemical reactions at the surface of the HAP. This model is shown in Figure 4 which shows the possible rate limiting steps of kinetic or mass transport controlled regimes.

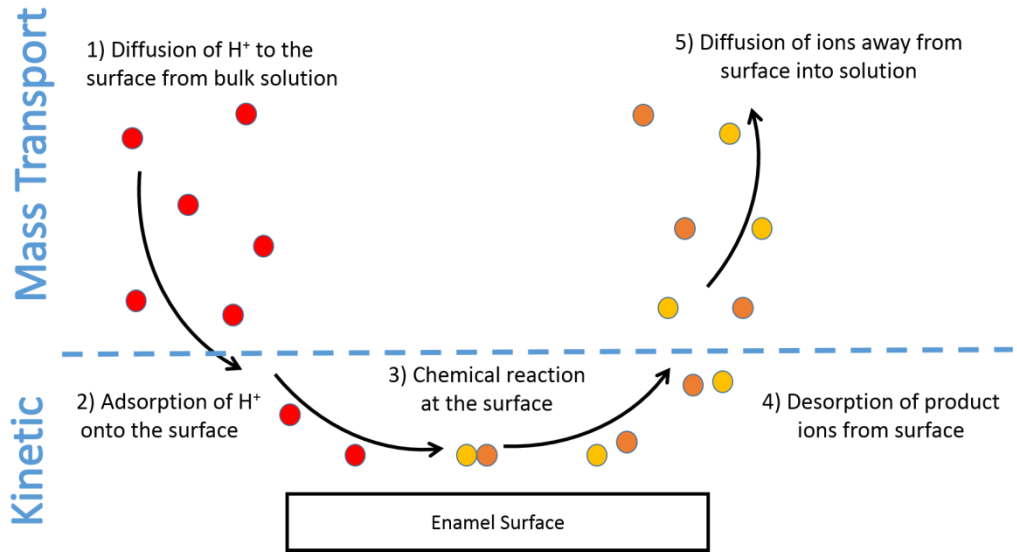

Figure 4 showing the various stages of dissolution and the areas of kinetic and mass transport limits

These two limits can only be defined as a difference in supersaturation immediate to the surface. In a kinetically-controlled regime, the solution is undersaturated with respect to HAP and in a diffusion-controlled regime the solution is saturated. A plethora of techniques have been brought to service to understand both this mechanism and rates of enamel dissolution, because understanding the processes is important to develop preventative and restorative treatments.(20, 23, 40-46) Historically, studies have focused on bulk chemical analysis of solutions during dissolution such as hydrodynamics, concentration of reagents, solution undersaturation, temperature and crystal size using methods such as rotating disk, constant composition and dual constant composition. The bulk of these required the monitoring of either H^+ uptake or Ca^{2+}/phosphate release. These methods were able to determine diffusion layer thickness,

rate constant and rate order, however the experiments largely remained within the diffusion-controlled limit.(44) To try to overcome this techniques including AFM(42), profilometry(12), scanning electron microscopy (SEM) (46) and nanoindentation(40) have all been utilised. These studies have proven that HAP dissolution is directly linked to the solution pH, with low pH inversely proportional to the rate of HAP dissolution. It has also been shown that the presence of calcium and phosphate ions cause slower dissolution as it makes dissolution less favourable because the concentration gradient in the solution is lowered and thus favours remineralisation.(47)

The aim in the first part of this thesis was to investigate the active component of a new toothpaste, Regenerate, in its effectiveness to increase the capacity of saliva to remineralise enamel. Research has been focused on solutions that balance calcium and phosphate to artificially remineralise the teeth; however most of this work has shown to be not commercially viable due to variations between individuals. Work in this thesis has aimed to get round this by boosting the natural ability to remineralise by increasing the quantity of bioavailable Ca^{2+} in saliva which is usually significantly lower in concentration than the phosphate species in saliva.

It should be observed that, whilst the aim was to provide treatments for use in humans, the studies were carried out using bovine enamel. The differences between human and bovine enamel are thought to be small but

there are structural differences which can lead to bovine enamel dissolving up to 3 times faster.(48) This is because of increased porosity, differing rod configuration and a thinner crystalline material at the surface in bovine enamel.(49) Due to differences in water supply there also tends to be a lower natural fluoride concentration in bovine enamel. However, given these differences, the similarities between the two materials makes bovine enamel a widely accepted alternative for use in laboratory studies.

1.2.5 Enamel Dissolution Inhibitors

Inhibitors can drastically affect the dissolution of enamel.(23, 33, 34) This may be because an active site is occupied by additive molecules/ions. Fluoride is the best known inhibitor for enamel dissolution, (24, 28, 31, 33, 34, 50) the ions of which are absorbed onto the HAP surface under neutral pH which prevents dissolution by creating fluorapatite and calcium di-fluoride. However, if over used, particularly in developing children, a condition called fluorosis can develop which discolours the teeth and is therefore seen as a negative drawback particularly in later life.(51)

There has also been research into other possible inhibitors.(19, 28, 32, 33, 52-54) One example is that of strontium ion inclusions which can hinder dissolution by the strontium ion replacing Ca^{2+} within the HAP lattice.(55, 56) Mn^{2+} have also been shown to prevent dissolution and cause variation in etch pit size and morphology when treated enamel is

exposed to acid attack.(57) Another material studied extensively is Zn^{2+} which is a common antibacterial agent and can be absorbed into the HAP lattice.(58) Although Zn^{2+} shows great promise at hindering dissolution, its toxic nature and lesser effectiveness has as yet prevented its use in replacing fluoride widely for human use.

1.2.6 Enamel summary

Acid erosion on enamel is a rapidly expanding field of research due to our modern diets.(12) The studies reported herein examines the susceptibility of treated enamel surfaces to acid attack and draws a comparison to untreated enamel surfaces using scanning electrochemical cell microscopy (SECCM); the aim of which is to understand dissolution rate and the effect of surface treatments on this rate. To carry out this investigation, a range of properties, for example dissolution rate and topography, can be measured to study the crystal.

1.3 Calcium Carbonate Crystals

The second aim of this thesis is to examine the crystallisation of calcium carbonate. Calcium carbonate includes an array of different phases principally that of calcite, vaterite and aragonite.(59-61) The method discussed was briefly trialled using calcium phosphate as the resultant crystal however the trial was not successful and so calcium carbonate was used as a simpler system with fewer possible polymorphs.

Nature uses a combination of soft organic matter and hard crystals in order to produce hybrid materials which perform a variety of roles.(62, 63) These includes biominerals like bones, teeth, and shells and often are formed in highly controlled shapes to facilitate their mechanical (6) and optical (7) properties. Replicating this controlled shape is of high interest to the development of manmade materials. The most common of the biomaterials is calcium carbonate. Within organisms it is most commonly produced in series of layers and macromolecular structures from vesicle deposits and the nucleation is controlled by acidic proteins.(64, 65) There have been many attempts to recreate these structures or at least control the crystallisation using structures at interfaces to circumnavigate the need for protein molecules.(66)

Calcium carbonate forms highly insoluble crystals(67) from almost all natural water sources.(68) This forms a layer known as limescale (69) where layers are formed from calcite and gypsum amongst other insoluble

salts such as calcium sulphate. Historically these deposits have been removed through the use of acidic media, which can equally damage the underlying surface. Therefore the removal of these deposits is of particular interest industrially(70-72), along with the prevention of initial growth.(73, 74) Calcium carbonate has been extensively studied as a model system because it has many natural and practical uses but, due to the need for acid in removal, studies commonly focus on prevention rather than removal. The two main approaches taken to challenge this are the inhibition of growth with additives, which prevent nucleation by retarding growth (75-79) and the prevention(80) or control of nucleation to direct the formation of specific polymorphs(81) to aid in eventual removal. The most common method of preventing growth directly is to add chemicals which prevent growth by binding to calcium ions in solution, often using molecules which chelate such as maleic acid. (76, 79) The molecules selected for this purpose invariably contain functional groups which readily bind to the calcium ions, or attach to sites on the crystals.

The three common polymorphs of calcium carbonate ($CaCO_3$) are calcite, aragonite, and vaterite. In many natural systems they frequently exist alongside each other.(60) Each polymorph possesses a unique crystal structure.(82) Therefore, the polymorphs can be relatively easily distinguished using vibrational spectroscopy, such as Raman spectroscopy. Raman has been extensively used to study calcium carbonate and its polymorphs including complex systems such as the variation of differing

polymorphs within a sea shells(60, 82-85), and is used here as a validation of crystals formed.

Solid structure nanopores have become increasingly used as model channels(86) they have also found uses as: sensors;(87-89) the synthesis of nanoparticles with narrow size selection;(90) and as a molecular sieve.(91) When embedded within a defined conical geometry, the nanopore can be considered distinct and inclusive of a nanochannel. These show behaviour as nanofluidic diodes due to the voltage gated ion current they possess.(92, 93) There are an array of reports from groups detailing the development of electrical sensors which utilize variations in ion current measurements across membranes containing asymmetric nanopores(94-100), often created using the track-etching method.(101) This method however is particularly involved with a low rate of success. The alternative method utilising capillaries pulled with a laser puller to form glass or quartz nanopipettes can produce far more consistent and quick structures.(102) These nanopipettes, shaped with a conical nanopore at the tip, exhibit many of the properties associated with other asymmetric nanochannels. However, in addition, they can be manoeuvred with high spatial resolution. When the capillary is filled with an electrolyte solution it can and is often used to mimic biological systems (93, 103) as they are similar in design to nanopores produced by proteins which behave as ion channels.(104, 105)

There are significant applications where nanopipettes are used as imaging probes for the scanning ion conductance microscope (SICM), a technique that has been used to image cells (106-108), the analysis of surface processes (109), sense surface charge(110) and functionalized for use in sensing applications.(111-115) Here, we are interested in the method where nanopipettes were used to produce strong ion current densities, where mass transport is well defined (102, 116), and therefore create locally artificially highly supersaturated solutions, which induce precipitation. This nanoprecipitation (104, 105, 117) forms a particle at the end of the nanopipette, thus restricting the ability of ions to flow due to the blockage, essentially altering the nanopipette's dimensions. The reverse is also true as the nanopipette can produce low supersaturations where dissolution of nanoparticles dominates. Therefore, this method exhibits a high degree of control over the nucleation, and the very initial stages of crystal growth. This method is made more effective due to recent advances in nanopipette fabrication, allowing for very small pipette dimensions to be achieved.

Conical nanopores have shown new chemical and electrical phenomena; ion current rectification, which is the asymmetric enhancement of ion current due to an applied voltage across the nanopore.(102, 103) This phenomena can be utilised to concentrate weakly soluble salts(104, 105), control the interface of two solvents using organic molecules with differential solubility(118), and as a method to control nucleation of sparingly soluble salts.(117) This leads to a method to both

monitor the precipitation in real time and at the nanoscale and to repeat the measurement in order to generate results with high statistical accuracy.

Here, it is shown that a potential bias through a nanopipette can control ion migration to cause selective precipitation and dissolution of a common industrially problematic insoluble salt. Through a series of varying conditions we present a method for investigating the conditions where nucleation is preferential. We also utilise finite element method (FEM) modelling to provide kinetic information about the driving factors behind the process. Finally we confirm the precipitate and polymorph formed within the nanopipette through the use of micro-Raman spectroscopy.

1.3.1 Applications of Crystal Nucleation, Growth and Dissolution

The formation and dissolution of crystals is a subject that has been of interest for centuries, particularly in respect to industrial applications in order to control the crystallisation process, the size and the polymorph formed.(119) This is because a greater understanding of nucleation, size and morphology are important in controlling other aspects such as solubility.

The formation of crystals can be described in two distinct steps. Firstly nucleation, the formation of a new stable phase within the solution. Secondly growth, the process of addition of ions to the crystal surface from

the solution. This thesis will focus on the first stage, nucleation, which will be explored in later chapters.

Nucleation itself can occur via two differing methods - homogeneous and heterogeneous growth. Homogeneous nucleation is the formation of nuclei within a solution from the aggregation of ions present in the solution. Heterogeneous nucleation occurs on a surface or impurity present in the solution preferentially. After nucleation the growth can occur via a variety of differing mechanisms which are not the subject of this work.

An area of particular interest is the biological formation of solid particles to form biominerals which can exhibit unique and desirable characteristics. Sometimes this may be an amorphous state (9, 120) but, more often, crystallinity is necessary in order for the material to carry out its desired function.(6, 7, 121, 122) One example of this are the shells of marine creatures many of which are made of calcium carbonate in the form of calcite (8, 81, 123, 124) which is the most stable morphology.(59, 125) These shells can produce structures that are highly shaped but relatively little is known about how these are formed. The ability to control the nucleation of these crystals would bring us one step closer to understanding these processes.(126-129)

Alongside HAP (130-132), calcium carbonate is one of the most studied crystal systems due both to its natural abundance in many rock formations but also for its industrial applications as it is the primary constituent of limescale, the removal of which is of huge industrial

significance in applications ranging from household appliance maintenance to toilet cleanliness and the prevention of scale in oil wells. This includes the study of processes that alter surface processes such as additives.

The aim of the crystal growth study in this thesis was to develop a method to control the nucleation and growth of calcium carbonate and the conditions under which this can be managed including a method that controls the diffusion and mass transport of ions in the system, which can be mathematically modelled to understand the kinetics involved.

1.3.2 Crystal Nucleation Theory

Nucleation is the process where there is a distinct change from one phase to another where a small number of ions, atoms or molecules begin to join into a distinct material.(133) In this thesis all crystal nucleation processes involve changing from solution phase to a solid phase.(134) In such situations the process is driven by the concentration supersaturation (135, 136) and temperature.(137) The early nucleation process has a fundamental impact on the resulting crystal formed; therefore understanding of the nucleation fundamentals are of imperative importance. The predominant issue in studying this process is one of size as an initial nucleus is 100-1000 atoms in size (136) making direct observation of this stage impossible.

Two models dominate the theory of crystal nucleation. The first, classical nucleation theory dictates that the rate of nucleation, J follows the

form of Arrhenius equation shown in equation 2.(138, 139) The result of which is shown in Figure 5 where ΔG is the Gibbs free energy for the system, k_b is the Boltzmann constant and T is temperature and r is the radius of the particle. From the Figure 5 it can be seen that free energy change increases until the critical cluster size is reached after which the free energy drops allowing the nucleus to continue to grow.

$$J \propto e^{-\Delta G/KbT} \quad 2)$$

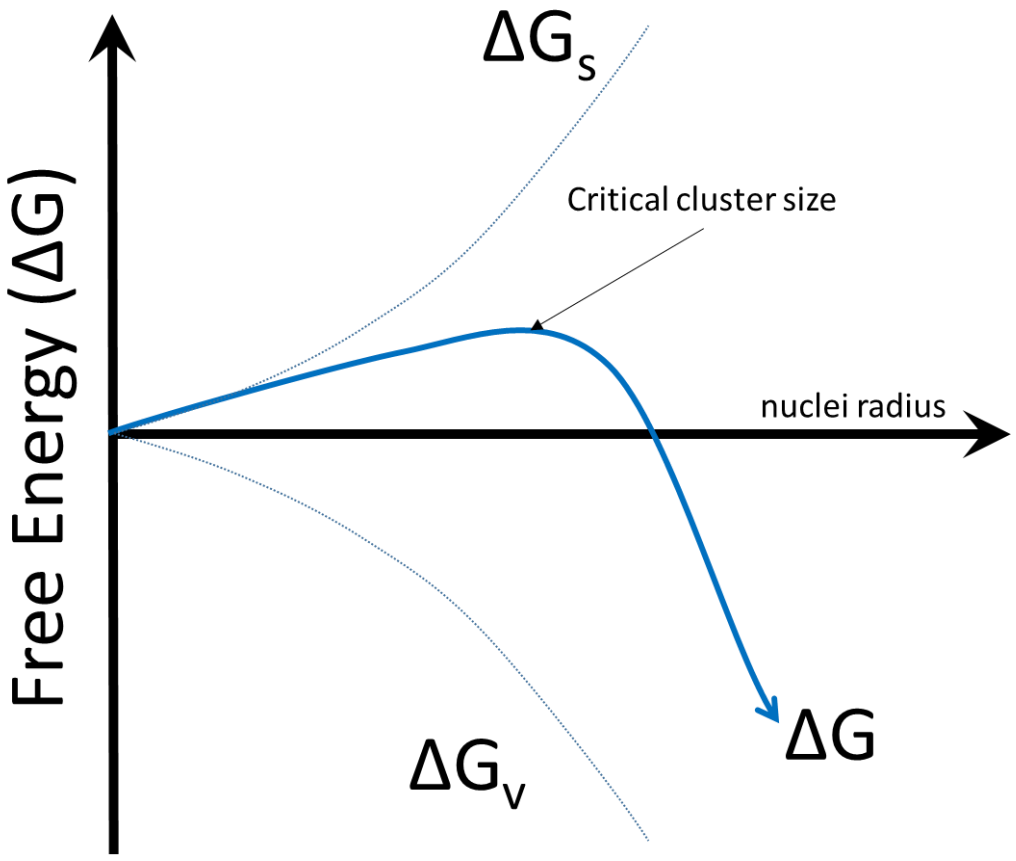

Figure 5 free energy diagram for nucleation

In Figure 5, ΔG is equal to the sum of the surface free energy ΔG_s and the volume free energy ΔG_v the particle is modelled as a sphere, which is the most energetically favourable shape. It can be seen that initially after during nucleation the surface energy term dominates increasing the overall system free energy, after a certain size (the critical cluster size) the volume term begins to dominate and the activation barrier is passed and the particle can continue to grow unhindered as the free energy drops.(133)

The limitations of this classical model mean that it assumes the particles are spherical and free from crystal defects and one monomer is added sequentially. For this reason the two step model was developed to address these issues.(140) It can be seen that the two-step model allows for a small amorphous cluster to form as an intermediary to the final crystal structure.(141) The major difference is that the intermediate does not have the same crystal structure as the final crystal.(136) This model is particularly favoured when describing the existence of different polymorphs. The amorphous clusters (known as metastable form) provide a lower energy barrier of formation, because of the lack of crystal structure, whereby it is possible for differing polymorphs to form from the metastable cluster.(142)

Nucleation can be seen to have two differing modes; homogeneous when nucleation occurs in solution, and heterogeneous when it occurs on a surface.(133) It can usually be assumed that crystal growth on a surface is energetically more favourable making heterogeneous nucleation

preferred.(143) This can be observed, as crystals tend to form, and thus nucleate, on imperfections at much lower supersaturation than via homogeneous nucleation, although some surfaces may lower the barrier to nucleation further through variations in surface charge for example.

1.3.3 Polymorphism

Many crystals show polymorphism where a chemical or compound has more than one possible crystalline structure (124, 144-147), which have different stability, solubility and dissolution rates. The growth or a particular polymorph can be affected using a particular solvent, temperature, supersaturation and use of additive molecules.(148) Industrially, understanding how different structures form is essential so that challenges such as cleaning, i.e. the removal of limescale via enhanced dissolution or preventative measures for adhesion can be addressed. In this thesis we look at the way nucleation can be controlled within a confined geometry, within an electric field and the influence of additives which inhibit nucleation. As described in nucleation theory, metastable clusters can help lead towards different polymorphs. The Ostwald rule shows the series of phases that can form before finding a thermodynamically stable state as shown in Figure 6. This states that in most situations the least stable polymorph will form first before eventually forming the most stable (thermodynamic) polymorph in time.(149)

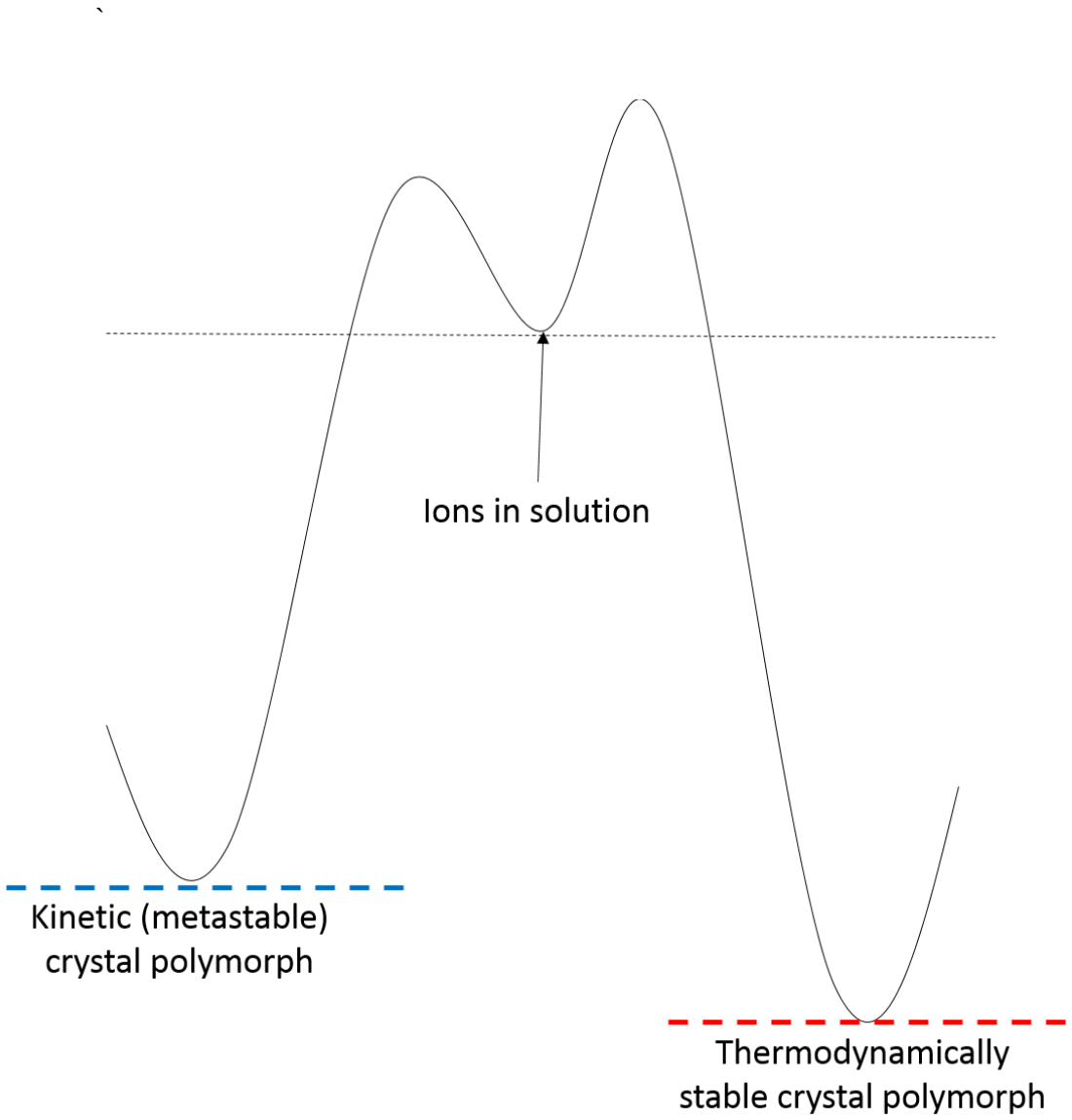

Figure 6 showing energy change diagram of metastable and thermodynamic crystals

One example that is investigated in this thesis is calcium carbonate and its polymorphs.(142) Each polymorph has differing thermodynamic stability and it is the stable polymorph which forms (150), the other states

being metastable.(149) For this reason, in high-supersaturated solutions it is possible to form the more unstable polymorphs (139), as the kinetics dominate, but as the supersaturation drops, a phase change to the most stable polymorph usually occurs as the thermodynamic driver takes over.(144)

1.3.4 Applications to $CaCO_3$

Crystallization research has predominantly focused on a model of classical nucleation theory (151) with subsequent growth via terrace-ledge-kink model growth (152), which relies on the basis of species adding monomer-by-monomer onto step edges and kink sites. Whilst classical nucleation has had a clear success (153, 154), there are circumstances where crystal formation is not able to be explained sufficiently i.e. amorphous phases that nucleate at concentrations far below those allowed by classical models.(155)

These non-classical (156) crystal growth processes have begun to develop into distinct models. One clear example found naturally is the agglomeration of amorphous calcium carbonate (ACC) which eventually form calcite crystals in organisms such as sea urchins (157, 158) for both spines (159) and teeth (160), mammalian tooth enamel (161), vertebrate bones (162), crustacean exoskeletons (163), and mollusc larval shells.(164)

Other non-classical mechanisms suggested include oriented attachment (165), where repeated attachments of crystalline particles occur on lattice matched specific crystal faces (166-168) or, via mesocrystals, which are kinetically stabilized nano-crystals in crystallographic alignment.(169, 170) These mesocrystals are intermediates forms between pre-nucleation clusters and true single crystals which either fuse and transform into single crystals (170) or remain in solution stabilized by other molecules at the particle interfaces.(156, 171-173)

In situ observations of crystal growth in these models are rare, usually limited to liquid-phase scanning probe (174) and transmission electron microscope (TEM) (167, 175, 176) studies. Perhaps more relevantly methods that combine imaging and spectroscopy with data collected at different time points throughout crystallization can detail the kinetics of growth at the early stages of crystallization.(155, 158, 171, 177, 178)

Recently and in opposition to classical nucleation theory, calcium carbonate crystal formation has been found to form as an amorphous cluster phase before forming the more stable polymorph forms both biologically (159, 179) and synthetically.(180, 181) It has also been shown that these mesostable clusters are preceded by the formation of pre-nucleation nano-clusters.(140, 182) The observation of calcium carbonate meso crystals is an area of particular interest as it may have lasting consequences for the crystal that is ultimately formed(183), this has been

shown in several ways such as freeze drying particles(184) and has shown evidence of spherical crystal formation.(61, 75)

The role of the pre-nucleation clusters has been examined using a method of Plunge-freeze vitrification to freeze clusters during a process of nucleation, before being studied via cryo-transmission electron microscopy (cryo-TEM).(180) This allowed sampling at various time points to see the different stages of the mineralization, and showed the formation of pre-nucleation clusters and amorphous phases before transformation into Vaterite and ultimately calcite.(185-187) This work showed that pre-nucleation occurred in solution before ultimately forming crystalline structures on the surfaces studied. It has been speculated (140, 151) that this is because of an entropy gain from the release of water from the ion's hydration shell, which provides the driving force towards pre-nucleation cluster formation, although it has also been suggested (187) this may occur simply due Brownian motion of the pre-nucleation particles and subsequent gain in surface enthalpy. Finally it has also been suggested (188, 189) that $CaCO_3$ clusters of ≤2 nm may have short range order thus making formation more closely linked to classical nucleation theory.

1.3.5 Confinement of crystal growth

Recently there has been significant research and interest in the growth of a variety of crystals within a confined geometry(81, 190-194) which has uniformly lead to the conclusion that a confined geometry, such

as a flow cell(195), has the tendency to stabilise conventionally less stable polymorphs and mesostable phases without the use of additive molecules.

This ultimately leads to the conclusion that crystal growth can be controlled using both additive molecules and modification of the growth geometry therefore the ability to study these in isolation, as presented here, is of particular importance.

1.3.6 Calcium Carbonate growth inhibition

Inhibitors can drastically affect the formation of calcium carbonate. An inhibitor is a chemical that reduces the formation of calcium carbonate crystals and are widely used as a control method in many fields. This may be because an active site is occupied by additive molecules/ions. This use of chemical inhibitors has been used in boilers since 1821 when it was found that potato starch reduces the rate of scale accumulation.(196) Chemical inhibitors may function via several mechanisms chelation, dispersion and inhibition.(197) One mechanism of inhibition occurs as ions in solution, at very low concentrations, adsorb onto the crystal surface, blocking growth positions on the surface inhibiting further precipitation.(198, 199) Other methods like carboxylic acids weaken the crystal structure(200) and chelates such as maleic acid bind around calcium in solution preventing it from joining a crystal.(79)

Whilst the inhibition of bulk growth crystals has been studied widely there are relatively few examples of experiments which exclusively observe the initial stages of nucleation and the effect of inhibitors on ACC. The work that has been done has shown the “Janus” like behaviour of larger molecules such as poly(aspartic acid) which present inhibiting behaviour at the ACC phase but promotes growth later in the solid phase of growth.(201) In contrast, this work by Meldrum *et al.* show the small molecules (magnesium and sulphate ions) investigated inhibited crystallisation in all phases. This has particular relevance for applications in calcium carbonate systems as the control of the early stages of nucleation leads directly to the eventual polymorph and crystal size eventually formed. These 2 parameters directly relate to the ease with which deposits are eventually removed.

The work presented in this thesis seeks to bring together the two strands of research into the early stage nucleation and then growth of calcium carbonate. The aim is to begin to understand how the early stages of nucleation, which have been observed in isolation via the methods outlined above, continue to their eventual polymorph. This thesis does this by using Raman spectroscopy to track the growth in real time from early nucleation through to the establishment of a specific polymorph.

This interesting problem could be addressed further in future work using the pipette method presented here as the method exclusively deals with monitoring differences at the early stages of nucleation and growth.

1.4 Mass Transport and Surface Reaction Kinetics

Any surface process such as crystal growth and dissolution is mainly dependent on two processes. Mass transport which describes the transport of species to and from the surface, and surface reaction kinetics which dictate the speed at which reactions on the surface occur.(202)

Mass transport is described by the Nernst-Planck equation (203), equation 3, which accounts for the diffusion, convection and migration of species in the system by calculating the flux, *J* of species of concentration, *c*:

$$J = -D\nabla c + \mathcal{u}c - \frac{zF}{RT}Dc\nabla \cdot \qquad 3)$$

Where *D* is the diffusion coefficient of the species, $\mathcal{u}$ is the fluid velocity, *z* is species charge, *F* is Faraday constant, *R* is the ideal gas constant, *T* is temperature and · is the electric field strength. The diffusion is the movement of the species due to differences in species concentration. Species will generally move from areas of high concentration to areas of low concentration. Convection describes fluid flow as a result of external factors such as vibrations, thermal or density gradients. Migration occurs due to charged species moving within an electric field.

1.5 Techniques for surface analysis

1.5.1 Optical Microscopy

Optical microscopes allow the visualisation of a sample at high magnification, much greater than is possible by eye.(204) This is achieved through use of visible light and its ability to be diffracted and refracted when passed through a lens. For this reason optical microscopy is commonly referred to as light microscopy. Optical microscopes are the oldest form of microscopy, developed in the 17th century. The limitation of optical microscopy is the wavelength of light itself.

At high magnifications, individual points are seen as diffuse discs surrounded by diffraction rings, called Airy disks.(205) It is these diffraction rings that impact the microscopes limit, the ability to resolve these details. The effect of the diffraction patterns are changed by the wavelength of light (λ), the materials used to make the lenses and the numerical aperture (NA) of the objective lens. This leads to a distance limit (*d*) beyond which it is not possible to resolve separate points called the diffraction limit shown in equation 4

$$d = \frac{\lambda}{2NA} \qquad 4)$$

This shows that resolution can be improved by increasing the NA or lowering λ both of which are physically limited to λ of light or the materials

used. Only by moving to use the much smaller λ of electrons can resolution be significantly improved. There are methods used to surpass the limit but these are usually limited to certain samples, such as requiring fluorescing samples and as such are limited in their use. For this reason scanning probe microscopy (SPM) was developed to advance the visualisation of nano scale features and provide 3D information which is also not usually possible from optical microscopy as it does not require the use of light.

1.5.2 SPM Methods

Scanning probe microscopy (SPM) techniques, typified by the scanning tunnelling microscope (STM) (206), are used to analyse surfaces. This thesis uses several scanned probe methods to look at enamel surfaces. As the name suggests, SPMs use a probe that scans a sample using precise positioning to give accurate topographical and surface property maps, for example conductivity or activity, to a specific reaction. The probe is usually controlled via piezoelectric positioners which can move a probe with atomic precision.

To study the surface properties of materials, several scanning probe techniques have been developed within the field including AFM (207), scanning electrochemical microscopy (SECM) (208), SICM (209) and scanning electrochemical cell microscopy (SECCM).(210) All these techniques have been used to study crystal dissolution.(41, 44, 211, 212)

This investigation will use a combined method of SECCM and AFM to study the dissolution kinetics of tooth enamel.

1.5.2.1 Atomic force microscopy (AFM)

Developed from the scanning tunnelling microscope (STM) (213), AFM is a variant of SPM with high resolution topographical imaging.(207) STM relies on quantum mechanical tunnelling of electrons and thus, for the surface to be conducting. AFM bypasses this need as the probe makes a physical contact to the surface and is easily used to investigate insulating surfaces.(214, 215) AFM is the most common method used for imaging nanoscale materials and the equipment is commercially available from many companies. The topography of the surface being investigated is directly observed by a mechanical probe that is scanned across the surface.

A generalized experimental AFM setup is shown in Figure 7.(213, 216-218) AFM measurements are made via a cantilever with a sharp tip (usually made of silicon), of the order of a few nanometres in diameter, used to scan the material surface. Each cantilever has a spring constant given by the manufacturer. This gives it very high resolution when compared with other techniques which might be in the order of micrometres as the tip size directly relates to the resolution possible. When scanning, the tip is lowered to the surface, the sample is mounted on a piezoelectric scanner which controls the *x, y and z*-directions, which can manoeuvre the sample to perform a raster scan across the surface with the tip rising and

falling with the surface features. The resultant force (F) between the tip and the surface cause the cantilever to deflect. The amount the cantilever is deflected (l) is dependent on the cantilever spring constant (k) and equation 5, determined by Hooke's law. The deflection in the cantilever is measured with a laser beam focused onto the back of the cantilever. This laser spot is reflected off the cantilever into a photodiode sensor which can detect the subtle changes in the tip caused by deflection of the tip from surface features. In the standard contact mode the z position is moved with the piezo to ensure the force between the tip and sample is maintained as constant.

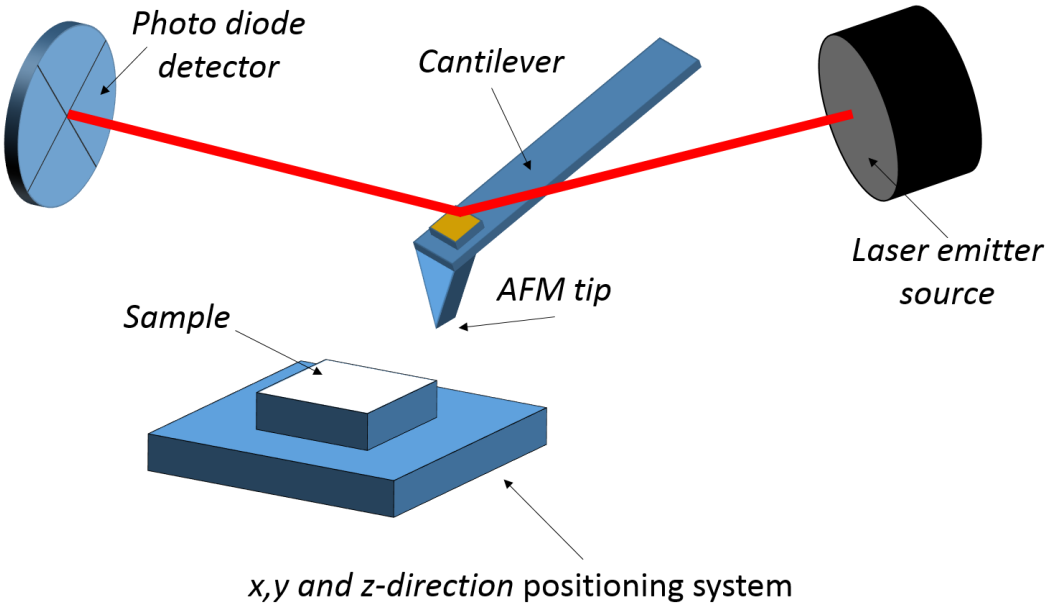

Figure 7 AFM experiment set up

$$F = -kl \quad (5)$$

There are several modes in which AFM can be used depending on the application. These are broadly divided into static (contact) mode and dynamic (tapping) mode. In contact mode, the tip is dragged across the surface of the sample and the contours of the surface are measured directly using the deflection of the cantilever. Originally, the tip was scanned in constant height mode where the tip height remained constant and the changing deflection generated the image. However this risks the tip colliding with the surface and becoming damaged. For this reason, a feedback mechanism is now used to adjust the tip height to maintain a constant force between the tip and the sample. A typical force curve for the tip/sample interaction is shown in Figure 8.

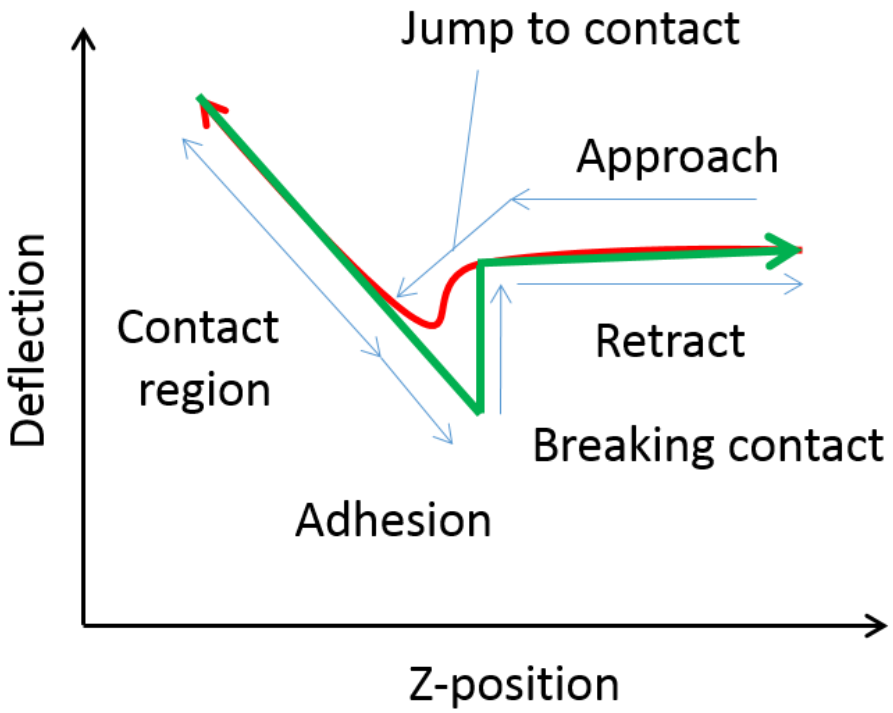

Figure 8 showing a typical force curve measured using AFM

In tapping mode, the tip is vibrated at a specific frequency, as shown in Figure 9. This vibration is dampened by tip-sample interactions which can be detected when compared to the reference vibration and detected to give a representation of the surface topography. Tapping mode reduces the damage done to both the sample and the tip when compared to contact mode as the tip is not dragged over the surface. The feedback used is to maintain the applied amplitude and frequency of the tip to build up the image. The work in this thesis used tapping mode as early testing showed that the hardness of the enamel substrate used caused significantly increased ware rates in the AFM tip reducing the usable life in contact mode.

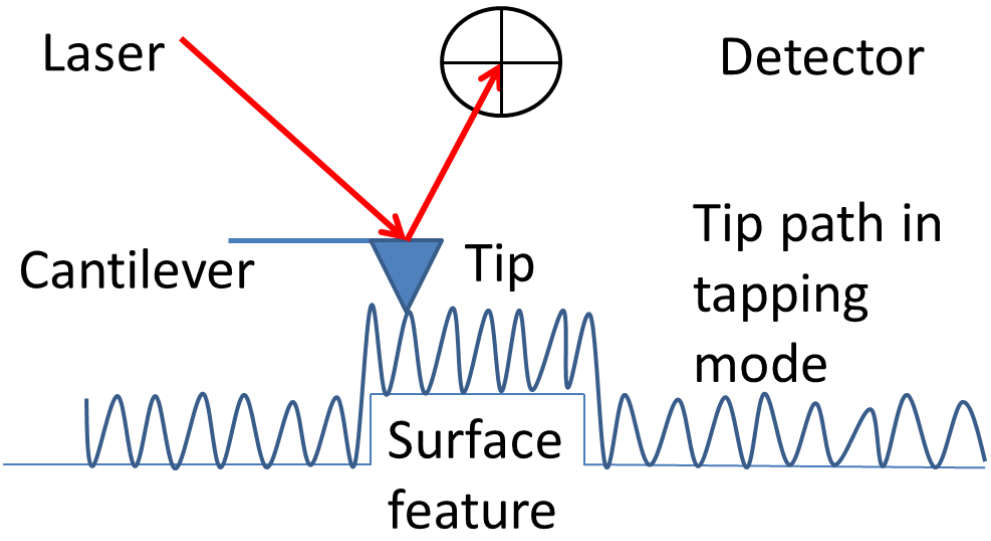

Figure 9 operation of tapping mode AFM

AFM does, however, have both advantages and disadvantages that must be considered. The advantages over other scanning probe techniques such as SEM include that AFM produces a 3-dimensional image and that AFM does not need the use of a vacuum or conducting surface coatings on the sample to produce optimal images. High resolution AFM (219) has produced resolutions similar to that of STM. One disadvantage of AFM is its slower speed when scanning which can cause thermal drift in the sample, meaning that the temperature must be kept constant to produce noise and artefact free images. It is also important to ensure that all images are produced with properly working tips as they can wear away or become damaged thus resulting in poorer images particularly with very hard samples. A significant disadvantage of AFM is its inability to cope with overhanging features or very steep walls as these are prevented from forming tip to surface contact as the tip sides interacts with the feature thus

preventing the tip to reach the surface as shown in Figure 10. This creates false images.

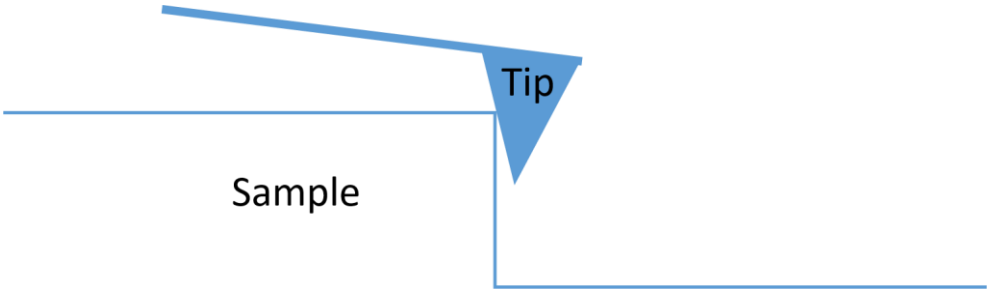

Figure 10 showing an AFM tip interating with a sharp feature which would create a false immage

In this research, AFM is used to visualise the topography of enamel (42) and the pits produced via SECCM. The AFM information was then used to perform pit analysis to calculate average etch pit volumes. Line profiles of the pits formed for experiments in this work are shown in Figure 11 which demonstrates the way a tip tracks surface features.

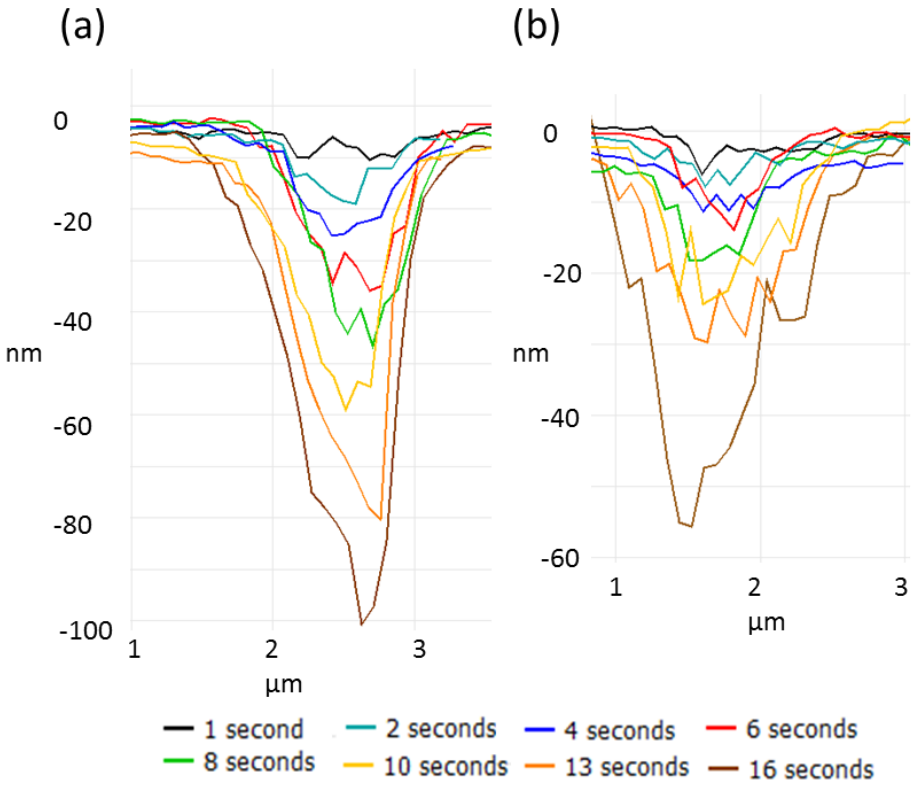

Figure 11 showing series of AFM line profiles at various times of an array of acid etched pits on a) polished enamel b) Fluoride treated polished enamel

To ensure that the AFM data used was accurate a comparison of pits was made using both a standard tip and a high aspect ratio tip as shown in Figure 12 the result of which showed a difference of less than 5% as shown in Table 1.

Table 1 showing difference in measured pit volume using normal tips and high aspect ratio tips

contact time	Normal tip Volume (m^3)	High Aspect Ratio Tip Volume (m^3)
3	2.16E-19	2.22E-19
4	2.50E-19	2.55E-19
5	3.35E-19	3.50E-19
6	3.59E-19	3.70E-19
7	4.24E-19	4.41E-19
8	4.89E-19	4.98E-19
9	6.33E-19	6.60E-19

It is worth highlighting the scale of the pits is less than 1 µm which is much smaller than that of an AFM probe which is on the order of 10 µm

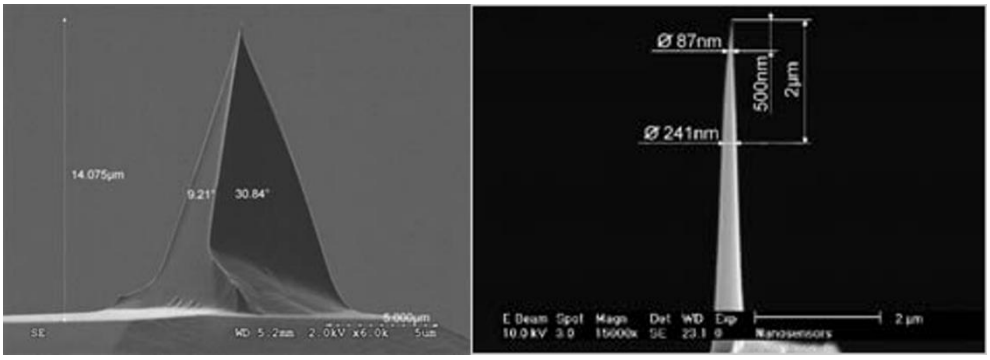

Figure 12 showing a standard AFM tip (Bruker) (left) and a high aspect ratio tip (right) (Nanosensors)

1.5.2.2 Piezoelectric Materials

Piezoelectric materials have the ability turn electrical charge into mechanical movement reversibly.(220, 221) These materials are formed by heating them beyond their Curie temperature, the point they lose their paramagnetic properties.(222) This is because it causes the nuclei to have randomly aligned dipoles and, thus, no overall magnetisation. If a direct

current (DC) field is then applied, the nuclei will align with the induced magnetic field. After removing the DC field the nuclei remain stuck in the aligned position, a process known as poling.(223) By applying a voltage in the same direction as the poling field, polarity causes the material to compress and the reverse causes the material to elongate. The reverse that mechanical compression, will create a voltage, is equally observed. SPMs utilise the highly controllable piezoelectric effect to move probes and samples together in order to carry out the surface analysis with the 3D resolution required to resolve features the size of atoms. The most common arrangement is to have separate *x, y and z* columns in the positioning system in order to prevent false artefacts of the scan forming in the resulting image. However, some systems utilise tube piezo positioners (224) to great effect though often at the lower end of the resolution scale and require the use of software to deconvolute the artefacts produced.

1.5.2.3 Nanopipettes

Nanopipettes are utilised throughout this thesis as a method for containing and defining the mass transport of aqueous ionic salts. These devices are formed from small glass capillaries melted and pulled to a sharp point. These are then filled with the relevant electrolyte solution. The advantage of the solution filled nanopipette over a conventional solid electrode is the ease of fabrication of small radii probes. The idea was first utilised in SICM (209, 225), however SICM is not considered as part of this thesis.

Nanopipettes can be considered a close relative of the nanopore which has been used extensively to study a range of complex systems (226-229) and is again utilised in this thesis to study the crystal nucleation of calcium carbonate.

1.5.2.4 Pipette Fabrication

Quartz glass capillaries were pulled to sharp points using a CO_2 laser puller (P-2000, Sutter). The resulting dimensions were observed using FE-SEM. Figure 13 shows the pulling process used to fabricate pipettes where the centre is held in the laser spot and then pulled apart to form the pipette.

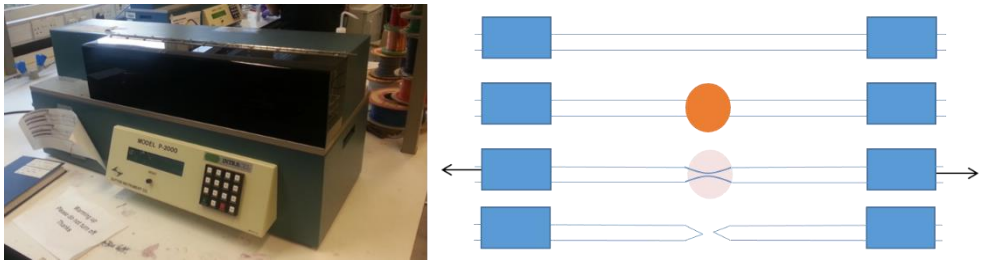

Figure 13 showing p-2000 laser puller and pulling process used

The work contained in this thesis required the use of <1µm probes in order to work, but at these sizes a new variety of dual barrel capillary was needed. It has been known for some time that to use small SICM sizes under 3 µm the starting capillary should have a ~160 µm glass rod that is annealed to the inner edge of the capillary.(230) This rod is called a filament. The presence of this filament acts as a “wick” to create capillary action to allow back filling of the solution being used in the experiment. The

filament can be pulled in a laser puller as usual and the filament reduces in size at the same rate, preserving the capillary effect to the end of the pipette. Due to the small size being used for the investigation in this thesis without a filament, backfilling the dual barrel pipettes are extremely difficult, to fill and leaves air bubbles within the solution of the pipette thus blocking the ion flow. For this reason custom made dual barrel, dual filament capillaries were commissioned and shown in Figure 14. These were shown to be able possible to pull to <50 nm per barrel with the filament intact and could be filled. This thesis is the first example of work to use these new dual barrel, dual filament capillaries.

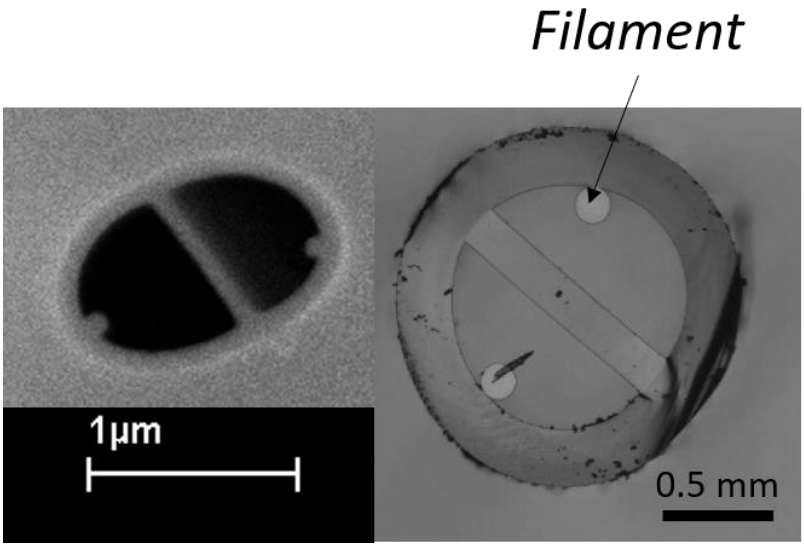

Figure 14 SEM and Optical image of dual filament capillary used

1.5.2.5 Scanning electrochemical microscopy (SECM)

SECM is a common electrochemical scanning probe technique that has previously been used to study enamel crystal dissolution.(44) SECM, though not utilised in this thesis, is a fundamental SPM technique from which several other methods have developed and thus is included here for completeness.(231) SECM uses a solid micro or smaller electrode that is moved close to a surface in solution with either a resulting rise of fall in current depending on the surface in question. The main advantage of SECM is that there is a high mass transport rate for analytes produced at the electrode to the surface. In previous investigations, SECM has been used to promote crystal dissolution by using the probe to generate protons and make a local change in pH at the point directly below the probe.(44) The main disadvantage of SECM is that the whole sample must be immersed in solution. Immersion may affect the surface before the experiment is carried out by causing dissolution to the surface. In addition, the crystal used must be stable in the bulk solution, which therefore limits the samples that can be studied with SECM.

SECM does also have the inherent drawback that the probe has no feedback mechanism. There are, however, some methods to counter this such as intermittent contact SECM (IC-SECM) or atomic force SECM.(232) However these variant techniques are beyond the scope of this investigation.

1.5.2.6 Scanning electrochemical cell microscopy (SECCM)

SECCM (233) takes advantage of a liquid meniscus that forms at the end of a dual-channel pipette which, once in contact with the surface, creates a positionable and mobile nano-electrochemical cell which can be used on both conductive and insulating substrates.(210) The technique is able to deliver high mass transport rates due to the geometry of the probe.(234) When using a conductive substrate it is possible to analyse electron transfer at an electrode surface and also study ion transfer.(235) It also enables the control of mass transport of charged species through control of the potential bias between barrels. The use of this technique has one specific advantage of particular use in this thesis over conventional SPM, such as SECM and SICM (209), due to the use of a mobile liquid meniscus as a probe. This leads to each measurement being collected in a newly exposed sample, rather than the surface having been submerged in electrolyte solution experiencing a bias for a long time, potentially leading to changes in the surface properties. The final disadvantage of SECM is the limited ability to maintain a constant tip-to-substrate distance. In SECCM a feedback loop is used to provide a constant tip-to-substrate separation during scanning by maintaining a component of the ion conductance current.

In an experimental setup for SECCM (210), shown in Figure 15, a glass theta capillary is drawn out to a sharp point of approximately 90 nm – 1µm in diameter. Each side of the barrel is filled with an electrolyte solution

and an Ag/AgCl reference electrode is connected at the open end of the capillary. The solution forms a small droplet at the tip due to the surface tension of the solution which allows electrical contact between the two barrels. When a bias is passed between the two barrels, the resultant currents limiting factor is the size of the droplet at the end of the pipette, thus the current is linked directly to the droplet size.

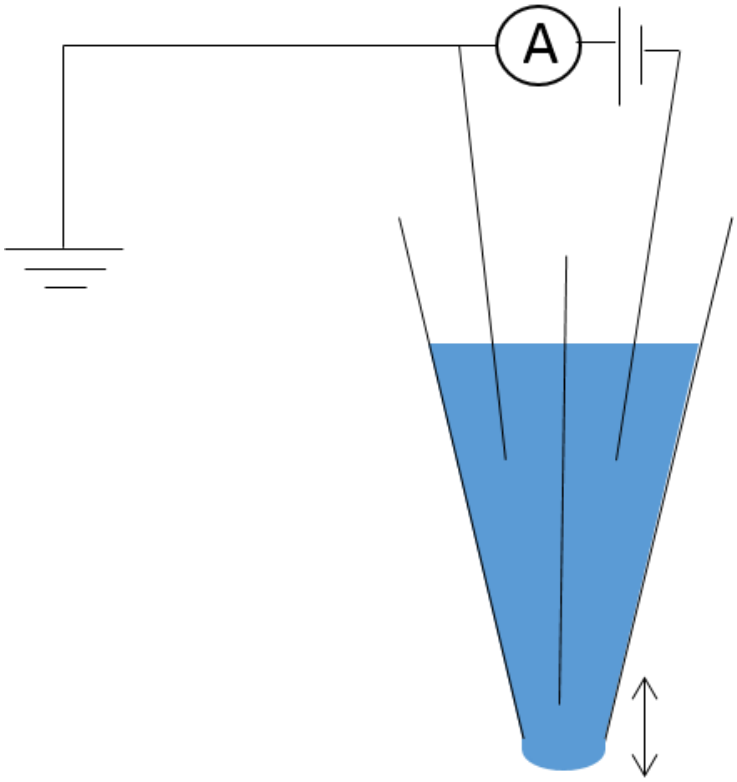

Figure 15 showing generic SECCM set up

This has the major advantage that the probe can now approach the surface of interest in air. To do this, a bias is applied between the two barrels and the tip is oscillated normal to the surface by a set amplitude and frequency. The tip is then lowered towards the surface at a constant, slow

rate using the *z* piezoelectric positioner. When the droplet comes into contact with the surface, a spike in current is observed as the meniscus expands towards the surface. This spike is used as an indicator that the surface has been reached, and so to stop lowering the tip. The increase in the DC occurs as the liquid wets the substrate surface upon contact and draws more liquid into the meniscus. This increases the droplet size and thus lowers the local resistance.

The oscillation of the tip now generates a much larger AC signal as the droplet is squeezed and released against the surface. This is used as a feedback mechanism to maintain a constant tip-substrate separation. At the point of contact there is another possible feedback method with a conducting substrate which is the formation of a surface current as the circuit is completed through the meniscus.

The DC (direct current) has also previously been used for feedback for some specific uses where oscillating the tip is not acceptable: for example, very fast dissolution processes.(109) It is also possible to set up another circuit on conductive surfaces. This can mean that surface activity can be mapped in relation to topography. The tip can then be scanned across the surface and a topographical map produced.

Figure 16 depicts a general SECCM approach curve experiment. It can be seen at the point of contact that there is a large rise in both the AC and DC currents as described above. During the SECCM approach the AC

and DC components, x, y and z position of the pipette are simultaneously recorded using a Field Programmable Gate Array (FPGA) card.

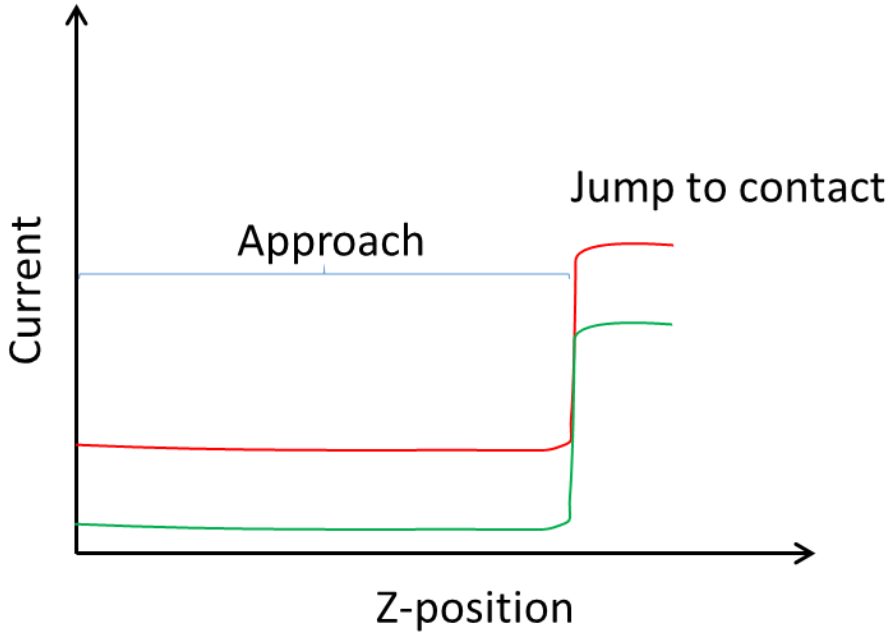

Figure 16 diagrammatic representation of SECCM approach curve. Showing both AC (Red) and DC (Green) outputs

1.5.3 Field Emission Scanning Electron Microscopy (FE-SEM)

A scanning electron microscope replaces light and uses electrons under vacuum in order to create images of a sample by scanning the sample with a focused electron beam which is then detected at a various detectors usually the secondary electrons are detected.(236) This is achieved by scanning the surface with a focused beam of electrons and detecting the returning electrons after they have interacted with the surface.

1.5.4 Micro-Raman Microscopy

Raman spectroscopy is used to provide information about sample identification. It involves exposing the sample to a highly monochrome light source, in this thesis a 514.5 nm laser, and detecting the resulting scattered light. The majority will be elastically scattered, i.e. returned at the same frequency as the incident light, however a small amount will be shifted due to interacting with the vibrational energy levels of the sample molecules.(237) The shifted light frequency can be plotted against the intensity and will give a spectrum of the sample. Raman spectra can be used to distinguish between different polymorph forms of a crystal and is used to this effect throughout this thesis.(60, 61, 82-85, 238-240)

When combined with an optical microscope Raman spectra can be collected from a highly localised area both laterally and in depth ~1 μm in size thanks to a high spatial resolution. The use of a microscope focusing the laser spot has the added benefit of enhancing the photon flux to the surface increasing the received signal. Another benefit utilised in this thesis is the fact Raman is particularly insensitive to water making it particularly suitable for the analysis of crystals.(237)

The resolution of the Raman system is limited by the laser wavelength used and the microscope optics used and defined by;

Spatial resolution = 0.61 λ/NA (237)

Where λ is the wavelength of the laser, and NA is the numerical aperture of the microscope objective being used.

1.6 Finite element method (FEM) modelling

Mathematical modelling is used throughout this thesis in order to quantify the experimental data. This provides information to calculate reaction kinetics that would otherwise remain elusive because the model system allows for a system with a complex geometry i.e. the pipette and allows for simultaneous treatment of multiple physical processes.

Within this thesis two models are used. The first models the acid induced dissolution of enamel. This was based on a model previously produced within the Warwick electrochemistry and interfaces group (WEIG) by Michael Snowdon (241) and modified by the author. The second used to model the blocking of a nanopipette by a growing crystal was created and analysed by David Perry also of WEIG.

The programme used was COMSOL Multiphysics, which utilises the FEM.(242) This method of modelling works on the basis that taking a larger geometry, in this case the tip, and splitting it into a series of small domains can approximate the diffusion, migration and convection effects within the tip. The size of the domains (the mesh) used to calculate these results dictates the accuracy of the simulations. Therefore, in important areas, where physical changes occur rapidly the mesh size is kept small such as at the end of a pipette. Whereas, in less significant areas, the mesh is allowed to grow larger to make the simulation less computationally expensive. The physical processes modelled use partial differential

equations (PDE)s to be solved, for example, transport of diluted ions and molecules, applying an electric field and fluid dynamics. To begin a simulation, an initial value is given by the user before the computer runs a series of iterations where new trial values are used and fitted to the PDE and the error is observed. Through the series of iterations this error is minimised until a threshold is reached. Each PDE is locally approximated using equations for steady state systems and differential equations time dependant models. The work in this thesis deals with steady state systems.

The model is used to calculate the rate of dissolution in conjunction with experimental results in order to calculate intrinsic rate constants. FEM modelling has been used extensively to show many systems with mass transport properties in the literature and has previously been used to quantify SECCM experiments by modelling the scanning probe used in the experiments in order to calculate the migration diffusion and convection involved.(241)

1.7 Chemicals, Instrumentation and Methods

Due to the exclusive inclusion of previously published work please see individual chapters for details of chemicals, instrumentation and methods used within this thesis.

1.8 Thesis Aims

The aim of this thesis is to investigate both the nucleation and dissolution of crystals, crystalline materials and biominerals, using aqueous systems, which have industrial growth uses. The focus will be on two systems: the dissolution and regrowth of enamel surfaces and the nucleation of calcium carbonate within a nanopipette. The aim is to observe these systems using a multi microscopy approach to discern the kinetics involved. To achieve this, the experimental setup is tailored to enhance and control movement of species to the surfaces involved.

The broad spectrum of microscopic techniques used includes optical, electrochemical scanning probe methods, AFM and Raman microscopy. The methods are used in novel combinations to probe the systems of interest. The experimental methods are matched with FEM simulations to gain a greater understanding of the processes studied.

Chapter 2 will explore a new method of investigating the dissolution of enamel using SECCM as a delivery method for defined acid contact, the effect of which is observed and quantified using AFM and ultimately FEM modelling. The effect of surface treatments in preventing dissolution is considered. As detailed herein, understanding the dissolution process has profound effects on basic human health and therefore investigative methodology advances are of paramount importance. Applications that can perform multiple measurements on single samples are particularly relevant.

Herein, just such a method is developed and sample surface treatments with fluoride and zinc ions are investigated.

Chapter 3 utilises the method developed in chapter 2 to investigate commercially relevant new surface treatments. The surface treatment used is calcium silicate which is used in remineralising toothpaste. The effect on dissolution is investigated, whilst the effectiveness as a material for remineralising enamel is studied using SEM to show the particle deposition, ion selective electrodes to measure Ca^{2+} release, Raman spectroscopy to detect the presence of HAP, and AFM to measure the extent to which acid etched enamel pits are in filled by calcium silicate.

Chapter 4 shows a simple new development of a nucleation and growth measurement system which is shown to be particularly effective in probing the nucleation and growth of calcium carbonate. It investigates the selective nucleation of calcium carbonate within a nanopipette using electrochemistry to trigger nucleation. This is industrially important in the development of cleaning products that can both clean surfaces of calcium carbonate, in the form of limescale, and prevent the nucleation of new particles. An ion current is used to control the mixing of calcium and carbonate ions which are driven together to cause crystal nucleation in a nanopipette. The use of inhibitors used to prevent formation are investigated and the crystal formed is confirmed using Raman spectroscopy. The method measures time taken for a tip blocking event to occur by monitoring current transients. Because of the controlled

reversibility of the reaction, many controlled repeats were possible to give highly statistically significant results. The kinetics of the system are validated using a FEM model to account for the migration and diffusion of ions in the system.

Chapter 4 also investigates effect of varying blocking and unblocking biases, electrolyte concentration and the effect of an inhibitor, in the model case maleic acid, which was introduced in trace amounts the effect was to increase substantially the blocking time of the transients.

In the various cases, the microscopic techniques selected are used to their strengths to measure the surface process for which that method is best suited. It is this combination of methods that allows a clear picture of the surface being studied to be formed, and thus, better understood, whether that is for gaining quantitative information or a greater understanding of the polymorphs formed. The valuable contribution of these multi-microscopy methods are combined effectively with FEM models throughout to further extend the understanding of these systems effectively.

2 Combinatorial Localized Dissolution Analysis: Application to Acid-induced Dissolution of Dental Enamel and the Effect of Surface Treatments

2.1 Abstract

A combination of scanning electrochemical cell microscopy (SECCM) and atomic force microscopy (AFM) is used to quantitatively study the acid-induced dissolution of dental enamel. A micron-scale liquid meniscus formed at the end of a dual barrelled pipette, which constitutes the SECCM probe, is brought into contact with the enamel surface for a defined period. Dissolution occurs at the interface of the meniscus and the enamel surface, under conditions of well-defined mass transport, creating etch pits that are then analysed via AFM. This technique is applied to bovine dental enamel, and the effect of various treatments of the enamel surface on acid dissolution (1 mM HNO_3) is studied. The treatments investigated are zinc ions, fluoride ions and the two combined. A finite element method (FEM) simulation of SECCM mass transport and interfacial reactivity, allows the intrinsic rate constant for acid-induced dissolution to be quantitatively determined. The dissolution of enamel, in terms of Ca^{2+}

flux ($j_{Ca^{2+}}$), is first order with respect to the interfacial proton concentration and given by the following rate law: $j_{Ca^{2+}} = k_0 [H^+]$, with k_0= 0.099 ±0.008 cm.s^{-1}**.** Treating the enamel with either fluoride or zinc slows the dissolution rate, although in this model system the partly protective barrier only extends around 10-20 nm into the enamel surface, so that after a period of a few seconds dissolution of modified surfaces tends towards that of native enamel. A combination of both treatments exhibits the greatest protection to the enamel surface, but the effect is again transient.

2.2 Introduction

The dissolution of solid materials is an area of significant interest (243) across many fields, including the earth sciences (244, 245), corrosion science (240), and the life sciences (246), as well as in chemistry.(247-253) Studies of the mechanism and kinetics of dissolution processes are important for both fundamental understanding and for various technical applications. This area requires methodologies that can probe dissolution under conditions of high and well-defined mass transport (254), so that surface kinetics can be extracted free from convolution from mass transport.(254, 255) This means that dissolution experiments must deliver sufficiently high and well-defined mass transport rates that surface kinetics are manifest in the measurement.

This paper describes a powerful combinatorial approach for dissolution studies, in which a large number of micron scale measurements are made rapidly on a small area of a single sample surface, for which different portions have been treated in different ways. The focus is on the acid-induced dissolution of dental enamel as an exemplar system, and one which is also of significant interest. Enamel is the hardest mineral found in the human body (10), forming the outer protective layer of teeth. Its main component is calcium hydroxyapatite (HAP, $Ca_{10}(PO_4)_6(OH)_2$) which makes up more than 95% of enamel by weight,(5) with the remainder comprised of a matrix of organic molecules, macromolecules and water.(13) Dental enamel is constructed from rods or prisms, each containing a tightly packed mass of HAP nanocrystallites in a highly orientated and organised structure.(14) Once formed, enamel has no vascular or nerve system, and can only regenerate minerals through remineralisation processes in the oral cavity.(11) Conversely, the enamel layer can be affected adversely through acid-induced dissolution processes associated with dental caries or erosion from the modern diet.(12, 20, 256)

Acid attack of HAP is reasonably described by the following reaction:(32)

$$Ca_{10}(PO_4)_6(OH)_{2\,(S)} + 8H^+_{(aq)} \rightleftharpoons 10\ Ca^{2+}_{(aq)} + 6HPO_4^{2-}{}_{(aq)} + 2\ H_2O \quad (1)$$

This is the primary process of tooth demineralization: protons react with HAP, which releases Ca^{2+} and HPO_4^{2-} ions into the solution (10, 257, 258), coupled with further solution processes (*vide infra).*

As highlighted above, to understand the relative contribution of surface processes and mass transport to demineralisation rates, experiments need to be carried out under controlled, calculable, and sufficiently high mass transport conditions.(32, 254, 255, 259) The main approach, with well-defined mass transport, used in studies of enamel and HAP dissolution is the rotating disk (RD) method.(29, 37-39, 260-262) However, the RD method is often restricted to bulk solution measurements, which places severe limitations on the time and spatial resolution of the technique.(254) This is particularly detrimental for the investigation of surface treatments that have a transient (temporary) effect, which may be short lived. To elucidate such effects requires methods with high time resolution. In terms of spatial resolution, a number of studies have used high resolution microscopy to study enamel dissolution at the nanoscale.(12, 40, 42, 44-46, 263-265) However, with the exception of SECM (44), the approaches often have rather low mass transport rates and all require the sample to be exposed to solution for long periods, making it difficult to monitor transient effects on dissolution, such as those imparted by surface treatments.

Several treatments have been used to protect enamel from acid dissolution (266, 267), most significantly, the treatment of enamel with fluoride results in a surface layer of fluoridated hydroxyapatite and fluorapatite (23, 24, 54, 268) which resists acid attack better than natural enamel (34, 269), thus inhibiting demineralization.(34, 270) Zn^{2+} treatment of enamel also produces a protective layer. The binding of Zn^{2+} is proposed to lead to the precipitation of an apatite-like phase, and the formation of a zinc complex at the surface of enamel has been suggested.(54, 271-274)

The work presented here employs a new approach for the study of dissolution processes, coupling localized measurements with high and controlled mass transport through the use of SECCM combined with AFM.(210, 234, 275-277) The aim is to demonstrate the methodology and to gain a better understanding of the acid induced dissolution process on enamel surfaces as well as the effect of treating the enamel surface with zinc and fluoride ions. Localized dissolution is achieved by confining the experiment to the meniscus of a pipette with a diameter ca.1 μm, and making a series of such measurements, with different exposure times, across the surface. Migration and diffusion of ions in the probe geometry allows fast surface kinetics can be investigated.(275) In essence SECCM is used as a tool to allow very fine control of the delivery of acid to the enamel surfaces resulting in localized etch pits. Nitric acid was used because it removed complexity in the system as the nitrate counter ion was

consistent with the background electrolyte These dissolution etch pits are then analysed using AFM and, using a finite element method (FEM) simulation, the intrinsic rate for proton induced dissolution (Ca^{2+} release) is extracted. We have presented preliminary data using this method as part of a multi-technique approach to elucidate a new treatment for enamel erosion that was presented in a special issue.(278) Here, we apply the technique in much more detail to common treatments of dental enamel, highlighting the spatial resolution of the approach and developing a full theoretical model to quantitatively analyse data.

2.3 Experimental details

2.3.1 Solutions

All solutions were prepared using resistivity 18.2 MΩ cm (25°C) water (Purite). Etching solutions (50 mM KNO_3 and 1 mM HNO_3 (Sigma-Aldrich)) were prepared daily (pH 3.3, Denver Instruments UB-10 pH meter). Zinc salt solutions used for enamel pretreatment were made using 1000 ppm of Zn^{2+} from $ZnCl_2$ (Sigma-Aldrich). Fluoride solutions for enamel pretreatment were 1000 ppm of F^- using NaF (Sigma-Aldrich). 1000 ppm was used as it is consistent with that of commonly used oral care products in the mouth.

2.3.2 Enamel Sample Preparation

Bovine enamel samples were received from Unilever plc. already saw cut into 6x6x2 mm blocks. These were then polished using a custom made polishing grip shown in Figure 17 before being finished by hand. This was achieved using a silk polishing pad (Buehler) and aqueous diamond suspension starting with particle size 20 µm and working down 10 µm, 8 µm, 5 µm, 2 µm, 1 µm, 0.5 µm and 0.05 µm sequentially until an RMS of <20 nm measured over 20x20 µm by AFM was achieved using a Bruker Nano Enviroscope AFM with a Nanoscope IV controller in tapping mode.

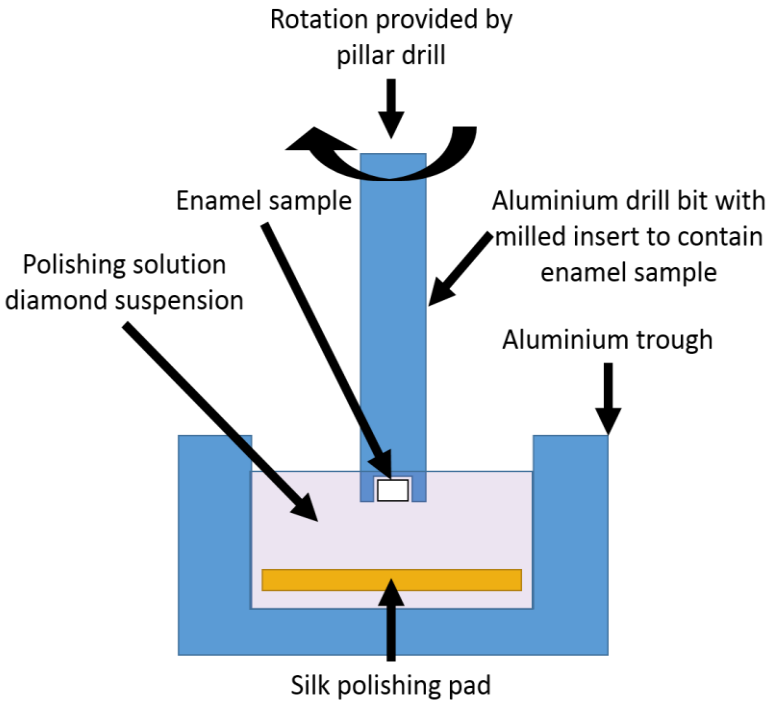

Figure 17 diagram of polishing set up

Three different treatments were applied to each enamel block, one treatment per section, with rinsing of the sample in Purite water between treatments. To selectively treat a particular section, a low tack polyester tape (3M) was used to protect all but the area of interest, before submerging the sample in the treatment solution for 2 minutes (see Figure 18). The treatments used were 1000 ppm F^-, 1000 ppm Zn^{2+}, and a sector of the enamel was also subjected to a combined treatment with F^- and Zn^{2+}, applied sequentially as depicted in Figure 18.

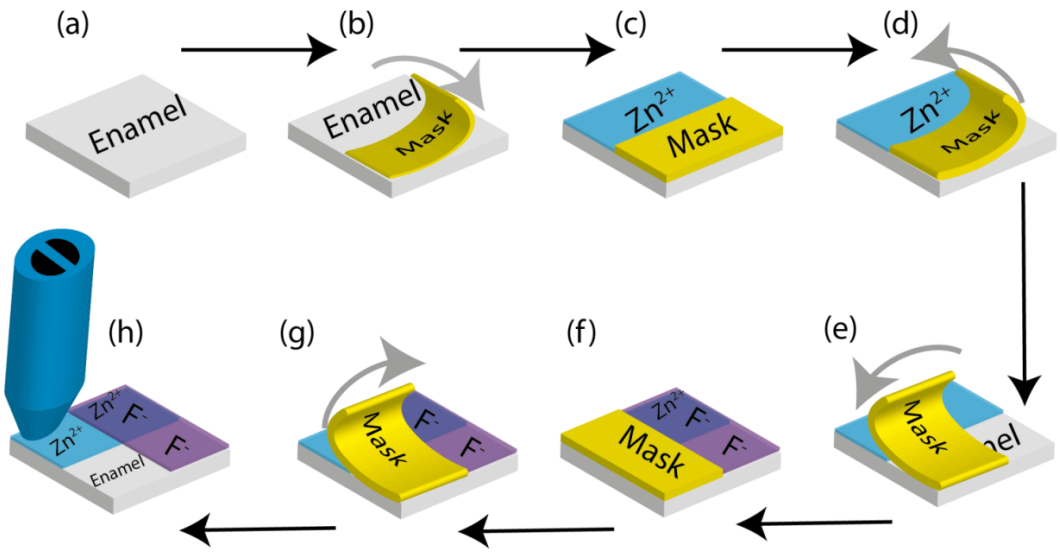

Figure 18 Representation of the localized treatments applied to an enamel block: a) Enamel block polished before any treatment applied; b) Half the sample masked off with polyester tape; c) Zn^{2+} treatment applied to sample; d) Polyester mask removed; e) Mask reapplied at 90° rotation; f) F^- treatment applied to sample; g) Mask removed; h) the final surface studied by SECCM

2.3.3 SECCM method

The SECCM tips used were fabricated from 1.5 mm diameter borosilicate theta capillaries (Harvard Apparatus) that were pulled to a sharp point using a P-2000 laser puller (Sutter Instruments Co.). After pulling, the tip of the resulting pipette was oval and approximately 800 nm across the main axis. A representative tip is pictured in Figure 19(a). Each pipette was filled with the etching solution and a quasi-reference counter electrode (QRCE) comprising an AgCl-coated Ag wire was inserted into each barrel.

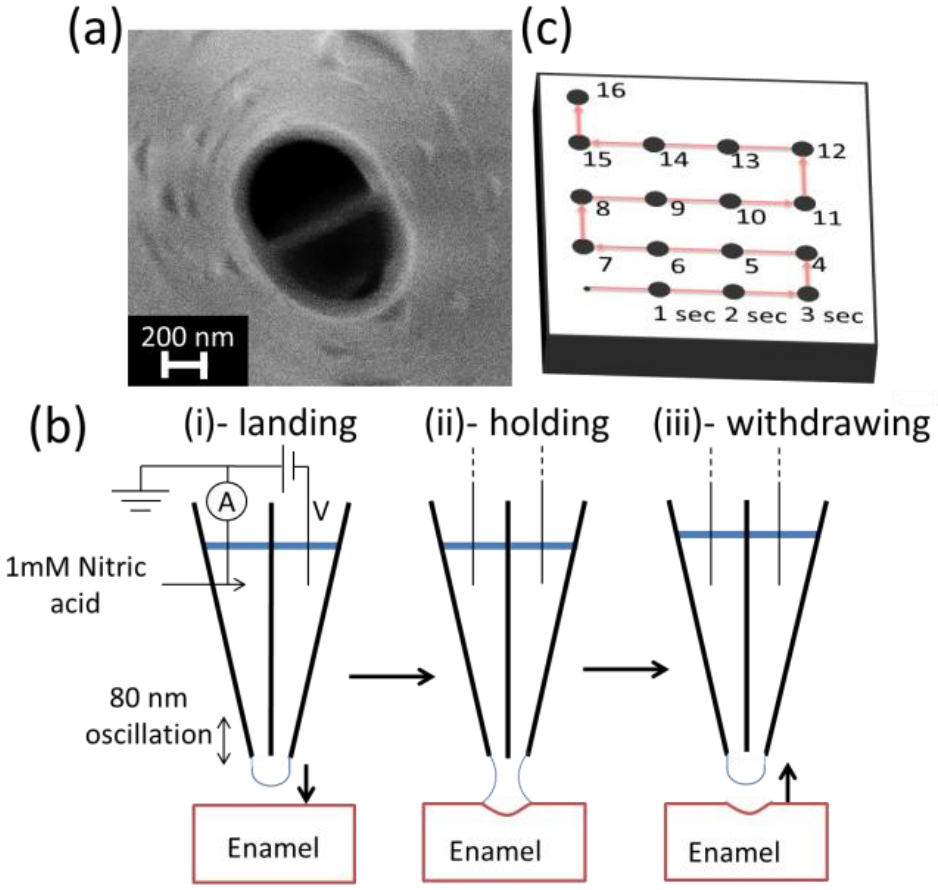

Figure 19 (a) SEM image of a pipette tip. (b) Representation of the experimental setup used. The approach-hold-withdraw cycle and probe path used in SECCM experiments. (i) Probe approaches enamel surface. (ii) Meniscus makes contact with the surface and is held for a set time. (iii) The probe is withdrawn and meniscus removed from the surface. (c) The path the probe takes during the whole array used. Red line represents tip path. Meniscus contact in each spot is 1 second longer than the previous spot

The SECCM technique was set up as recently described.(277) The pipette was positioned close to the enamel surface using a manual micrometer (M-461 series, Newport) aided by a digital camera (Pixelink). Fine positioning of the pipette was achieved using a piezoelectric positioner system with a range of 38 µm normal to the

substrate, in the *z*-axis (P-753.3CD positioner, Physik Instrumente) and 300 µm parallel to the substrate in the *x*- and *y*-axes (Nano-Bio300, Mad City Labs). A potential of 0.25 V was applied between the QRCEs in the barrels of the theta pipette using a home-built instrument controlled via LabVIEW 2011 and a field programmable gate array card (PCI-783R, National Instruments). An oscillation of 80 nm amplitude was applied to the *z*-position of the tip, with a frequency of 233.5 Hz, using an external lock-in amplifier (SR830DSP, Stanford Research Systems), and the resulting alternating current (AC) magnitude at the driving frequency was measured and used to inform on the meniscus condition. An approach-hold-withdraw method, as illustrated in Figure 19(b), was used to carry out local dissolution at the enamel surface with different solution contact times. First, as shown in Figure 19(b)(i), the *z*-piezo was used to move the pipette towards the surface and the approach was stopped when the meniscus made contact with the surface (without the pipette itself making contact) as evidenced by a sudden change in the AC value. Typically, a threshold value was used that was one order of magnitude higher than the background AC measured when the tip was in air.(279) The meniscus was held in contact with the surface for a precise period of time (Figure 19 (b)(ii)), after which the pipette was rapidly withdrawn from the surface (20 µm s^{-1}), breaking meniscus contact (Figure 19(b)(iii)). The pipette was then moved laterally to the next approach location at a velocity of 1 µm s^{-1} (taking 5 seconds). In

this time, the solution in the meniscus retuned to its initial conditions (equilibrium reached in << 1 sec).(277) This procedure was used to prepare an array of local etch features, following the pattern described in Figure 19(c), which also shows the path of the pipette. The array created in this experiment started with a 1 s meniscus hold time on the surface, and this was increased by 1 s for each subsequent position, up to a total of 16 s. Six arrays were created in each treatment section of an enamel surface and a total of four bovine enamel samples were studied, meaning that 24 separate arrays were created for the four different surfaces. Optical images showing an experiment in progress and an example of the resultant pit arrays are provided in Figure 20.

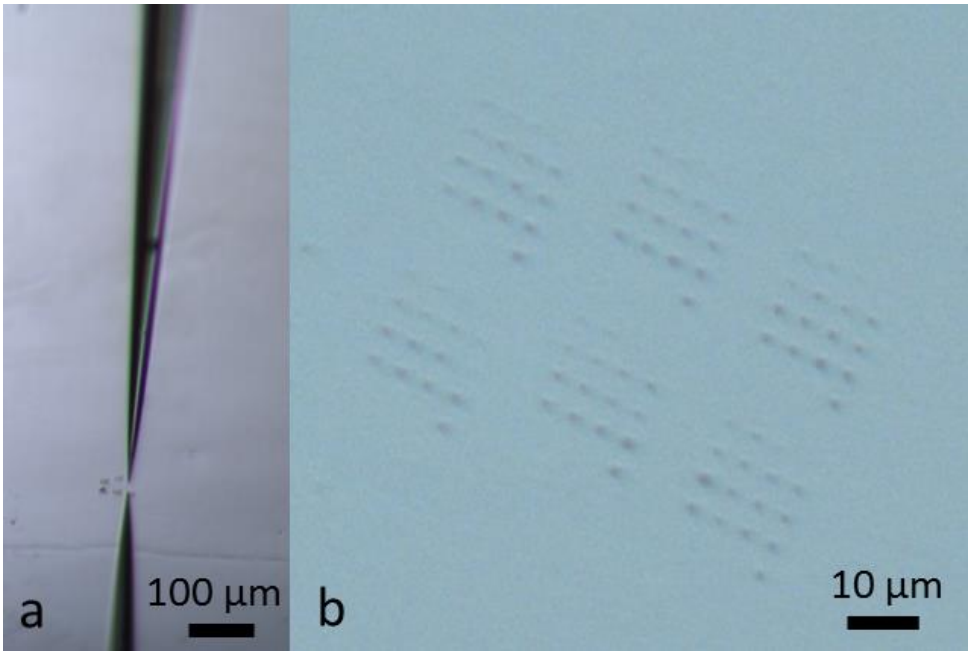

Figure 20 Optical images of: a) an experiment in progress; b) close up image of arrays of dissolution pits formed on a surface

2.3.4 Atomic Force Microscopy

The SECCM etch pits were characterized using a Bruker Nano Enviroscope AFM with a Nanoscope IV controller in tapping mode. We did not see any evidence of residues from the etching process or of solution being left behind after breaking meniscus contact. Tips used were 0.01-0.025 Ω-cm Sb doped Si cantilevers (Veeco). The resultant images were analysed using SPIP 6.0.10 software.

2.4 Theory and Simulations

A 3D finite element method (FEM) model was used to extract the acid induced dissolution rate of enamel. The theta pipette presents a symmetry plane perpendicular to the pipette septum such that it was possible to model only half a pipette, for computational efficiency, as illustrated in Figure 21. Values for the parameters used to describe the theta pipette geometry were typical values obtained from SEM images of the pipette: the major pipette radius perpendicular to the septum (*mpr* = 440 nm); the minor pipette tip radius parallel to the septum (*mptr* = 260 nm); septum width (*tw* = 74 nm), pipette semi-angle (*semi-ang* = 2.4°). The values used in Table 2 are the aqueous reference values as some of the species involved are transient and only exist in extremely low concentrations in the experimental conditions and thus are difficult to measure experimentally.

Table 2 Diffusion coefficients of key solution species.(280)

species	diffusion coefficient (*D*) ($cm^2\ s^{-1}$)	Charge (*z*)
Ca^{2+}	$0.792x10^{-5}$	2
HPO_4^{2-}	$0.759x10^{-5}$	-2
$H_2PO_4^-$	$0.959\ x10^{-5}$	-1
H_3PO_4	$0.882\ x10^{-5}$	0
H^+	$9.311\ x10^{-5}$	1

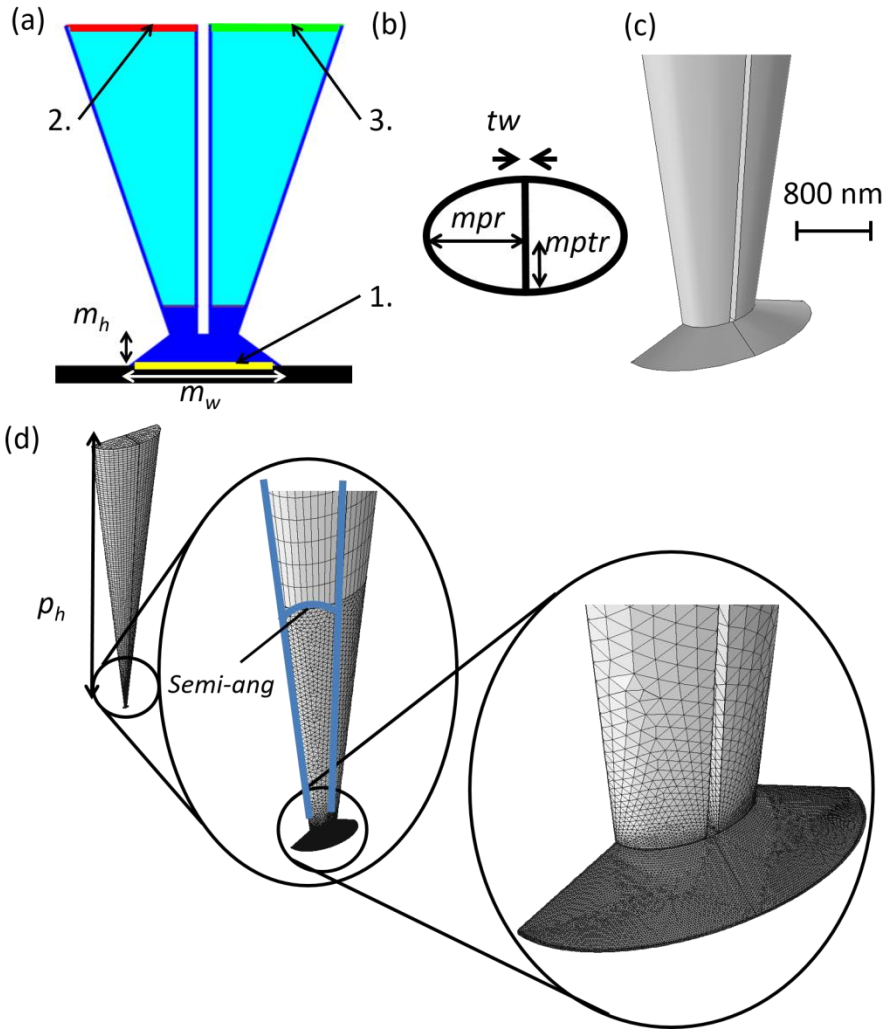

Figure 21 the pipette geometry used. (a) 2D representation of the 3D simulations. (b) 2D representation of the end of the pipette. (c) The simulation geometry used zoomed into the region of the meniscus. (d) 3D representation of a pipette probe in meniscus contact with a substrate showing the FEM grid used in experiments

For simplicity the simulation assumed a planar enamel surface due to the relatively shallow pits formed after etching, especially at the short times. However, the meniscus contact width (m_w) that is shown in Figure 21(a) was adjusted for each experimental time simulated, as informed from AFM data of etch pits. The meniscus height (m_h = 300 nm), and the

fraction of the potential that falls across the simulation boundaries (E_f) were determined by matching the ionic conductance current in the simulation (with an inert substrate surface) to the experimental barrel current of an approach to an inert silicon oxide wafer substrate.(275) The pipette height (p_h = 100 µm), which is the height of the tip domain that was simulated, was chosen to be sufficiently large so not to influence the results of the simulation.(277) All simulations were carried out using the FEM simulation software, Comsol Multiphysics (v4.3, Comsol AB) with LiveLink for Matlab (R2011a, Mathworks).

The Nernst-Planck equation (eq. 2) coupled with the electroneutrality condition (eq. 3) was solved to determine ionic concentration distributions in the pipette and meniscus domains:

$$\nabla.(-D_i\nabla \mathrm{c}_i - z_i u_i F c_i \nabla V) = R_i \qquad (2)$$

$$\sum_i z_i\, c_i = 0. \qquad (3)$$

where c_i is concentration, D_i is diffusion coefficient,(275) z_i is charge, u_i is ionic mobility (calculated based on the Einstein equation) of species *i, F* is the Faraday constant, and *V* is the electric field (between the 2 QRCEs), R_i indicates reactions leading to the formation or loss of species *i* within the field. Species in the solution were always kept at equilibrium, described by the following equations.

$$\begin{cases} \mathrm{H_3PO_4} \rightleftharpoons \mathrm{H^+ + H_2PO_4^-} & K_{a1}^* = \frac{[\mathrm{H_2PO_4^-}][\mathrm{H^+}]}{[\mathrm{H_3PO_4}]} \\ \mathrm{H_2PO_4^-} \rightleftharpoons \mathrm{H^+ + HPO_4^{2-}} & K_{a2}^* = \frac{[\mathrm{HPO_4^{2-}}][\mathrm{H^+}]}{[\mathrm{H_2PO_4^-}]} \end{cases} \quad (4)$$

where K_{1a}^{*} and K_{2a}^{*} are acid dissociation constants for H_3PO_4 and $H_2PO_4^-$, respectively, corrected for the ion activity coefficients using MINEQL$^+$ (Chemical Equilibrium Modelling System v4.6). In this simulation, convection from the electroosmotic flow was reasonably assumed to be negligible and so was not included because diffusion and migration play a much larger role under the experimental conditions.(234) As the experimental contact times (1-16 s) were much longer than the time needed to reach steady-state in the pipette, it was reasonable to assume steady-state dissolution for the simulation.(275)

The initial concentrations for Ca^{2+}, HPO_4^{2-}, $H_2PO_4^-$, and H_3PO_4 were assigned to zero in the simulated domain. The bulk concentrations, (*i*) were maintained at boundaries 2 and 3 (Figure 21(a)) with the following equation:

$$c_i = c_i * \qquad (5)$$

is initial concentration of species *i*. To simulate the bias, $0\ V$ was applied to surface 3 (one barrel), and E_f was applied to surface 2 (the other barrel).(275)

At the interface between the meniscus and the enamel surface, represented in 2D (Figure 21(a)) with surface 1 as enamel (yellow), a flux relation was applied to represent the dissolution process:

$$\begin{cases} -n.N_{Ca^{2+}} & = & k_0.[H^+].\left(\frac{10}{8}\right) \\ -n.N_{H_2PO_4^{2-}} & = & k_0.[H^+].\left(\frac{6}{8}\right) \\ -n.N_{H^+} & = & -\ k_0.[H^+] \end{cases} \quad (6)$$

where n is the inward unit vector and N_i is flux vector of species *i*, The intrinsic rate constant for dissolution is K_0.

The fractions $\left(\frac{10}{8}\right)$ and $\left(\frac{6}{8}\right)$ represents the stoichiometry coefficients of the acid dissolution reaction (eq. 1). All other boundaries, pipette walls and meniscus sides, were considered to be electrically insulating and have no flux (normal).

2.5 Results and Discussion

2.5.1 Etch Pit analysis

Six arrays (each comprising 16 etch pits) were generated on each of the four enamel samples for each treatment using the 1 mm HNO_3 etching solution. This resulted in 384 etch pits for each of the four treatment conditions, all of which were analysed using AFM. A representative AFM image of an array is shown in Figure 22. There is a noticeable trend towards deeper and wider dissolution pits with increased time. It can also be seen that SECCM dissolution results in highly localised dissolution at the position of meniscus contact with the enamel surface. The volume of the pits for each hold time was averaged across all the arrays and samples

to produce Figure 23(a), which shows pit volume against meniscus contact time for untreated enamel, F^- treated enamel, Zn^{2+} treated enamel and the combined treatment. These data highlight that the etch pit volume increases with time for all surface types, but the extent of dissolution is greatest for untreated enamel. Treatment of the surfaces inhibits the extent of dissolution, although the difference from the untreated samples was most noticeable at short times. This trend is also evident in the plot of pit depth vs. time (Figure 23(b)), with the treated surfaces showing much smaller pit depths overall, and for all surfaces the pit depth increasing with time.

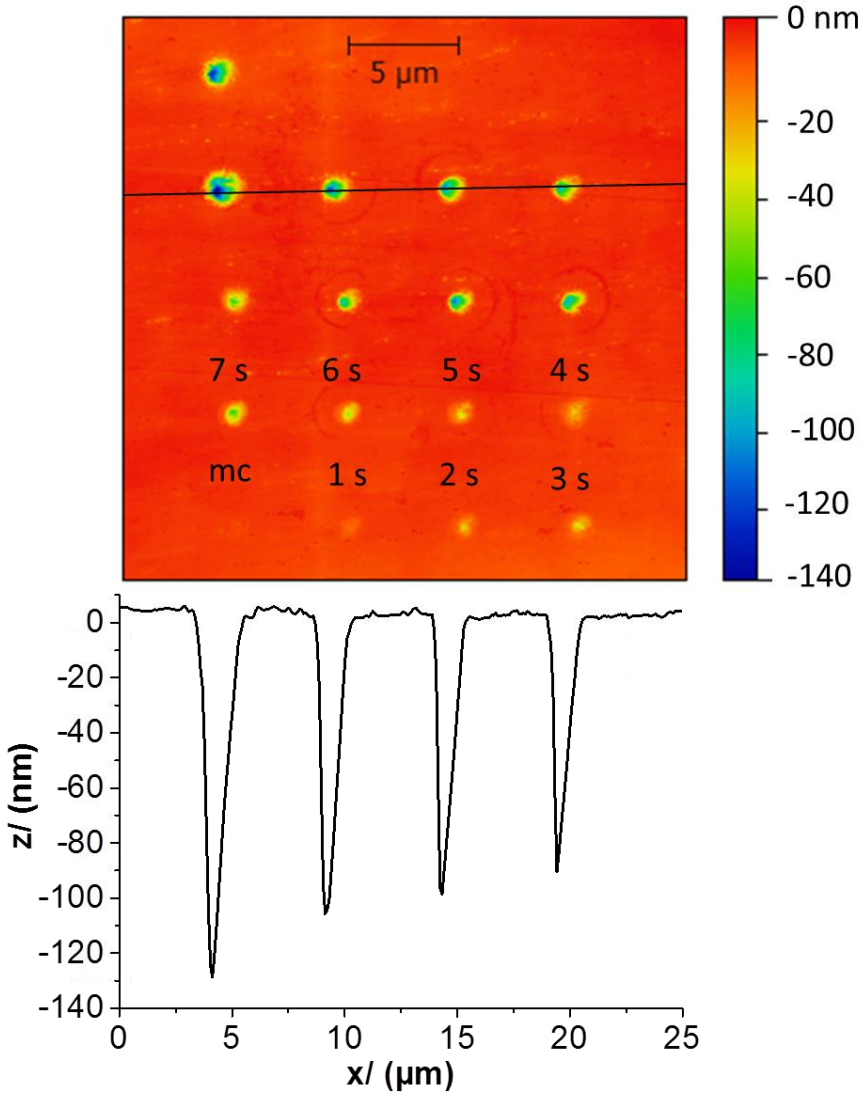

Figure 22 Typical array of untreated enamel etch pits formed using SECCM, with the times of meniscus contact noted. Black line marks point of the profile at the bottom of the AFM image. The first point only makes momentary contact (mc), used for orientation of the sample, acid dissolution at each position is for an increased time period

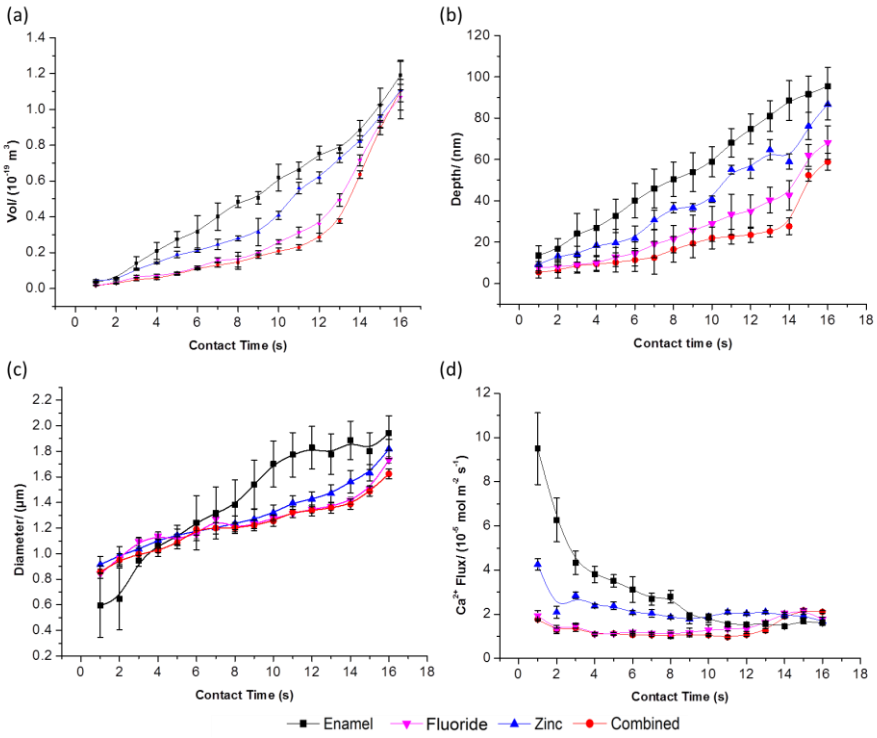

Figure 23 Plots of: (a) average etch pit volume, (b) average pit depth, (c) average pit diameter, (d) average Ca^{2+} flux as a function of time. Error bars show standard error of the mean, n=24. Curves through the points are to guide the eye

In order to elucidate quantitative dissolution rates, it was necessary to know the pit diameter (Figure 23(c)), which relates to the area of meniscus contact. The change in diameter, and thus the area of contact between the meniscus and the surface, was taken into account and inputted into the simulations used to analyse the data i.e. a time dependent meniscus area was considered to ensure that surface fluxes were determined with high accuracy (*vide infra,* e.g. Figure 23).

Overall, the treatments appear to show F^- treatment providing more protection of the enamel surface to acid attack than Zn^{2+} treatment, with the combined treatment providing the greatest protection. However, at longer

times, the treatments are less effective. This is because the treatments in Figure 23 only effect the surface layer of the enamel. The treatment does not penetrate substantially into the sample and protect the subsurface; this indicates these surface treatments are suitable if applied regularly.

The flux of Ca^{2+} (mol cm^{-2} s^{-1}) was determined using the time-dependent pit volume and area (calculated using SPIP 6.0.10 software) to calculate the molar amount of enamel removed (density of enamel is 3.16 g cm^{-3}, molar mass is 502 g mol^{-1}).(5, 10, 11, 13, 14, 281) The average flux for each contact time for the different enamel substrates is shown in Figure 23(d).

Table 3 Calculated intrinsic rate constants for the different enamel substrates. Error is standard error of the mean (n=384).

Sample	Intrinsic rate constant (k_0) for Ca^{2+} release (cm s^{-1})
Enamel	0.099 ±0.008
Zinc treated	0.058 ±0.007
Fluoride treated	0.033 ±0.008
Combined treated	0.025 ±0.005

All values are statistically different ($p < 0.01$) analysed by ANOVA and Tukey-Kramer analysis.

2.5.2 Simulations

The model described earlier was implemented to calculate Ca^{2+} fluxes as a function of k_0 which was varied in the simulations between $1x10^{-3}$ cm s^{-1} and $7x10^{-5}$ cm s^{-1}. The ratio of the diameter of contact area (obtained from AFM images of the pits, as described) to the diameter of the pipette was varied between 0.5 and 3. Figure 24 shows example concentration profiles for the key species involved in the acid attack and dissolution process for a rate constant, k_0=0.08 cm s^{-1}, which is at the upper end of those measured experimentally (*vide infra*). It can be seen that protons are significantly consumed at the enamel surface (interfacial concentration *ca.* 0.1 mM) but that, even with this rate constant, there is some contribution from surface kinetics, which can be determined. The profiles also show that there is some asymmetry in the transport of ions to and from the surface due to the electric field between the 2 QRCEs in the pipette.(275)

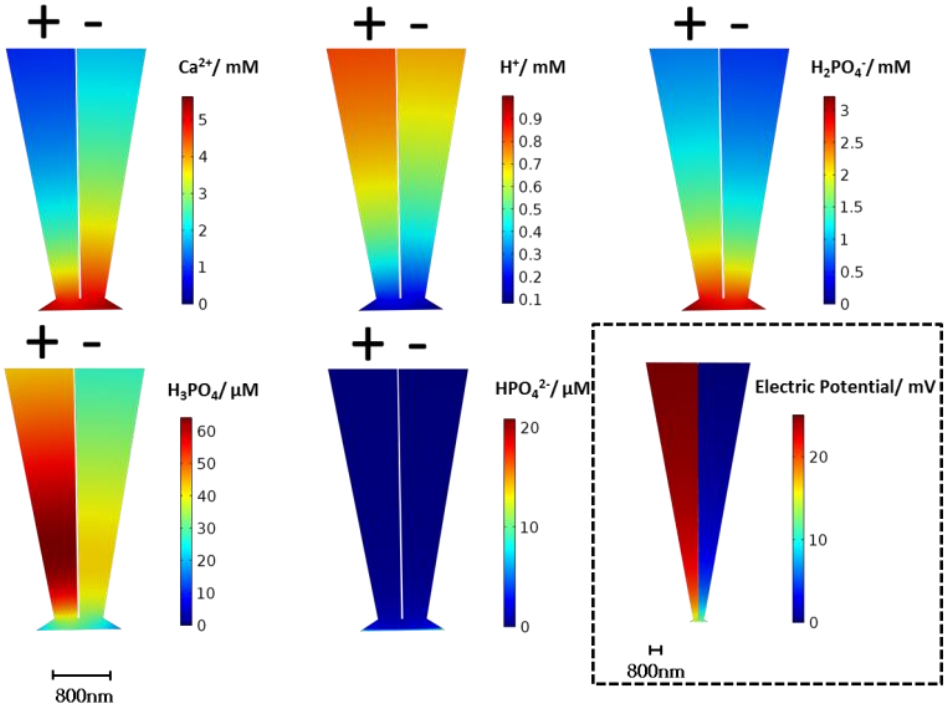

Figure 24 The concentration profiles of simulated species and electric potential at the end of the tip using an intrinsic rate constant, $k_{0,}$ of 0.08 cm s^{-1}.

2.5.3 Determination of dissolution kinetics

A 3-D working plot showing the interfacial calcium ion flux from the enamel surface as a function of the dissolution (acid attack) rate constant and ratio of meniscus radius to pipette radius ratio is shown in Figure 25. The experimental data yield j_{Ca}^{2+}, as described above, along with the area of meniscus contact, leaving the kinetic term, $k_{0,}$ which can then easily be determined. This calibration surface was used to derive the rate constant using the experimental results for all four treatment conditions and over all times. The average rate constant for each treatment is shown in Table 3. The result for the untreated enamel substrate is comparable to that of our

previous work, (0.1 ±0.05 cm s^{-1}) using a different technique giving great confidence in the technique.(39) In particular, it proves that there are no deleterious issues, for example, from solution that could have been left behind. As described above, it can be seen that F^- treatment is more effective than Zn^{2+}, and that the two combined gives the best barrier to acid attack of enamel. The variation between the rates constants for different treatments was proven to have statistical significance by using one-way analysis of variance (ANOVA) ($p = 2.9x10^{-9}$, 99%).

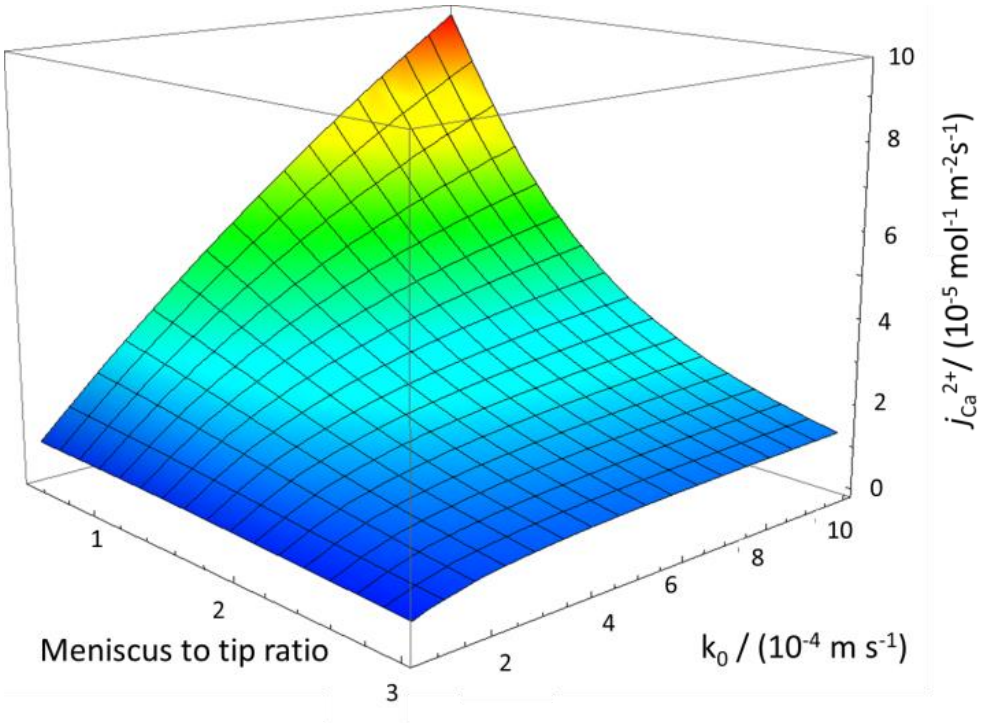

Figure 25 Simulated results showing Ca^{2+} flux (mol m^{-2} s^{-1}) vs. intrinsic rate constant of dissolution (m s^{-1}) vs. meniscus to tip ratio

2.6 Conclusions

This study has presented a new method of combinatorial localized dissolution analysis highlighting the ability of SECCM to make multiple, rapid, localized, and independent dissolution features on a surface, under conditions of highly defined and fast mass transport. Combined with AFM analysis of the resulting etched features, this provides a powerful platform to investigate surface processes. In the present study, by following the dissolution reaction with time, it has been possible to elucidate the efficacy of surface treatments on enamel dissolution, and how this changes during etching. With the additional information provided by FEM modelling, quantitative kinetic information about the surface reaction has been extracted.

This method has proven to be particularly powerful for the investigation of dental enamel surfaces, which may show some inter-sample variability. With this approach herein, a single sample can be subjected to multiple treatments in different locations and their relative efficacy assessed, removing inter-sample effects. A particularly powerful aspect of the technique is that dissolution can be monitored for very short times, which is very beneficial as surface treatments often provide only a thin, transient coating, as shown herein. We expect that this approach

could have myriad applications in the future for examining surface coatings and treatments. Although not exploited in this study, it should also be pointed out that dissolution can be monitored via the ion-conductance current during meniscus contact(277) which further enhances the capabilities of this technique.

For the systems studied, it has been found that both zinc and fluoride act initially to protect enamel from acid-induced dissolution, with fluoride having the greatest effect, whilst a combination of both treatments provided the optimum protection. This study demonstrates that the method outlined can be used to test treatments in a high throughput, automated approach to test single and multiple (combination) treatments of a surface quickly and effectively.

3 Measurement of the efficacy of calcium silicate for the protection and repair of dental enamel

3.1 Abstract

3.1.1 Objectives:

To investigate the formation of hydroxyapatite (HAP) from calcium silicate and the deposition of calcium silicate onto sound and acid eroded enamel surfaces in order to investigate its repair and protective properties.

3.1.2 Methods:

Calcium silicate was mixed with phosphate buffer for seven days and the resulting solids analysed for crystalline phases by Raman spectroscopy. Deposition studies were conducted on bovine enamel surfaces. Acid etched regions were produced on the enamel surfaces using scanning electrochemical cell microscopy (SECCM) with acid filled pipettes and varying contact times. Following treatment with calcium silicate, the deposition was visualised with FE-SEM and etch pit volumes were measured by AFM. A second set of bovine enamel specimens were pre-treated with calcium silicate and fluoride, before acid exposure with the

SECCM. The volumes of the resultant acid etched pits were measured using AFM and the intrinsic rate constant for calcium loss was calculated.

3.1.3 Results:

Raman spectroscopy confirmed that HAP was formed from calcium silicate. Deposition studies demonstrated greater delivery of calcium silicate to acid eroded than sound enamel and that the volume of acid etched enamel pits was significantly reduced following one treatment ($p<0.05$). In the protection study, the intrinsic rate constant for calcium loss from enamel was 0.092±0.008 cm/s. This was significantly reduced, 0.056±0.005 cm/s, for the calcium silicate treatments ($p<0.0001$).

3.1.4 Conclusions:

Calcium silicate can transform into HAP and can be deposited on acid eroded and sound enamel surfaces. Calcium silicate can provide significant protection of sound enamel from acid challenges.

3.1.5 Clinical Significance

Calcium silicate is a material that has potential for a new approach to the repair of demineralised enamel and the protection of enamel from acid attacks, leading to significant dental hard tissue benefits.

3.2 Introduction.

Although the prevalence of dental caries has declined over the last four decades, due to the increasingly widespread use of fluoride toothpastes and improvements in oral hygiene practices, this painful and debilitating condition is still of major importance.(282) Likewise, the need for teeth to last longer due to increases in life expectancy, and the detrimental effects of increases in the consumption of acidic drinks, has increased concerns about tooth wear, particularly acid erosion.

While both caries and erosion are the results of mineral loss due to acids, their aetiologies are very different. Caries is the result of plaque bacteria metabolising fermentable sugars to produce acids which progressively remove mineral beneath the relatively intact tooth surface, so that a lesion develops and grows within the tooth enamel. Conversely, erosion is caused by direct contact between dietary acids and the tooth surface, so mineral is initially lost from the surface, but further loss continues over time from the newly exposed mineral as the old surface dissolves. The acids responsible for erosion can also come from the stomach, where the patient suffers from, for example, an eating disorder or an illness that causes regurgitation, or occasionally from the environment, such as the occupational exposure for swimmers.(15)

The ability of fluoride to reduce dental caries is long established where fluoride has been shown to both provide some protection from acid

challenges and to repair demineralised enamel.(26, 50, 283-285) Toothpaste manufacturers have sought to improve the efficacy of their products by enhancing fluoride delivery or adding other therapeutic agents. Increased erosion protection has been reported for stannous fluorides that are claimed to form a barrier layer on top of enamel, which protects it from acid challenge (286), but the efficiency of remineralisation (287) in the presence of such a barrier is unclear. Remineralisation is a naturally occurring process in the mouth, in which the saliva provides a source of phosphate and calcium ions needed for the formation of HAP.(27)

The addition of calcium-containing minerals to fluoride containing toothpaste is another approach to enhancing the remineralisation and protection benefits.(27, 284) These minerals can elevate the level of calcium in both plaque and saliva, which may reduce the chance of caries and contribute to reducing the rate of enamel demineralisation, while promoting enamel remineralisation. Elevated calcium levels have been shown to increase fluoride levels in plaque and saliva (288), which can also have a beneficial effect.(289) Furthermore, the retention of calcium minerals in the mouth after brushing can provide some pH buffering, and confer a degree of protection against subsequent acid challenges.(27)

Calcium-containing materials that have previously been used include hydroxyapatite (290, 291) and calcium sodium phosphosilicate bioglasses.(292) Bioglasses were first developed to repair bone injuries suffered by US servicemen during the Vietnam War (293), and have since

been used in toothpastes to reduce hypersensitivity (294) via the formation of a hydroxycarbonate apatite layer.(295) More recently, calcium silicate minerals were shown to be an active ingredient for both remineralisation (53) and the prevention of demineralisation.(296)

A new oral health technology has been developed based on the combination of calcium silicate, sodium phosphate salts and fluoride. The technology is proposed to augment the natural mineralisation processes of saliva by nucleation of HAP and the formation of tooth enamel minerals. The proposed mechanism can help to repair acid-softened enamel and to protect sound enamel from acid challenges, giving overall enamel health benefits.

Studies of acid induced enamel dissolution follow the process either by surface or bulk solution analysis.(30, 35) These studies have identified some of the key factors in enamel dissolution, namely that the rate is directly linked to the solution pH, with the rate of HAP dissolution typically inversely proportional to the proton concentration. The presence of calcium and phosphate ions can cause slower dissolution of enamel due to a lower degree of undersaturation.(47, 297) It has been demonstrated that the rate and extent of acid dissolution of enamel is strongly dependent on the diffusion of species towards and away from the surface, so that diffusion at the surface being investigated is controlled.(29, 30, 32, 35, 37, 298) More recently, several different microscopy techniques have been used to investigate localized acid-induced dissolution of enamel (41, 44, 211,

212) including atomic force microscopy (AFM) (42, 45), transmission electron microscopy (TEM) (263), profilometry (12), field emission-scanning electron microscopy (FE-SEM) (264, 299), and nano-indentation.(40) These have provided detailed views of the surface structural changes that accompany dissolution.

The aims of the current study are several fold. First, the calcium release profiles of calcium silicate were investigated and its transformation into HAP under different pH conditions was elucidated. Then the treatment of sound and eroded enamel surfaces with calcium silicate was studied to demonstrate protection and repair using a range of techniques, including with a scanning electrochemical cell microscope (SECCM).(210) This novel technique confines the area of acid attack within a single moveable droplet of acid, which can be positioned on the enamel surface with precise time and spatial control and allows multiple measurements to be made across a surface.(210, 234) The etch pits produced from the acid attack can be measured by AFM. This method also allows the quantitative analysis of the dissolution kinetics due to the controlled mass transport within the probe geometry (241), which can be described with a finite element method (FEM) model.(235, 277) The effect of treating the surface of the enamel before dissolution with both fluoride and calcium silicate is investigated and the effect on the rate of dissolution observed. The ability of calcium silicate to repair acid damaged enamel is shown via AFM analysis after treatment with calcium silicate in combination with a phosphate buffer. The hypotheses to be tested are (1) HAP is formed from calcium silicate; (2)

calcium silicate can be deposited onto acid eroded enamel to provide potential repair, and (3) calcium silicate can provide protection of sound enamel from acid challenge.

3.3 Materials and Methods

3.3.1 Calcium release from calcium silicate

Calcium silicate (1 mg/ml) was slurried in phosphate free buffer solutions (2-[4-(2-hydroxyethyl)piperazin-1-yl]ethane sulfonic acid (HEPES), potassium hydrogen phthalate, sodium tetraborate, and adjusted at the desired pH (pH 4, 7 and 10) using sodium hydroxide (n=5). The release of calcium was measured *in situ* using a calibrated calcium ion selective electrode (Ca-ISE,) at one minute intervals for up to 10 minutes and *ex situ* using inductively coupled plasma optical emission spectrometry (ICP-OES) (Perkin-Elmer Optima 5300 DV) after 10 minutes only (n=5).

3.3.2 HAP formation from calcium silicate

A set of calcium silicate slurries were prepared by mixing 1 mg/ml calcium silicate with phosphate buffers 0.1 M at pH 4, 7 and 10. After seven days, the slurries were filtered and washed to remove any residual phosphate salt, dried on filter paper and compacted using a pill press. The pH of each solution was monitored using a pH probe (Denver instruments UB-10) to confirm stable pH values were maintained over the seven days.

Untreated calcium silicate was also compressed into a pill as a control sample. Micro-Raman spectra were collected from the compressed pill samples using a Raman microscope (Renishaw, UK) fitted with a Charge Coupled Device (CCD) detector and a 633 nm HeNe laser using 5% attenuation and a spot size of 3 pm. A 50X lens was employed.

3.3.3 Scanning electrochemical cell microscopy (SECCM)

Enamel repair and protection were investigated using SECCM. The SECCM used was a custom-built machine controlled by a custom LabVIEW 2011 program (National Instruments).(210, 234, 235, 241, 277) The tip position was controlled using piezoelectric positioners with a movement range of 38 μm in the *z*-axis (P-753.3CD positioner, Physik Instrumente, Germany) and 300 μm in the *x*- and *y*-axes (Nano-Bio300, Mad City Labs, USA). Potentials were applied using a custom built potentiostat controlled by the LabVIEW 2011 program through a field programmable gate array (FPGA) card (PCI-783R, National Instruments, UK).

Dual-barrel (theta) capillaries (diameter 1.5 mm) made of borosilicate glass (Harvard Apparatus, UK) were pulled to a sharp taper using a P-2000 IntraCel laser puller (Sutter Instruments Co., USA), producing two closely identical (mirrored) pipettes. One pipette was employed for SECCM experiments and the other was imaged by a FE-SEM

to ascertain the diameters at the tip apex (approximate 4 μm diameter). In other experiments pipettes of different sizes were used as discussed below.

An oscillation (233.5 Hz frequency, 80 nm peak-to-peak amplitude) was applied to the *z* position onto which the pipette was mounted, using a lock-in amplifier (SR830DSP, Stanford Research System, USA). To aid positioning of the tip close to the surface of the enamel specimens, a mechanical winder was employed aided by visualisation with a camera.(277)

All experiments used 50 mM KNO_3 and 1 mM HNO_3 (pH 3) in each barrel of the pipette. An Ag/AgCl quasi-reference counter electrode (QRCE), made by chloridising a 0.25 mm silver wire (MaTecK, Germany) in saturated KCl (Sigma-Aldrich, UK) solution was employed in each barrel to form the electrochemical cell. A bias of 0.25 V was applied between the two electrodes to introduce an ion current flow. The final approach of the pipette to the surface was made with the *z* piezo positioner, which stopped approximately when the generated alternating current changed by an order of magnitude from the value in air.(277) The system allows a constant distance between the tip and the sample surface to be maintained.(210, 234, 235, 241, 277)

The acid droplet was held in contact with the enamel surface for a set period of time before being withdrawn using the SECCM controller. An example FE-SEM image (end on view) of the type of tip used is shown in Figure 26a. Figure 26b shows a simple diagram of part of the experimental

set-up used. An approach-hold-withdraw cycle was conducted for each pit created with a varying hold time of the meniscus on the surface, typically starting at 1 s, after a prior momentary contact for array alignment in subsequent visualisation, followed by increments of 1 s at each later point up to a total of 16 s. Figure 26c shows a representation of a grid used to generate an array of etched pits on an enamel surface. The grids were repeated 4 times on each enamel sample.

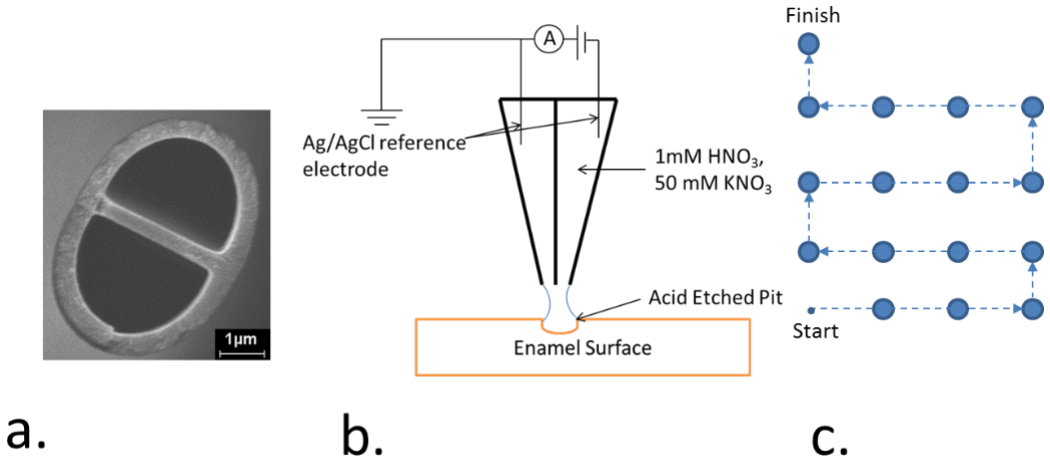

Figure 26 (a) FE-SEM showing 2 barrel pipette geometry. (b) Experimental set up used showing an acid filled pipette in contact with an enamel surface. (c) Representative pit array created in SECCM experiments. Arrows show probe path. Droplet is held in contact with each spot for defined time periods of 1 s – 16 s (1 s increments). For the very first spot there is only momentary meniscus contact for orientation of the array

3.3.4 Deposition of calcium silicate onto sound and eroded enamel surfaces

Bovine enamel blocks (6×6 mm) were polished to a 3.0 µm root mean squared (RMS) roughness, as confirmed by AFM. These were further polished on polishing pads with diamond lapping particles starting with 6 µm and progressing to 50 nm particles (Buehler, Germany), resulting in a final surface roughness of 1.5±0.6 nm RMS. The enamel was mounted on an AFM puck for ease of handling. An area of each enamel block was acid eroded using the SECCM technique as previously described, using a tip with a 200 µm diameter and containing 50 mM KNO_3 and 1 mM HNO_3 for 120 s. This generated an acid eroded surface on the enamel with a

diameter of approximately 200 μm, leaving significant sound enamel areas to act as an internal control for each specimen. Calcium silicate was applied to the enamel blocks (n=4) by gently rubbing the enamel surface in circular motions with the calcium silicate slurry, in phosphate buffer 0.1 M at pH 7, on a Microcloth polishing pad (Buehler, Germany) for 2 minutes. Following water rinsing, the specimens were dried and prepared for FE-SEM analysis.

3.3.5 Deposition of calcium silicate to eroded enamel pits

Calcium silicate deposition to eroded enamel pits was explored using polished bovine enamel blocks as previously prepared. An array of acid eroded pits was etched onto the surface of the enamel using SECCM as described above with a contact time that varied from 1–9 s, with 1 s intervals. A 1 μm diameter pipette was used to create the pits in this instance. Topographical imaging of the eroded enamel pits was carried out using tapping mode AFM (Bruker Nano Enviroscope AFM with a Nanoscope IV controller, UK). The tips used were 0.01-0.025 Ω-cm Sb doped Si cantilevers (Veeco, USA). The etch pit volumes were measured using SPIP 6.0.10 software. Enamel specimens were then treated with a slurry of calcium silicate (1 mg/ml) in phosphate buffer (pH 7) for 2 minutes with agitation followed by water rinsing.

The volume of the treated etch pits was again measured by AFM. The percentage change in etch pit volume was calculated using the following equation:

$$Percentage\ change = \frac{Original\ Volume - Treated\ Volume}{Original\ Volume}\ X100$$

3.3.6 Protection of enamel by calcium silicate and fluoride

Two sets of polished bovine enamel blocks were prepared as described in section 2.3, 4 blocks per set. For each enamel block the surface was half-masked using low tack polyester tape (3 M, UK). Both sets of blocks were immersed in a solution of sodium fluoride (1000 ppm F^-) for 2 minutes before rinsing in deionised water. The mask was removed and then one set of blocks was treated with a calcium silicate slurry (1 mg/ml) in phosphate buffer (pH 7) for 2 minutes as described in section 2.3. The second set of blocks received no further treatment. The preparation procedure is schematically shown in Figure 27. Thus, a set of enamel specimens were prepared in which the surfaces were either untreated, treated with fluoride alone, treated with calcium silicate alone or treated with both fluoride and calcium silicate (n=4). Arrays of acid etch pits were then generated on the enamel specimens using the SECCM as previously described, with contact time between 1 and 16 s, with a 1 s interval. For

each untreated and various treated areas, four arrays were produced. The volume and contact area of the etch pits were measured using AFM from which the flux of enamel dissolved was calculated. A set of detailed simulations, 44 was carried out using the experimental data to obtain the intrinsic rate constant of calcium loss.

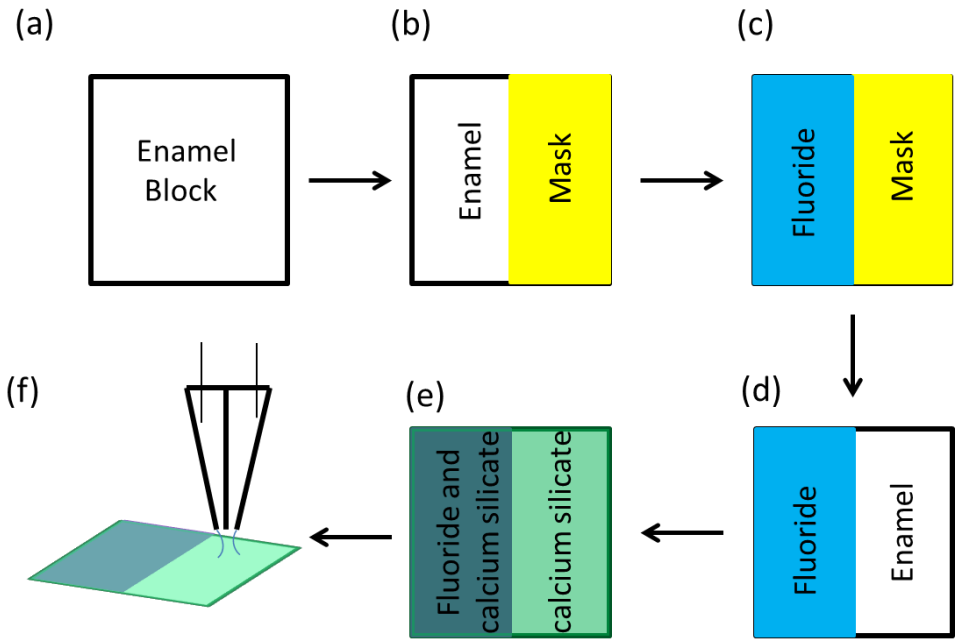

Figure 27 The preparation steps used to prepare an enamel sample for the protection experiments. (a) A polished enamel sample was used. (b) Half the sample was masked off. (c) The sample was treated with 1000 ppm F^- for 2 minutes. (d) The mask was removed. (e) The whole sample was treated with calcium silicate slurry. (f) The sample was used in SECCM experiments.

3.4 Results

3.4.1 Calcium release from calcium silicate

Calcium release profiles measured by Ca-ISE at differing pH values are shown in Figure 28. The initial release of calcium is rapid within the first minute. Maximum release is approached after 5 minutes with little further change in calcium concentration up to 10 minutes. ICP-OES analysis confirms the amount of Ca^{2+} released after 10 minutes; the data are

summarised in Table 4 Comparison of Ca2+ release concentration via ICP-OES and ISE (n = 5). The data show a small pH dependence of the release process with higher calcium release at low pH.

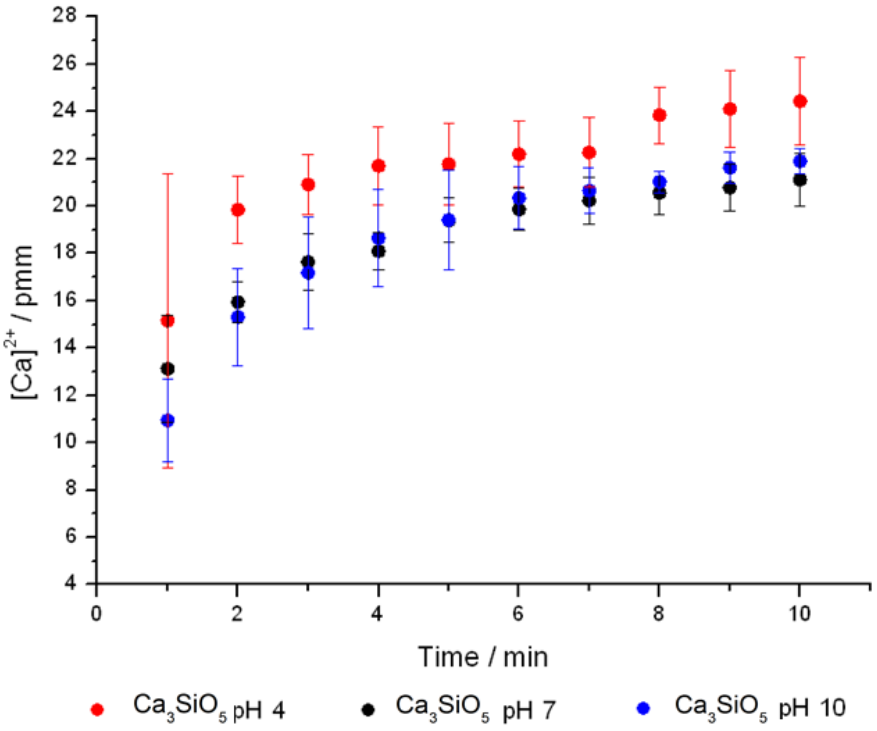

Figure 28 Calcium release profile of 1 mg/ml calcium silicate in phosphate free buffers at pH 4, 7 and 10 using Ca^{2+} ISE

Table 4 Comparison of Ca^{2+} release concentration via ICP-OES and ISE (n = 5)

	Ca^{2+} release ppm		
	pH4	pH 7	pH10
ICP-OES	22.5 ±0.15	23.6±0.15	18.3 ±0.6
ISE	24.4 ±1.8	21.0 ±1.1	21.9 ±0.5

3.4.2 HAP formation from calcium silicate

Figure 29a shows the Raman spectrum of the calcium silicate control. The material is mostly amorphous calcium silicate and as expected the spectrum does not present any characteristic features. Figure 29b shows spectra of the calcium silicate treated with phosphate buffers at different pH values. All spectra show similar features. The position of the peaks are characteristic for the vibration, bending and stretching of phosphate groups and the position of these peaks is attributable to either HAP or *β*-tricalcium phosphate (TCP). In order to distinguish between the two compounds, more detailed analysis of the spectra is necessary. Figure 29c shows the spectra of a polished enamel block, a TCP pill and a calcium silicate pill after treatment at pH 7. TCP and enamel (HAP) produce similar Raman spectra, dominated by the PO_4^{3-} internal modes. However, their different crystallographic structure gives rise to significant differences in the

shifts and splittings of the V_1, V_2, V_3 and V_4 bands.(219, 238) In the case of enamel, the V_1 and V_2 bands are noticeably narrower and have a larger separation than for TCP (ca. 120 cm−1 vs. ca. 50 cm−1, respectively).(219, 238) For HAP, V_1 is a singlet with a shoulder and V_2 appears as a doublet-doublet while for TCP V_1 appears as a doublet with shoulder and V_2 as a multiplet. For HAP the V_3 peak appears as a singlet, while for TCP it appears as a singlet with a shoulder. V_4 is broader for HAP with a lower frequency Raman shift. The spectrum of the calcium silicate after treatment shows all of these features and direct comparison with the spectra collected from freshly polished enamel (and TCP) shows a convincing similarity, proving conclusively the formation of HAP on the calcium silicate pill after treatment in pH 7 phosphate buffer.

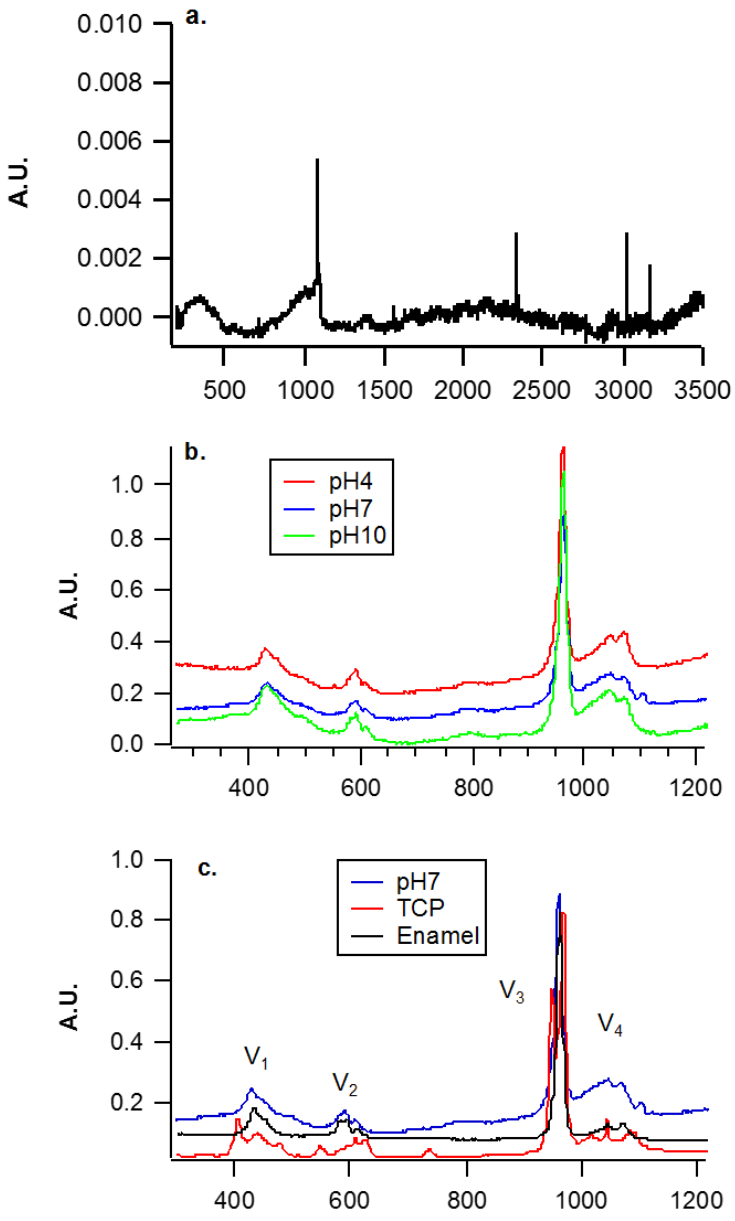

Figure 29 Raman spectra of (a) calcium silicate untreated (b) calcium silicate treated in phosphate buffers pH 4, 7 and 10 and (c) a comparison of calcium silicate treated in phosphate buffer pH 7, enamel and TCP

3.4.3 Deposition of calcium silicate onto sound and eroded enamel surfaces

Figure 30 shows typical FE-SEM images of (a) polished and (b) acid etched surfaces after treatment with calcium silicate. These show that the distribution of particles over the surface is random. However, the main difference between the samples is that the acid etched sample had a much higher coverage than the polished sample.

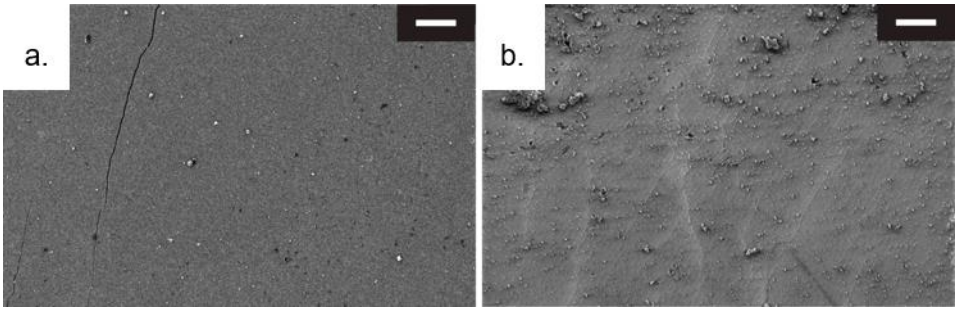

Figure 30 FE-SEM imaging of the deposit morphology of calcium silicate on (a) polished and (b) etched enamel. Scale bars are 20 µm

3.4.4 Deposition of calcium silicate to eroded enamel pits

Figure 31 shows an AFM image of a typical array of pits etched into polished enamel using SECCM. The pit volumes, as a function of time, before and after treatments with calcium silicate are shown in graphical form in Figure 32. Small pits, generated by acid exposure times of less than three seconds, were excluded from this analysis as pit volume determination is more accurate for well-defined pits at longer exposure

times. Table 5 Percentage change of repair at each contact time after treatment with calcium silicate. The error is calculated as standard error of the mean (n=4). summarises the percentage change at each contact time and shows clearly the reduction in pit volume after treatment. The reductions in pit volume are significant, with an average pit volume reduction of 77±12% observed over the whole data set.

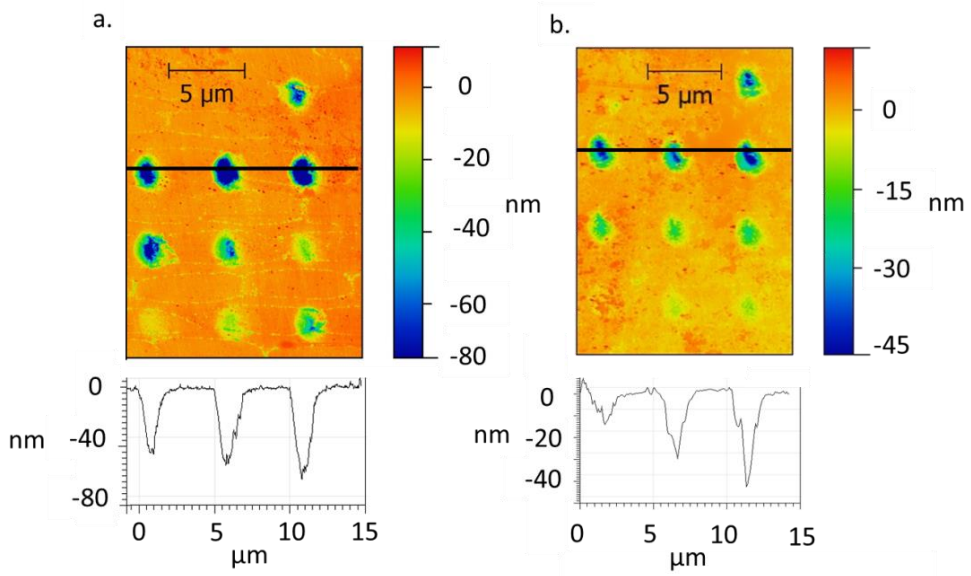

Figure 31 AFM of an SECCM produced array using 1 µm diameter pipette with 1 mmol HNO_3 solution (a) before and (b) after treatment with calcium silicate. Lines across the images show approximate locations of the profiles. Pits produced for contact times of 1 s -9 s (1 s intervals) plus momentary first contact for alignment

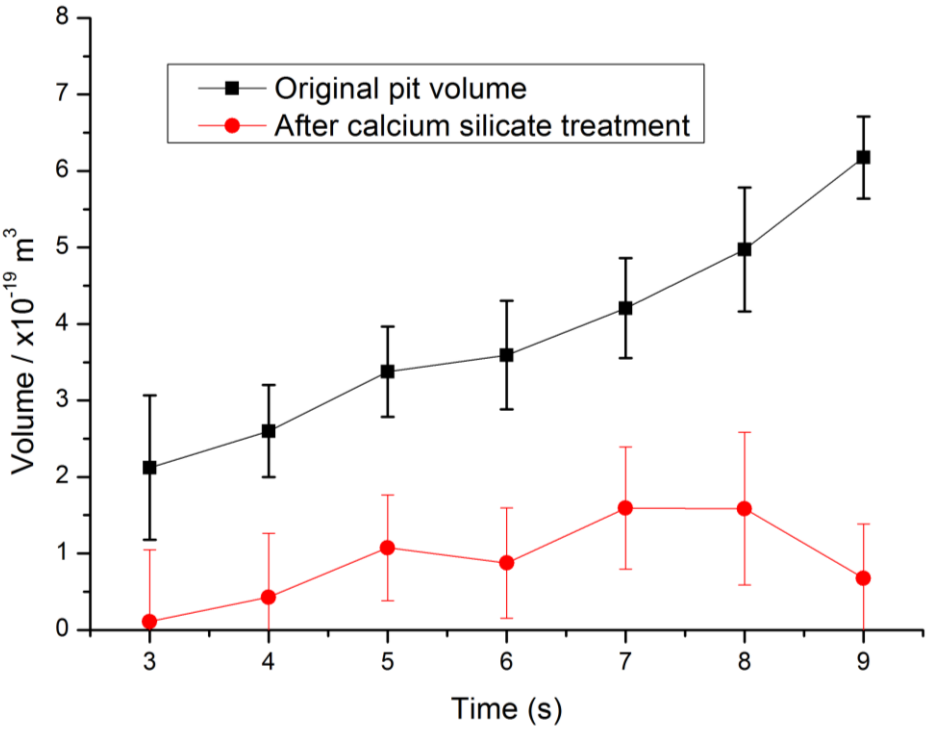

Figure 32 Pit volume at given contact time before and after treatment with calcium silicate. The error bars are calculated as standard error of the mean (n=4)

Table 5 Percentage change of repair at each contact time after treatment with calcium silicate. The error is calculated as standard error of the mean (n=4).

Contact time (s)	% change after treatment
3	90 ± 10
4	83 ± 15
5	68 ± 7
6	78 ± 10
7	62 ± 9
8	65 ± 11
9	89 ± 6

3.4.5 Protection of enamel by calcium silicate and fluoride

The volume of the pits produced using SECCM on different prepared enamel with treatments were measured using the AFM. The

volume of material loss was used to calculate the flux of enamel dissolution at the interface between the enamel surface and the etching solution for each contact time. Figure 33 shows the enamel flux for untreated enamel compared to the three treatments – calcium silicate, fluoride, calcium silicate plus fluoride. Each data point is the average over 16 pits (4 blocks and 4 arrays per treatment), the outliers have been excluded (minimum number of data averaged per time point is 14). Figure 33 shows a clear decrease of surface flux for each of the treated samples corroborating that all treatments provide some protection against acid erosion. While the flux gives a clear indication of protection from the treatment, in order to obtain the intrinsic rate constant and decouple the effect of mass transport the FEM model was used to determine the intrinsic acid etch rate from which the calcium flux from the enamel surface was defined. The intrinsic rate constant, k, for the different treatments are summarised in Table 6. The flux of calcium from the enamel surface is the product of the near-interface proton concentration and heterogeneous rate constant, taking into account the stoichiometry of the reaction in which 8 protons react to release 10 Ca^{2+} ions.(297) It is clear the 3 different treatments provide different degrees of protection. The average rate constants are calculated over the first 10 s. At long exposure times (contact time >10 s, data not reported) the benefit is no longer apparent, the rate constant of all treated samples converge closer to the untreated samples suggesting, in this model and under these experimental conditions, that the protection arises from a

surface effect and that once the surface has been breached, erosion proceeds in the normal manner.

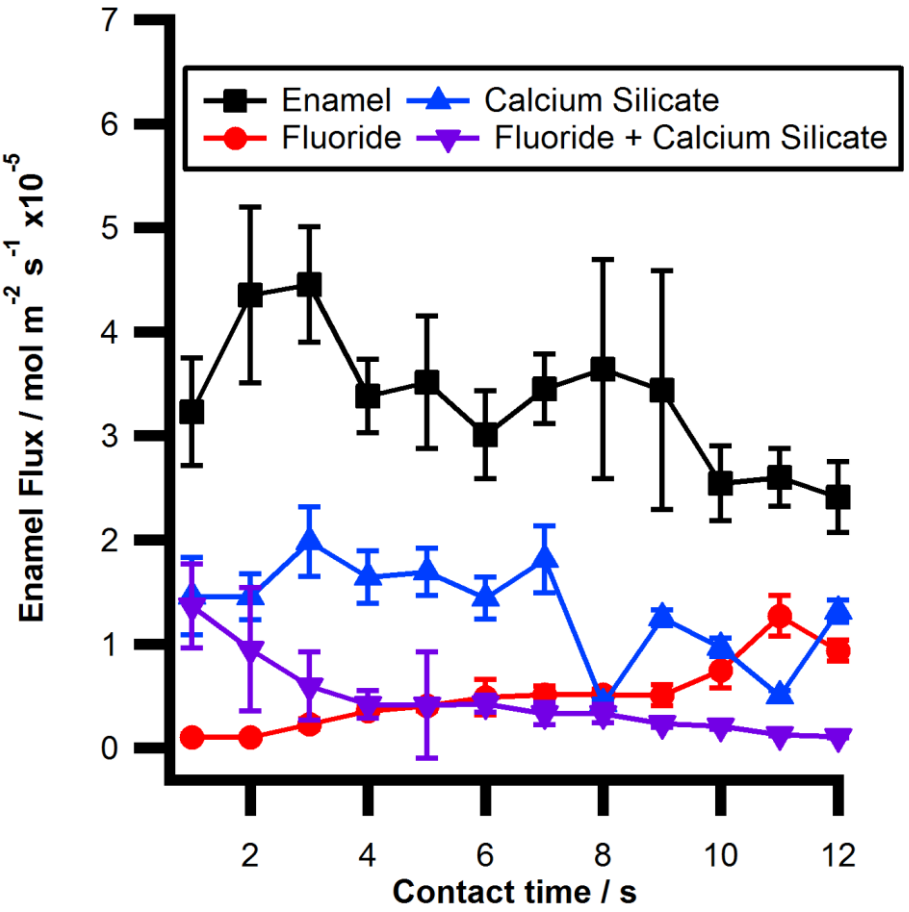

Figure 33 Flux of enamel at the enamel/aqueous interface at a given contact time. The error bars are calculated as standard error of the mean (n=16)

Table 6 The calculated intrinsic rate constants of calcium loss for each treatment. The error is standard error of the mean (n=10)

Sample	Intrinsic rate constant (cm/s)
Enamel	0.092 ± 0.008^{a}
Fluoride	0.026 ± 0.004^{b}
Calcium silicate	0.056 ± 0.005^{c}
Calcium silicate and Fluoride	0.0063 ± 0.0002^{d}
*** Values with different letters are statistically different ($p < 0.05$): letters denotes statistical comparison for different treatments by ANOVA and Tukey-Kramer analysis.**	

3.5 Discussion

The Raman spectra obtained from calcium silicate following treatment with phosphate buffers at pH 4, 7 and 10 all showed characteristic peaks unequivocally attributable to the formation of HAP after 7 days. The HAP formed had a similar spectrum to an enamel specimen and the comparison with the TCP spectrum was consistent with a literature study.(238) It is interesting to observe that HAP formation occurred at all bulk pH values examined and was not limited to pH>5.5 as might have been expected due to the dissolution that takes place in acidic conditions.(300) It is postulated that the rapid release of Ca^{2+} from calcium silicate is the result of an ion exchange process of the type postulated in the bone growth literature. This suggests a mechanism involving templating

by SiO groups with a local pH and geometry that favours the nucleation and formation of HAP even when the bulk pH is as low as pH 4.

Similar studies using Fourier transform infrared spectroscopy (FTIR) measurements have also demonstrated the formation of calcium phosphate crystalline phases from calcium silicate dispersed in phosphate solutions for 3 hours.(301) In addition, other *in vitro* and *in situ* experiments using transmission electron microscopy and selected area electron diffraction techniques have identified HAP formation on enamel surfaces following their brushing with a calcium silicate containing toothpaste formulation.(301) Thus, there is a strong body of evidence for the formation of HAP from calcium silicate.

The deposition and retention of calcium silicate particles onto enamel surfaces has been demonstrated from the FE-SEM data. In particular, more calcium silicate was deposited onto the acid eroded enamel areas than on sound enamel areas. Similarly, using the SECCM and AFM techniques, the volume of acid etched enamel pits was significantly reduced following one treatment with the calcium silicate slurry. This enhanced deposition onto eroded enamel is clearly beneficial in terms of possible repair mechanisms of eroded enamel by calcium silicate. Indeed, formulations containing calcium silicate, sodium phosphate salts and fluoride have been shown to more effectively remineralise eroded enamel compared to fluoride control formulations *in vitro.*(28)

The ability of calcium silicate to protect enamel from an acid challenge has also been demonstrated using the SECCM and AFM techniques. The deposition of calcium silicate particles after a single treatment is sufficient to reduce the intrinsic rate constant of calcium loss from the enamel surface by approximately 39% when compared to a non-treated control enamel surface. The intrinsic rate constant for the non-treated enamel is similar to that reported by McGeouch *et al*.(44) Under the current experimental conditions and methods, a sequential treatment of fluoride followed by calcium silicate gave a further reduction in the intrinsic rate constant of calcium loss. For the combination treatments, this was an order of magnitude lower than the non-treated control enamel surface and was significantly lower than the fluoride treatment alone. Thus, the potential for calcium silicate to give enamel protective benefits has been demonstrated using the current experimental set up. It is postulated that the protective properties of calcium silicate may be due to a combination of its calcium release profile, pH buffering capability and the formation of sacrificial HAP. In addition, a toothpaste formulation containing calcium silicate, sodium phosphate salts and fluoride has been shown to reduce the enamel demineralisation potential of acids over control formulations in a series of *in vitro* studies.(28)

3.6 Conclusions

The SECCM technique described here is a new method designed for the study of ionic crystal dissolution kinetics which clearly has considerable scope to study dental materials.(277) A key feature of the technique is that the sample is only exposed to the solution where the meniscus makes contact, and that measurements can be made with millisecond time resolution, opening up the possibility of studying materials with a wide range of solubilities and particularly highly soluble crystals. A further strength of the technique is that, in combination with FEM simulations, it is amenable to a high level quantitative description of mass transport and surface kinetics, as evident from the studies herein where comparisons made to the results from literature show good agreement.

The formation of HAP from calcium silicate dispersed in phosphate buffers at pH 4, 7 and 10 has been unequivocally demonstrated by Raman spectroscopic analysis of the resulting solids. Calcium silicate was shown by FE-SEM to deposit more on acid etched than sound enamel surfaces and has the ability to reduce the volume of acid etched pits in enamel surfaces, as determined by SECCM and AFM techniques. The enamel protective role of calcium silicate towards acid challenge was demonstrated, again using the SECCM and AFM techniques. Thus, we can formally accept the three hypotheses: (1) HAP is formed from calcium silicate; (2) calcium silicate can be deposited onto acid eroded enamel to

provide potential repair, and (3) calcium silicate can provide protection of sound enamel from acid challenge.

4 Controlled Crystallization in a Nanopipette

4.1 Abstract

Nanopipettes are becoming increasingly versatile tools for a diverse range of sequencing, sizing and imaging applications. Herein, the use of nanopipettes to induce and monitor crystallization and dissolution in real time is considered, using the precipitation of $CaCO_3$ in aqueous solutions as an exemplar system. The approach is to use the bias between a quasi-reference counter electrode (QRCE) in a nanopipette filled with solution containing sodium bicarbonate and a QRCE in a bulk solution containing calcium chloride to mix the two solutions locally by ion migration and drive either growth or dissolution depending on the polarity of the applied bias. Furthermore, Raman spectroscopy applied simultaneously allows for the identification of specific polymorphs formed at the end of the nanopipette. The technique is supported with a robust finite element method (FEM) model that allows for the extraction of time-dependent saturation levels, mixing characteristics and growth rates from the experimental current-time transients. Finally, the technique shows great promise as a tool for screening growth additives and inhibitors. In particular, it is demonstrated that the dicarboxylate dianion, maleate, has a significant impact on growth rates of calcium carbonate.

4.2 Introduction

Crystallization processes underpin a wide range of natural and technological phenomena from the formation of bones and shells,(302, 303) to the production of pharmaceuticals(304) to scale formation in pipes.(305) Studies of the formation of crystals and minerals from supersaturated solutions has a long history, driven by the desire to improve fundamental knowledge and advance practical applications.

One of the most studied and important minerals in natural and industrial systems is calcium carbonate, $CaCO_3$, is one of the most abundant and important minerals present on Earth.(68) It is key as a biomineral used by organisms in the formation of eggshells, seashells and snail shells as well as skeletal matter.(306, 307) It is also found as limestone deposits, which are used widely in the construction industry, is a significant component of coral reefs(308) and serves as a repository for carbon dioxide. There is also great interest in the formation of $CaCO_3$ as limescale(69) where solid $CaCO_3$ precipitates from dissolved calcium ions and carbon dioxide present in water sources. The prevention and removal of limescale is an important task as a build-up can lead to blockage and damage of water pipes on both a domestic and industrial scale. (70-72)

Despite the long history of study, major new aspects to crystallization continue to be revealed, such as the identification of new crystalline precursors and the proposition of new modes of growth including

oriented attachment of crystalline particles on lattice matched crystal faces,(309) growth via mesocrystals(169, 310) and the growth of $CaCO_3$ from nanoparticles.(311) There is still much ongoing study into the role of additives and also the role of both confinement and growth substrates on crystallization events.(193, 312, 313) Advancements to the study of crystals is forwarded by the development and application of novel techniques for studying crystal systems such as $CaCO_3$.

Techniques for measuring growth and dissolution events on the nanoscale include the use of scanning probe microscopy, most notably atomic force microscopy (AFM) to probe nanoscale changes in surface morphology during dissolution and growth.(314-316) AFM allows for the identification of heterogeneously active sites on a crystal surface with high precision and boasts resolution approaching the sub-nm level.(317) Information can also be obtained from *in-situ* electron microscopy with regard to the crystal surface and mode of transformation.(176, 318) In terms of probing the structure of the formed crystal and identifying the composition of mineral samples, Raman spectroscopy(164, 319-321) and x-ray diffraction(322) can also help to identify the crystal interactions and lattice structure. Microfluidic based techniques have also been used for both driving crystallization events as well as for studying the effects of additives on crystal growth and dissolution rates.(195)

New techniques for studying crystals have provided insights into the mechanism of $CaCO_3$ formation from solution and there is growing

evidence, including from computational and cryo transmission electron microscopy (TEM) techniques that before the formation of aragonite, vaterite or calcite, the three distinct polymorphs of $CaCO_3$, an amorphous cluster phase first forms which follow the formation of prenucleation nanoclusters.(140, 182, 323-325) TEM of samples that have been plunge-freeze vitrification during the nucleation phase, have revealed the presence of these prenucleation clusters, amorphous phases and the subsequent transformation to vaterite and finally to calcite.(323, 324)

In this work we consider the use of nanopipettes, already powerful tools for a host of analytical applications, (326-329) for the study $CaCO_3$ growth and dissolution, in a combinatorial approach together with *in situ* Raman spectroscopy and backed up with finite element method (FEM) simulations to provide a complete understanding. Herein, controlled growth and dissolution of $CaCO_3$ is achieved through filling a nanopipette with sodium bicarbonate solution and a quasi reference counter electrode (QRCE) and applying a bias between this QRCE and another QRCE placed in a bulk solution of calcium chloride. Through changing the magnitude and polarity of the bias applied, control over the local mixing of Ca^{2+} and CO_3^{2-} ions at the end of the nanopipette and growth or dissolution of $CaCO_3$ can be driven and monitored through observing changes in the ionic current through the end of the nanopipette. This builds upon recent work which considered the crystallization of zinc phosphate in a nanopipette where oscillations in the ionic current were attributed to periodic blocking and unblocking due to crystal growth and dissolution

resulting in changes in the pipette resistance.(117) Our work develops on this previous work, using a higher data acquisition rate for a more thorough analysis of growth and dissolution transients and the use of FEM modelling, allows for a more complete understanding of the mixing processes occurring at the end of the nanopipette and analysis of the experimental growth and dissolution rates observed. It also becomes possible to quantify the saturation levels at the end of the nanopipette where crystallization events occur in this regime. Furthermore the combination with Raman spectroscopy allows for the identification of the specific polymorph of $CaCO_3$, which forms in the end of the nanopipette and also hints at the formation of an amorphous phase before transformation to calcite.

There is much interest in the role of additives on the growth and dissolution of crystal systems and how they incorporate into crystal structures to affect the properties.(305, 330-335) A key strength of this approach is it allows for the inclusion of additives and thus provides a platform to screen and observe the effects of additives, which can serve to reduce or enhance the rates of crystal formation or dissolution. In this contribution, maleic acid, a known inhibitor for $CaCO_3$ growth,(336) is seen to result in an increase in an increase in the time taken for $CaCO_3$ to block the nanopipette, validating the technique as a tool for screening additives in a fast and robust manner. Applications of this could be in screening new chemicals for the prevention of scale build-ups in industrial systems. The combination of nanopipette voltammetric measurements, with FEM simulations and Raman spectroscopy provide a robust platform for the

study of the growth and dissolution of crystal systems on the nanoscale and could find great application in a wide range of systems.

4.3 MATERIALS AND METHODS

4.3.1 Solutions.

All solutions were made up using 18.2 MΩ cm water (Millipore Inc.). All chemicals used were purchased from Sigma Aldrich. The nanopipette contained 125 mM $NaHCO_3$ electrolyte solution for all experiments and the bath contained 25 mM $CaCl_2$ unless stated for individual experiments. For inhibitor studies maleic acid was added to the bath solution at concentrations ranging from 0.5 mM to 8 mM. For each experiment, all solutions were buffered to pH 9.2 using NaOH solution.

4.3.2 Nanopipettes.

Nanopipettes were fabricated using quartz glass capillaries with filaments (outer diameter 1.0 mm, inner diameter 0.5 mm, custom manufactured, Friedrich and Dimmock) using a laser puller (P-2000, Sutter Instruments; parameters of: Line 1: Heat 750, Fill 4, Vel 30, Del 150, Pull 80; Line 2: Heat 650, Fil 3, Vel 40, Del 135, Pull 150) to give a tip opening diameter of approximately 40-60 nm (determined accurately).(337) A typical tip is shown in Figure 34 at a range of magnifications.

4.3.3 Pipette Characterization

The pipettes used for these experiments were characterized using transmission electron microscopy (TEM), Optical microscopy and field emission - scanning electron microscopy (FE-SEM) as shown in Figure 34. These reveal tips with an open diameter of ~40-60 nm. It can be noted that the SEM revealed the filament present in the original glass capillary this is there to aid in the back filling of the pipette.

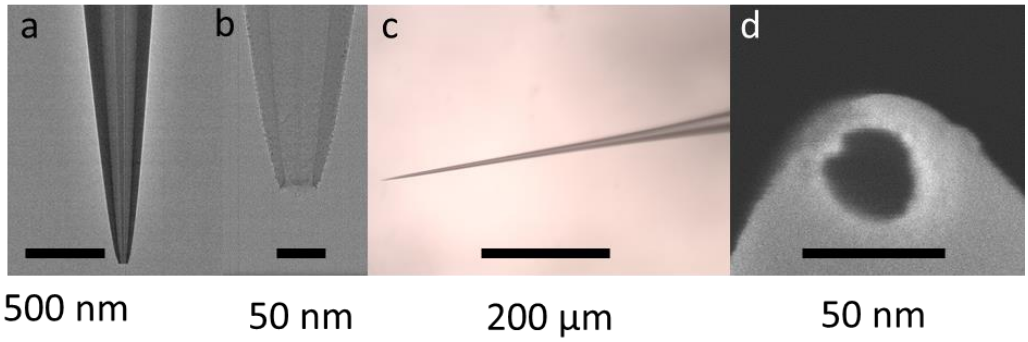

Figure 34 Micrographs of typical nanopipettes used in this investigation obtained using: (a) and (b) Transmission Electron Microscopy, (C) Optical microscopy and (d) Field Emission Scanning Electron Microscopy.

4.3.4 Instrumentation.

The electrometer and current-voltage converter used were home built, while the user control of voltage output and data collection was via custom made programs in LabVIEW (2013, National Instruments) through an FPGA card (7852R, National Instruments).

4.3.5 Bias Driven Crystallization Experiments.

Typical crystallization experiments involved filling the nanopipette with $NaHCO_3$ solution, to serve as both supporting electrolyte and a source of CO_3^{2-} ions, along with a chloridized silver wire, which serves as a QRCE. The nanopipette was immersed in a solution of CaCl2 containing a second Ag/AgCl QRCE. To drive crystallization, a negative bias was applied to the nanopipette QRCE relative to the bulk electrode. This typically resulted in a blockage to the nanopipette, and a resulting drop of the ionic current as observed in Figure 35. To unblock the nanopipette for subsequent experiments a positive bias (4 V) was instead applied to drive the constituent ions apart.

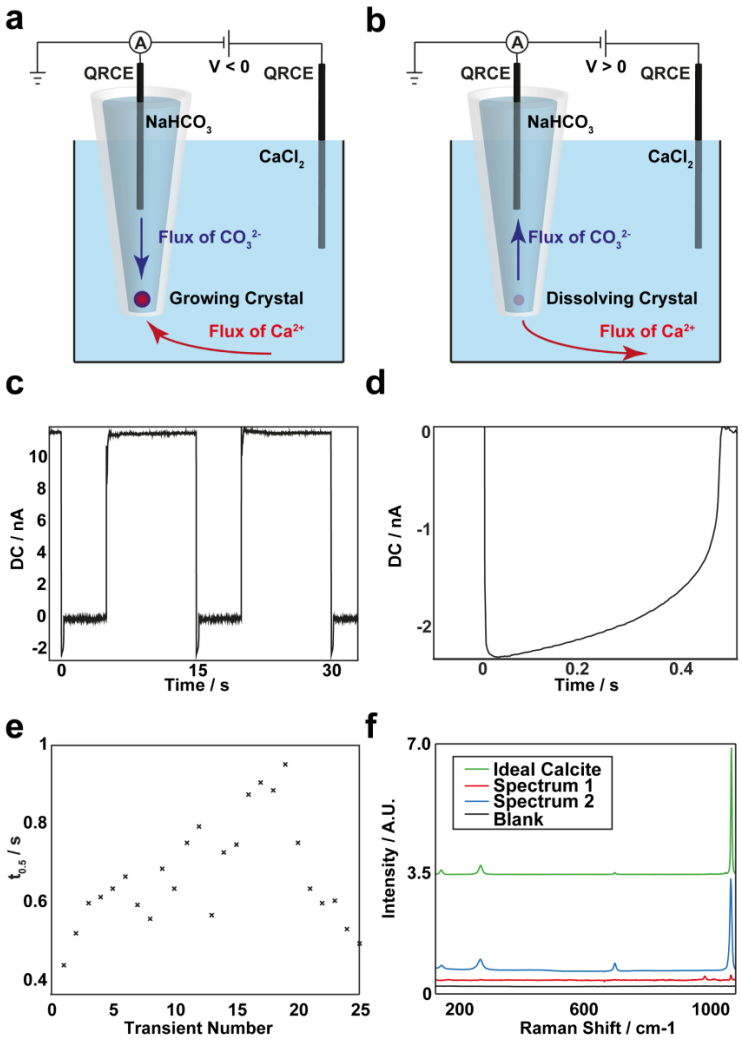

Figure 35 Schematic of the principles of precipitation in a nanopipette with growth occurring with negative tip bias, (a), and dissolution when the polarity is reversed, (b). c) Typical experimental blocking and unblocking events with blockages occurring with a tip bias of -0.25 V and unblocking at 4 V. d) Typical blocking transient with a blocking time $\tau_{0.5}$ of 400 ms. e) Variation of the extracted blocking time, $\tau_{0.5}$, over an experimental run of 25 events. f) Raman spectra performed at different times after a blocking event with the green line showing the simulated spectra of calcite for comparison, the black line shows the spectra of the nanopipette with solution before the polarity was switched to be negative and the blocking event occurs. The red spectrum was collected over 5 minutes from when the blocking occurred and suggests at the presence of amorphous calcium carbonate. The final spectra (blue) shows the presence of calcite.

The effect of driving bias was explored with biases ranging from 0 V to -1.2 V used. The effect of varying the concentration of Ca^{2+} in the bath was observed as shown in Figure 36 along with reversing the species in the pipette and bath as shown in Figure 37. The effect of additives was also explored by performing subsequent runs with the same nanopipette with increasing maleic acid concentrations from 0 mM to 8 mM present in the bath electrolyte. Each experimental run consisted of 25 blocking and unblocking events and all quoted blocking times, $\tau_{0.5}$, referred to herein, are measured from the time of the voltage switch to the time the current dropped below half its maximum value.

4.3.6 Variation of Ca^{2+} concentration in the bath solution

An experiment was carried out with 125mM $HNaCO_3$ in the pipette and varying $CaCl_2$ in the bath solution. This shows the strong correlation between bath concentration and $\tau_{0.5}$ time. Experimentally the remaining experiments used 25 mM in the bath as the time taken was measurable and allowed for observation of both longer and shorter times when adjusting other parameters.

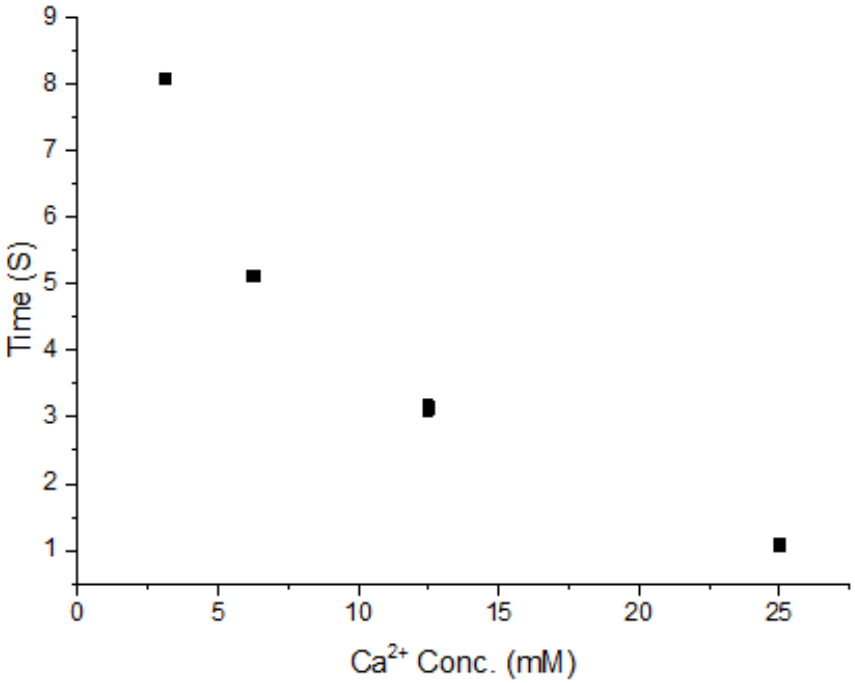

Figure 36 Effect of increasing Ca^{2+} concentration on the time taken for calcium carbonate to block the nanopipette.

4.3.7 Effect of inverting the tip and bath species whilst varying of CO_3^{2-} concentration in the bath solution

Experiments were performed with 125mM $CaCl_2$ in the pipette and varying $HNaCO_3$ concentrations in the bath solution. The effect of varying $HNaCO_3$ concentration on the blocking time is shown in Figure 37 and it can be seen that increasing concentrations of the carbonate ion in solution result in a faster blocking time. It should be noted that in these experiments the driving potentials applied were reversed in order to get the blocking to take place.

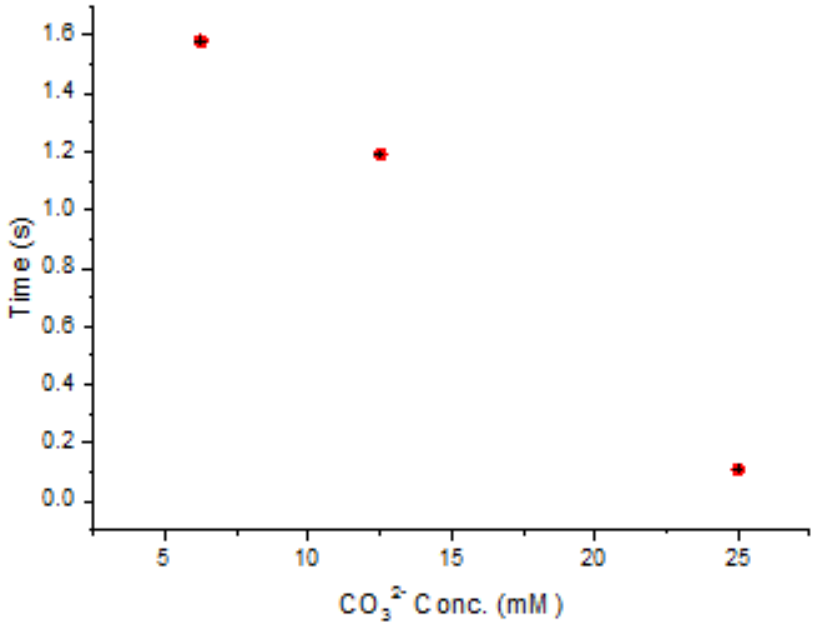

Figure 37 Effect of increasing CO_3^{2-} concentration on the time taken for calcium carbonate to block the nanopipette

4.3.8 FEM Simulations.

A 2D axisymmetric model of the nanopipette in bulk solution was constructed in Comsol Multiphysics (v. 5.2) with the Transport of Diluted Species and Electrostatics modules. A schematic of the simulation domain and boundary conditions is presented in Figure 40. The dimensions of the nanopipette were extracted from TEM images of nanopipettes and these were faithfully reproduced in the model so that the experimental geometry was mimicked precisely.(337) All simulations accounted for the speciation of calcium carbonate, with reaction constants and equations presented in Table 7.

Finite element method (FEM) simulations outlined above were all performed, incorporating the speciation of calcium carbonate in aqueous solutions with the equilibria parameters outlined in Table 7.(338)

Table 7 Equilibria parameters describing the speciation of calcium carbonate in aqueous solution

Eq	Reaction	pK
S1	$CO_2 + H_2O \rightleftharpoons H_2CO_3$	1.466
S2	$H_2CO_3 \rightleftharpoons H^+ + HCO_3^-$	6.351
S3	$HCO^- \rightleftharpoons H^+ + CO_3^{2-}$	10.33
S4	$CaHCO_3^+ \rightleftharpoons Ca^{2+} + HCO_3^-$	1.015
S5	$CaCO_{3(aq)} \rightleftharpoons Ca^{2+} + CO_3^{2-}$	3.2
S6	$H_2O \rightleftharpoons OH^- + H^+$	13.997

To study the mixing timescales of experiments, a steady state simulation was first run with a positive applied tip bias (2 V). A time dependent simulation was then run at negative tip bias (normally -0.25 V) to explore how the saturation level in the nanopipette changes with time. Simulations at positive tip bias were then performed to study the timescales over which the saturation levels reduced upon unblocking.

Steady state simulations were also performed with varying tip bias between 2 V and -1.2 V in order to explore how the saturation levels varied with driving force to facilitate the understanding of experiments. Finally growth rates for blocking events were studied by matching the proportion of blocked currents in experiments to FEM simulations of spheres of different radii present in the nanopipette domain.

4.3.9 Raman Spectroscopy.

In-situ micro-Raman spectra were collected from the final 10 µm of a nanopipette that had undergone a blocking event, using a Raman microscope (Renishaw, UK) fitted with a Charge Coupled Device (CCD) detector and a 514.5 nm Ar+ laser. A 20X lens was employed as shown in Figure 38.

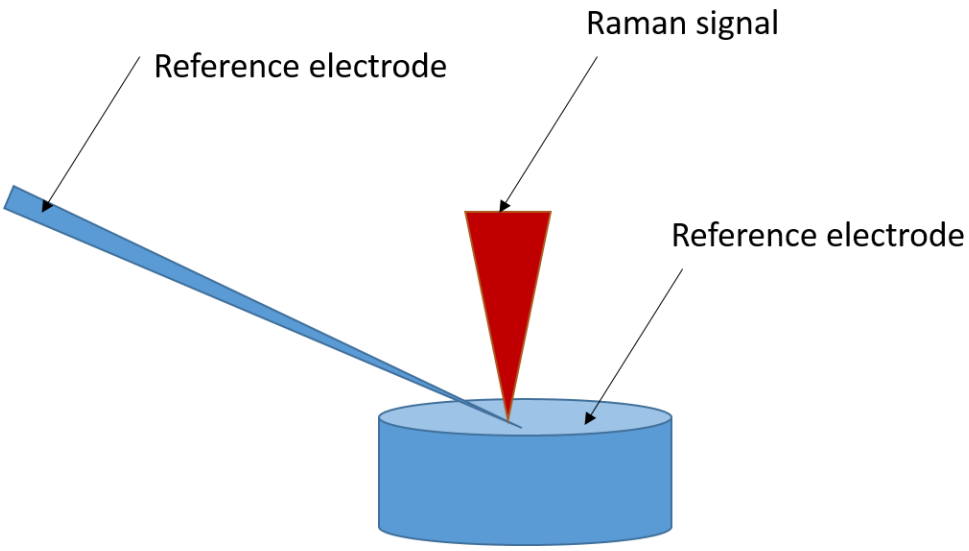

Figure 38 showing *In-situ* micro-Raman experimental set up

4.4 RESULTS AND DISCUSSION

4.4.1 Initial Experiments

The work initially looked at the possibility of using calcium phosphate as the crystal being studied. The nanopipette was filled with 125 mM Na_3PO_4 and placed in a bath of 25 mM $CaCl_2$ (solutions buffered above pH 9) whilst the bias was oscillated between 4 V and -0.25 V at the QRCE in the nanopipette with respect to one in bulk solution. Unfortunately, as can be seen in Figure 39 this system did not produce reproducible transients to study. It might be that the resulting crystal was particularly insoluble or did not grow in a way that consistently blocked the tip such as being needle shaped.

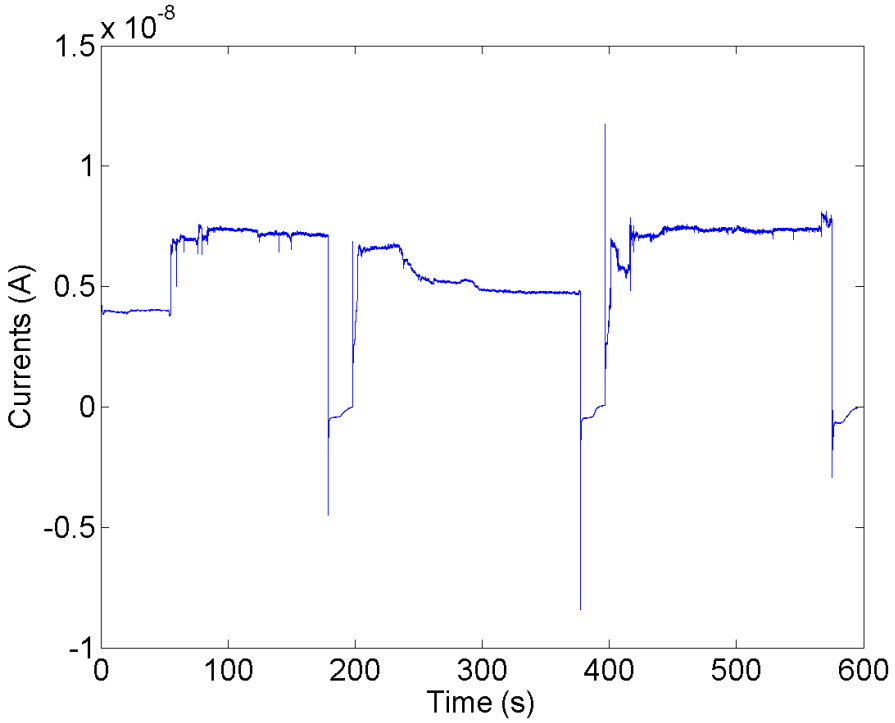

Figure 39 Showing the current vs. time transient when studying calcium phosphate crystals

4.4.2 Growth of Calcium Carbonate in a Nanopipette

The principles of using a single barreled nanopipette for the study of calcium carbonate nucleation and growth are depicted in Figure 35a and b. The nanopipette was filled with 125 mM $NaHCO_3$ and placed in a bath of 25 mM $CaCl_2$ (solutions buffered to pH 9.2) whilst applying a bias of 4 V to a QRCE in the nanopipette with respect to one in bulk solution. In this state a steady current is observed corresponding to an unblocked nanopipette. Upon switching the bias to -0.25 V, a decay is observed in the ionic current to nearly 0 A, as seen in Figure 35c and d. This drop in the ionic current is attributed to the formation of solid $CaCO_3$ at the end of the nanopipette.

When a negative tip bias is applied Ca^{2+} ions are driven to the nanopipette orifice and CO_3^{2-} ions are transported in the opposite direction. Where they meet at the end of the nanopipette, $CaCO_3$ forms and begins to grow, resulting in a blockage of the ionic current. Upon switching the polarity of the bias, the nanopipette can be seen to return to its open state, as seen in Figure 35c.

Through switching the applied bias, the nanopipette can become blocked and subsequently unblocked, making this a powerful technique for the study of growth kinetics of $CaCO_3$ in a controlled manor. It is important to note that the unblocked current remains constant, as depicted in Figure 35c. Figure 35d shows a typical blocking event in closer detail and it is seen the blockage is characterized by a slower initial drop off in the ionic current before a sharp rise at the end to around 0. The shape of this curve and the associated growth rates will be explored later with the aid of FEM simulations. Figure 35e depicts how, throughout a run of 25 experiments, the time taken for a 50 % blockage from the open state, $\tau_{0.5}$ varies. It can be seen that there is some variation, of around 400 ms, in the time taken but that there is no overall trend and an average blocking time of around 600 ms is observed. The variation in blockage times observed is most likely due to slight changes in the height at which the nucleation event occurs, which would affect the size to which a crystal particle could grow, as the dimensions of the nanopipette varies.

Raman spectroscopy, performed on the lowest 10 μm portion of a nanopipette, allowed for the analysis of what was forming at the end of the nanopipette during a typical experiment. Figure 35f shows typical Raman spectra obtained during and after a growth event. The black lines shows the signal obtained whilst the nanopipette is maintained at a positive bias with respect to the bulk solution. It can be seen that no signal is observed in this case.

Upon switching the bias, a second Raman spectrum with an acquisition time of 5 minutes was obtained and revealed the presence of two peaks, one at 1085 cm^{-1} and one at around 1000 cm^{-1}. The noticeable absence of peak at 711 cm^{-1} with the presence of one at 1085 cm^{-1} suggests the presence of amorphous calcium carbonate (ACC).(201) It is possible that the peak at 1000 cm^{-1} can be attributed to one of the metastable ACC polymorphs.(61) The blue spectrum, collected 30 minutes after the initial blockage, shows the presence of calcite near the end of the nanopipette due to the characteristic peaks V_1 at 1085, V_4 at 711 and lattice peaks at 282 and 155, agreeing with Raman spectra of known calcite sample,(60) as depicted by the green line of Figure 35f. These results indicate that the initial blockage of the nanopipette may result from ACC but that this transforms to the more stable calcite polymorph of $CaCO_3$, in accordance with known sequence of $CaCO_3$ crystallization and transformation events.(176) The time resolution of the Raman was insufficient to track this in more detail in order to provide more conclusive evidence.

4.4.3 Mixing of $CaCO_3$ in a Nanopipette

To aid understanding of the mixing and growth phenomena occurring in this system, FEM simulations were performed using conditions similar to that used experimentally, with 125 mM $NaHCO_3$ present in the nanopipette domain and 25 mM $CaCl_2$ representing the bath solution. Initially a steady state simulation was performed with a bias of 2 V applied to the upper boundary of the nanopipette domain. In experiments 4 V was applied in order to maximize the rate of unblocking and thus maximise experimental efficiency. Using the steady state solution with positive tip bias as the initial conditions, a time dependent simulation was then run, applying a tip bias of -0.25 V. Figure 40a-d depict the subsequent change in the saturation levels of $CaCO_3$ defined as:

$$K_s = \frac{\sqrt{[Ca]^{2+} X\ [{CO_3}^{2-}]}}{S} \qquad 1)$$

where $[Ca^{2+}]$ and $[CO_3^{2-}]$ are the concentrations of calcium and carbonate ions respectively and *S* is the solubility of calcium carbonate in water, known to be around 0.13 mM. At the start of the simulation, the highest value for K_S was calculated to be 0.05. After 10 ms, a region at the end of the nanopipette with a higher saturation of $CaCO_3$ begins to be distinguishable with values of up to 0.3. By 100 ms of mixing the saturation level increases above 1 (which would promote growth) and the solution is supersaturated. After 1000 ms of mixing, a supersaturation of around 5 is achieved. Figure 41a shows how the maximum value of K_S across the

simulation domain varies with time from these simulations, with the gradient decreasing with time. As typical blocking events lasted between 400 ms and 800 ms under these conditions, the supersaturation levels achieved could be in the range of 3 — 5. Steady state simulations under these conditions revealed a maximum K_S value of around 18 but this is unlikely to be achieved experimentally as the nanopipette becomes blocked, hindering mixing. It is interesting to note that whilst supersaturation levels change throughout the initial 1000 ms of mixing, the ionic current remains constant, after the first 0.1 ms, as shown in 3b when nothing is growing in the end of the nanopipette. Simulations also helped to estimate the position at which growth is most likely to occur. Figure 41c shows how the height of the maximum value of K_S above the nanopipette opening varies with time. At the time when the solution first becomes supersaturated, (~40 ms), this position is seen to be around 5 μm, making this the most likely position for initial nucleation and growth to occur. Up to around 300 ms, this position increases to as high as 12 μm before then decreasing back to around 6 μm. This is validated by the above-discussed Raman data, presented in Figure 35f, which was performed on the lowest 10 μm portion of the nanopipette and revealed the presence of formed calcite in this region.

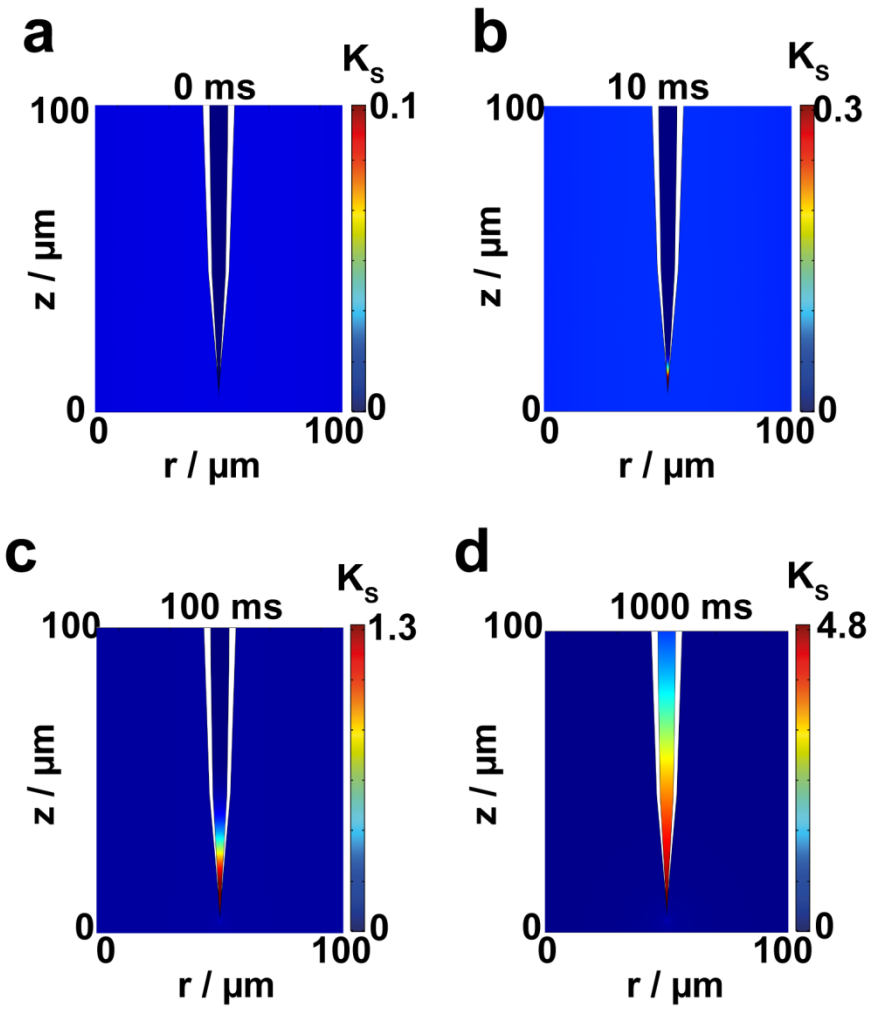

Figure 40 Simulated estimations for the saturation level of calcium carbonate in solution at times ranging from 0 ms to 1000 ms, (a-d). The saturation level starts to increase after around 10 ms and reaches a value of around 5 by 1000 ms. The most saturated region of the nanopipette can be seen to move up the length of the nanopipette initially

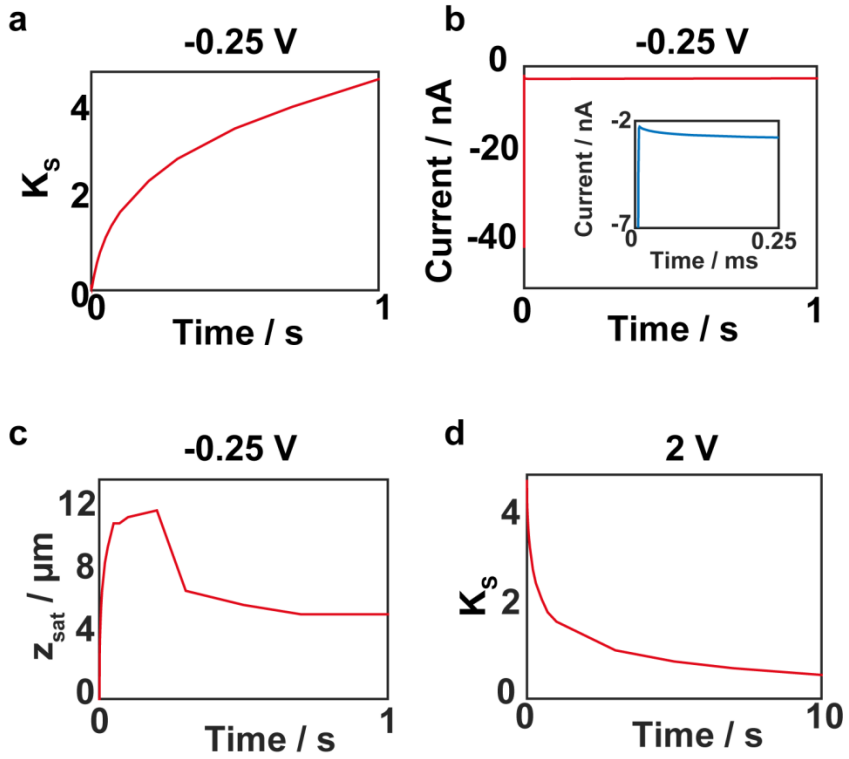

Figure 41 a) The rate of increase in maximum saturation across the whole simulation domain can be seen to increase over the whole first second with the rate of increase seen to decrease with time. b) The predicted ionic current can be seen to stabilize within 0.25 ms after switching the potential, inset shown with zoom in. c). The position of the maximum saturation from the nanopipette can be seen to vary with time initially increasing to 12 µm within 200 ms before decreasing to 6 µm. Upon switching the tip bias to be 2 V, after 600 ms of mixing at -0.25 V, the saturation can be seen to decrease to under 1 within 5 seconds, (d)

Simulations also helped justify the time required to allow sufficient unmixing of solutions for subsequent growth events. Figure 41d represents how the maximum value of saturation decreases when a bias of 2 V was applied after 600 ms of initial mixing. These results evidence a time of

around 4 s for the saturation level to drop back below 1. This would be expected to be quicker with a higher applied bias as used experimentally.

4.4.4 Quantifying Growth Rates in a Nanopipette

FEM simulations performed above predicted a position of around 5 μm above the nanopipette opening for the growth of calcium carbonate at the end of the nanopipette. Further FEM simulations help extract how the size of the growth product varies with time through modeling the precipitate as a spherical particle, which has been observed in other work. (61) These simulations are used to analyze the experimental growth transient, presented in Figure 42a. Simulations were performed with increasing particle size and the corresponding effect on the ionic current is observed in Figure 42b. It can be seen that the initial growth of the particle results in a small but measurable blockage of the ionic current. As the particle gets closer to the walls of the nanopipette, the resistance increases rapidly and there is a sharp drop off in the current that can pass the growing sphere. This helps to explain the shape of the experimental transient, which typically presents a slower initial decay of the current before a sharp decrease to 0.

Through combining the data of Figure 42a and b, a plot of expected particle radius with time can be obtained and is presented in Figure 42c. It can be seen that there is an initially high rate of growth with the radius changing at a rate approaching 12 nm/ms until the particle size reaches a

radius of around 300 nm and then the growth rate levels off. This is most likely due to a hindered migration of material to the region of the particle, closest to the nanopipette wall, which is where the most observable change in resistance would be seen. It is important to note that the times presented in Figure 42 are from the point of greatest current and do not include the time (~50 ms) after jumping the potential during which the saturation levels are likely to have reached 1 based on the above simulations. In order to determine whether the observed blocking times are reasonable, based on diffusion, an analytical calculation was performed based on the flux of material to an isolated growing spherical $CaCO_3$ particle. For a spherical particle growing due to a flux, j, the change in volume dV, with a change in time, dt, is defined by:

$$\frac{dV}{dt} = 4\pi r^2 \frac{dr}{dt} = j\frac{4\pi r^2}{\rho} \qquad 2)$$

where r is the radius of the particle and ρ is the molar density of $CaCO_3$.

For a flux controlled by diffusion:

$$j = \frac{D(C^* - C_{sat})}{r} \qquad 3)$$

where D is the diffusion coefficient of the species here assumed to be the Ca^{2+} CO_3^{2-} ion pair, C* is the bulk concentration, taken to be the

maximum saturation concentration taken from FEM simulations in the most saturated region of the nanopipette and C_{sat} is the concentration at the growing spherical particle, taken to be the solubility of calcium carbonate in water. Combining equations 2 and 3 and integrating gives an expression for a growing spherical particle with time as:

$$r^2 = \frac{4D(C^* - C_{sat})}{\rho} t \qquad 4)$$

Using a value for D of 8.525×10^{-6} cm^2/s, ρ as 0.0271 mol cm^{-3} and C_{sat} as

1.3×10^{-7} mol cm^{-3} together with values for C* obtained from Figure 41a, predicts a particle of radius 180 nm by a time of 600 ms. This is a similar magnitude to the growth rates extracted from the above analysis. Precise quantification is a difficult task owing to the fact that the precise position the crystal nuclei forming being unknown. Consequently the radius of the nanopipette at this location and hence the maximum size to which the particle could grow is not precise. This analysis does however show that the growth rates obtained above are reasonable based on the levels of saturation predicted from FEM simulations.

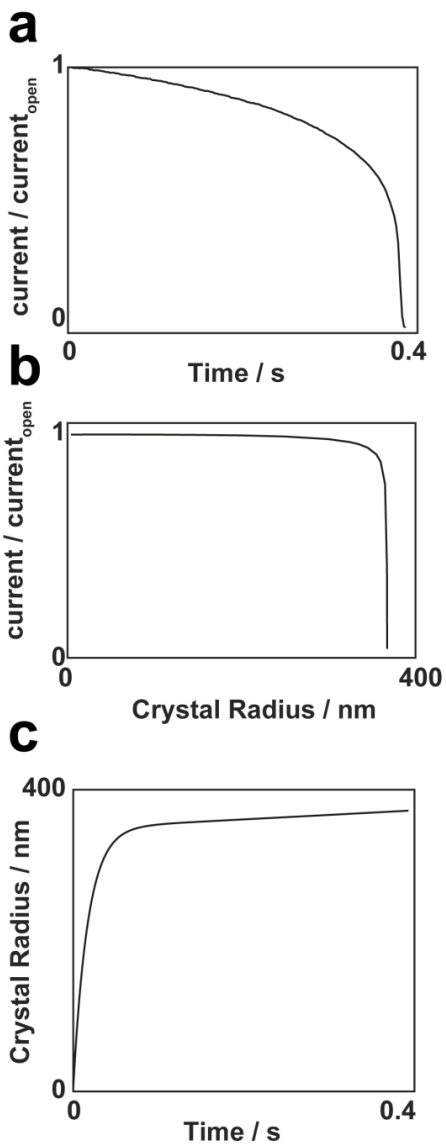

Figure 42 (a) Experimental blocking event showing the proportion of current decreasing with time to 0 in about 400 ms. (b) FEM simulation of a growing sphere in a nanopipette showing the drop off in current as the size of the sphere approaches the walls of the nanopipette. Most of the drop off is seen to occur when the sphere reaches a radius of around 320 nm. Through combining the simulation in (b) with the experimental data of (a), the radius of the growing particle in a blocking event, with time can be estimated, (c)

4.4.5 The Effect of Applied Bias on Blocking Rates

The formation of $CaCO_3$ explored above has all been driven through the application of a bias of -0.25 V to the nanopipette QRCE with respect to bulk. The effect of changing this applied bias is now explored. Experiments were performed with varying tip bias between -1.2 V and -0.001 V. Presented in Figure 43a, it is seen that increasing the magnitude of the applied bias from -0.001 V to -0.4 V, resulted in faster growth rates and hence smaller values for $\tau_{0.5}$. However further increases to the applied bias did not result in significantly different blockage times. There is a limit to the rate at which the calcium carbonate can be formed at the end of the nanopipette through simply increasing the bias magnitude.

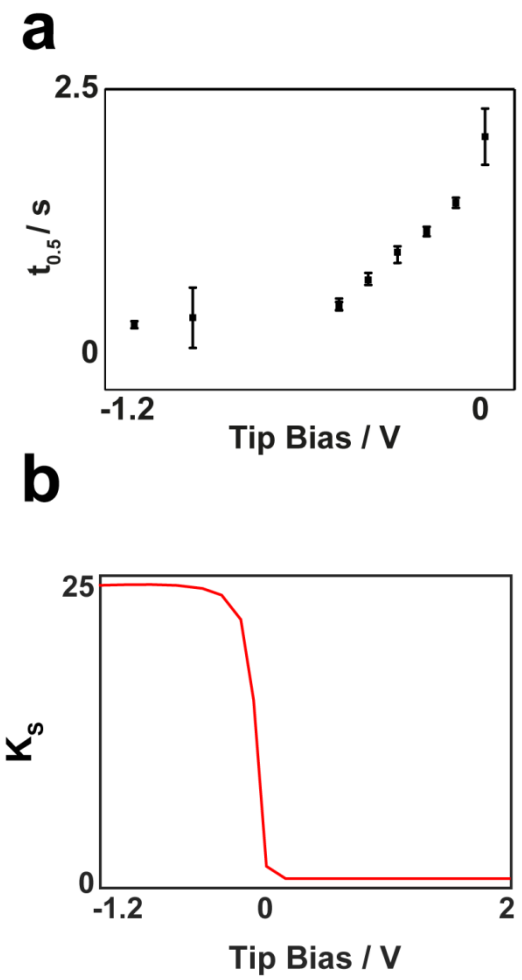

Figure 43 Experimental effect of varying tip bias on the blocking time shows a decrease in blocking time with higher magnitude bias, (a). As the bias is decreased below -600 mV, the effect of further decreases are less significant. b) Steady state FEM simulations reveal a similar trend with the maximum saturation level K_s initially increasing rapidly as the magnitude increases but levelling off at higher magnitude negative biases. At positive tip bias, saturation levels lower than one are predicted, validating the tip blocking and unblocking approach

Simulations performed at similar tip biases reveal that the steady state saturation level follows a similar trend to the experimental blocking times. Increasing the applied bias, initially results in higher saturation levels at the end of the nanopipette, as shown in Figure 43b. However increasing

the bias beyond -0.4 V results in negligible further increases in the saturation level, helping to explain why the blockage times do not decrease further. Note that when a positive tip bias is applied, the maximum values of K_S are below 1, validating why growth of $CaCO_3$ and blockages of the nanopipette are not observed under these conditions.

4.4.6 Inhibitor Studies Using a Nanopipette

Thus far, using a nanopipette has been seen to be robust for the study of growth kinetics for calcium carbonate in a confined geometry. It is now demonstrated whether the capabilities of the technique can be used for the study of additives. The formation of $CaCO_3$ scales is a great problem in industry and there is much work on the study of reducing $CaCO_3$ build-ups in pipes and other systems. Maleic acid, shown in Figure 44 is one such growth inhibitor that has been studied with application to preventing the formation of solid $CaCO_3$. The mechanism of maleic acid in the inhibition of $CaCO_3$ growth has been debated, with one hypothesis being that it acts as a chelating agent, binding to Ca^{2+} ions to prevent their involvement in $CaCO_3$ growth from solution. The alternative mode of action suggested is that the maleic acid instead acts on the surface of solid $CaCO_3$ inhibiting the addition of more material to the surface. Experimental runs of 25 blocking and unblocking events, as outlined above were now performed but with varying concentration of maleic acid present in the bath solution. After each run of experiments the concentration of maleic acid was increased to explore its effect.

Maleic acid was used as a test inhibitor to $CaCO_3$ growth in this investigation is structure is shown below in Figure 44.

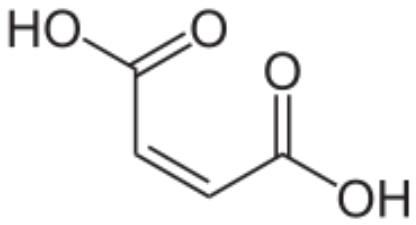

Figure 44 Molecular structure of maleic acid

Figure 45a shows typical transients overlaid with different concentrations of maleic acid present in the bath solution. It can be seen that increasing the concentration of maleic acid in solution results in significantly longer times required for a full blockage of the nanopipette to be observed with blocking times spanning nearly two orders of magnitude seen. It is important to note that these changes in blocking times are significantly larger than the variation observed in one experimental run, shown in Figure 35e. Figure 45b suggests an almost linear relationship between the maleic acid concentration present in the bath solution and the mean value of $\tau_{0.5}$ observed over the experimental run. This approach can also provide some information about the mechanism of action for maleic acid on calcium carbonate growth. Were maleic acid solely acting as a chelating agent, it would be expected that the effect of adding 8 mM maleic acid on the blocking time, would equate to 8 mM of Ca^{2+} ions leaving solution as each molecule would chelate one Ca^{2+} ion. An experimental run was also performed with 17 mM $CaCl_2$ present in the bath solution, using the same nanopipette as used for Figure 45a and b. This experiment yielded a value for $\tau_{0.5}$ of 2.1 ± 0.14 s. This should be compared to the value of $\tau_{0.5}$ observed with 8 mM maleic acid in the bath solution, which was seen to be around 16 seconds. Consequently it is hypothesized that the maleic acid does not act solely as a chelating agent, and has some surface effect as well, which inhibits the formation of solid $CaCO_3$ in the nanopipette.

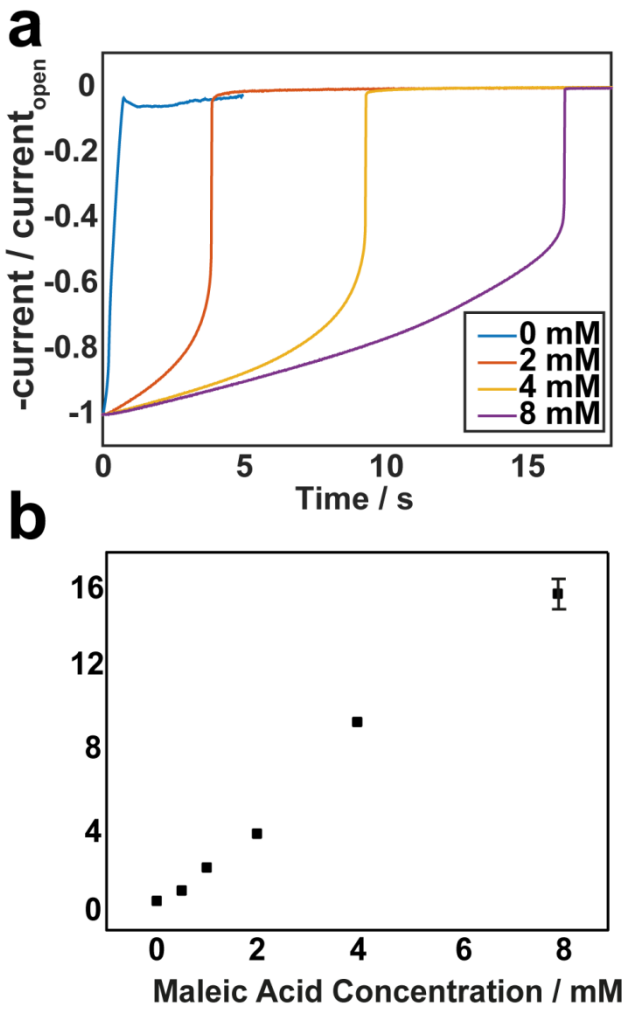

Figure 45 Increasing maleic acid concentrations are seen to result in an increased blocking time with typical transients shown in (a) and the trend shown in (b)

4.5 CONCLUSIONS

Building on previous work, it has been demonstrated herein that nanopipettes can provide a powerful and robust platform for the

consideration of crystal and particle growth events in a nanopipette in a controlled manner. Through tuning the bias applied between a QRCE in a nanopipette and outside in a bath solution, crystal formation can be driven at the end of the nanopipette, and can be used to extract growth kinetics. These crystals can be subsequently removed through reversing the polarity of the applied bias. The power of this technique is increased further through combination with other techniques, most notably Raman spectroscopy, which can provide diagnostic information about the formed product in the nanopipette and has helped postulate about the possible amorphous precursor to calcite formation.

This approach is backed up by a FEM model, which helps provide information about the mixing times needed for product formation as well as the supersaturation levels achievable in this experimental approach. Furthermore the effects of applied bias have been explored through combining experimental and simulation results and revealed the limits to which this technique can drive crystallization events.

Finally the power of this technique in the study of additives has been highlighted using the maleic acid inhibition on $CaCO_3$ growth as an example system. Through increasing the maleic acid concentration, the subsequent effects on crystal growth and blockage time have been observed and allowed us to elucidate some information about the mechanism behind the action of maleic acid in reducing $CaCO_3$ growth.

The technique presented herein is extremely versatile and, whilst has been applied in this work for the study of $CaCO_3$, could find great application for the study of other growth and dissolution systems as well as for additive studies and screening to determine efficacy in a controlled and precise regime.

5 Conclusions

Within this thesis a new approach for studying highly localised acid-induced dissolution has been described which can quantitatively show the kinetics involved in Chapter 2. The use of SECCM etching allowed multiple dissolution measurements on a single sample, without the effect of surrounding solution effects which allowed multiple surface treatments on the single sample to eliminate the effect of differing samples.

The resultant etch pits were characterised using AFM which allowed the calculation of removed enamel volume and pit diameter. This information was used in conjunction with a FEM model to calculate the intrinsic rate constant for proton induced dissolution of Ca^{2+} release which gave an average of 0.099 ± 0.008 cm s^{-1}.

It was also shown that this value decreased significantly with the use of surface treatments Zn^{2+} and F^- with F^- proving most successful. However the combination of both proved to be most effective decreasing to 0.025 ± 0.005 cm s^{-1}.

It was also shown, due to the ability to follow the dissolution in time, that the effect of the surface treatments is transitory and only extends to the initial 20 nm of enamel.

In chapter 3 this method was again utilised as part of a full investigation into the effect of calcium silicate as an additive to toothpaste

to both protect enamel but also promote its remineralisation and thus repair. Once again the intrinsic rate constant for Ca^{2+} release was calculated, this time as 0.092 ± 0.008 cm s^{-1} however this time the combination of both calcium silicate and fluoride proved to be most effective lowering the rate to 0.0063 ± 0.0002 cm s^{-1}.

The investigation also showed that in a phosphate free solution of calcium phosphate over 23 ppm of Ca^{2+} was released at pH 7 when measured using an ion selective electrode. This was continued by proving the formation of HAP when the product of a solution containing calcium silicate and phosphate was analysed using micro-Raman spectroscopy. This showed that at pH 7 HAP was produced.

It was also shown using FE-SEM that the calcium silicate particles preferred to adhere to rough acid etched samples and the effect of repair show by treating the SECCM etched samples with calcium silicate showing an average pit reduction of 77± 12%

The secondary aim of this thesis was dealt with in chapter 4 with the aim of investigating crystal growth and nucleation using a defined geometry technique which allowed for the study of the initial stages of nucleation and growth via nanoprecipitation within a nanopipette. This method utilised a strong ion current applied in alternating polarities to either drive substituent molecules together of apart. This allowed for the selective formation of calcium carbonate crystals at the nanopipette opening. The monitoring of the ion current through the nanopipette allowed for the early monitoring of

the early stages of nucleation. This process was rationalised through the use of FEM simulation to account for the system kinetics and calculate the rates of reaction. The polymorphs of the crystal formed was elucidated via the used of micro-Raman which gave an indication of the formation of ACC before undergoing transformation into calcite. The work also shows the effect of maleic acid as an inhibitor species which significantly slowed the rate of growth at trace levels. The obvious extension to this work would be to screen a series of candidate molecules for inhibition to compare them to the known maleic acid effect.

An interesting future development of this work may be to address further why as has been shown why some molecules supress early growth whilst others promote it and provide further evidence to the extent of this phenomenon. The method presented here is particularly suited to this issue as the method allows for accurate comparison of differences at the early stages of nucleation and growth.

There has been an emphasis throughout this thesis on systems which have strong industrial applications. The multi-microscopic analysis presented throughout has been critical in the outcomes of the work. In the two cases studied this has been the development of toothpastes and development of ways of inhibiting the growth of limescale. To this end a toothpaste product, Regenerate™, has been launched which incorporated calcium silicate as its active ingredient and we have presented a robust

method which can be used to test potential additives to prevent the growth of limescale.

6 Bibliography

1. Kurlansky M. Salt: Random House; 2011.

2. Lorenz R. Lehrbuch der allgemeinen chemie, von w. Ostwald. Ii. Band. 2. Teil: Verwandtschaftslehre. 1. Lieferung. (leipzig, 1896.) 5 mark. *Zeitschrift für anorganische Chemie*. 1897;**15**(1):239-.

3. Luquet G, Marin F. Biomineralisations in crustaceans: Storage strategies. *Comptes Rendus Palevol*. 2004;**3**(6–7):515-34.

4. Charola AE, Pühringer J, Steiger M. Gypsum: A review of its role in the deterioration of building materials. *Environmental Geology*. 2006;**52**(2):339-52.

5. Boyde A. Enamel. Teeth. Handbook of microscopic anatomy. 5 / 6: Springer Berlin Heidelberg; 1989. p. 309-473.

6. Smith BL, Schaffer TE, Viani M, Thompson JB, Frederick NA, Kindt J, et al. Molecular mechanistic origin of the toughness of natural adhesives, fibres and composites. *Nature*. 1999;**399**(6738):761-3.

7. Aizenberg J, Weaver JC, Thanawala MS, Sundar VC, Morse DE, Fratzl P. Skeleton of euplectella sp.: Structural hierarchy from the nanoscale to the macroscale. *Science*. 2005;**309**(5732):275-8.

8. Weiner S, Addadi L. Design strategies in mineralized biological materials. *Journal of Materials Chemistry*. 1997;**7**(5):689-702.

9. Addadi L, Raz S, Weiner S. Taking advantage of disorder: Amorphous calcium carbonate and its roles in biomineralization. *Advanced Materials*. 2003;**15**(12):959-70.

10. Robinson C, Shore RC, Brookes SJ, Strafford S, Wood SR, Kirkham J. The chemistry of enamel caries. *Critical Reviews in Oral Biology & Medicine*. 2000;**11**(4):481-95.

11. Francisconi LF, Honorio HM, Rios D, Magalhaes AC, Machado MAAM, Buzalaf MAR. Effect of erosive pH cycling on different restorative materials and on enamel restored with these materials. *Operative Dentistry*. 2008;**33**(2):203-8.

12. West NX, Hughes JA, Addy M. Erosion of dentine and enamel in vitro by dietary acids: The effect of temperature, acid character, concentration and exposure time. *Journal of Oral Rehabilitation*. 2000;**27**(10):875-80.

13. Shellis RP. Variations in growth of the enamel crown in human-teeth and a possible relationship between growth and enamel structure. *Archives of Oral Biology*. 1984;**29**(9):697-705.

14. Kay MI, Young RA, Posner AS. Crystal structure of hydroxyapatite. *Nature*. 1964;**204**:1050-2.

15. West NX, Joiner A. Enamel mineral loss. *Journal of Dentistry*.**42**:S2-S11.

16. Hillson SW. Diet and dental disease. *World Archaeology*. 1979;**11**(2):147-62.

17. Chadwick RG, Wilson NHF. Dental erosion: Quintessence; 2006.

18. Wiegand A, Koewinq L, Attin T. Impact of brushing force on abrasion of acid-softened and sound enamel. *Archives of Oral Biology*. 2007;**52**(11):1043-7.

19. Attin T, Meyer K, Hellwig E, Buchalla W, Lennon AM. Effect of mineral supplements to citric acid on enamel erosion. *Archives of Oral Biology*.**48**(11):753-9.

20. Higuchi WI, Gray JA, Hefferren JJ, Patel PR. Mechanisms of enamel dissolution in acid buffers. *Journal of Dental Research*. 1965;**44**:330-41.

21. Arends J, Tencate JM. Tooth enamel remineralization. *Journal of Crystal Growth*. 1981;**53**(1):135-47.

22. Global Industrial Analysts I. Toothpaste - a global strategic business report. http://www.strategyr.com/Toothpaste_Market_Report.asp: Global Industrial Analysts, Inc., 2010.

23. Ten Cate JM, Featherstone JDB. Mechanistic aspects of the interactions between fluoride and dental enamel. *Critical Reviews in Oral Biology and Medicine*. 1991;**2**(3):283-96.

24. McCann HG. The solubility of fluorapatite and its relationship to that of calcium fluoride. *Archives of Oral Biology*. 1968;**13**(8):987-1001.

25. Hughes JA, West NX, Parker DM, van den Braak MH, Addy M. Effects of pH and concentration of citric, malic and lactic acids on enamel, in vitro. *Journal of Dentistry*. 2000;**28**(2):147-52.

26. Hornby K, Evans M, Long M, Joiner A, Laucello M, Salvaderi A. Enamel benefits of a new hydroxyapatite containing fluoride toothpaste. Genève, SUISSE: FDI World Dental Federation; 2009. 7 p.

27. Li X, Wang J, Joiner A, Chang J. The remineralisation of enamel: A review of the literature. *Journal of Dentistry*.**42**:S12-S20.

28. Hornby K, Ricketts SR, Philpotts CJ, Joiner A, Schemehorn B, Willson R. Enhanced enamel benefits from a novel toothpaste and dual phase gel containing calcium silicate and sodium phosphate salts. *Journal of Dentistry*.**42**:S39-S45.

29. White W, Nancollas GH. Quantitative study of enamel dissolution under conditions of controlled hydrodynamics. *Journal of Dental Research*. 1977;**56**(5):524-30.

30. Chen WC, Nancollas GH. The kinetics of dissolution of tooth enamel - a constant composition study. *Journal of Dental Research*. 1986;**65**(5):663-8.

31. Muhler JC, Van Huysen G. Solubility of enamel protected by sodium fluoride and other compounds. *Journal of Dental Research*. 1947;**26**(2):119-27.

32. Gray JA. Kinetics of the dissolution of human dental enamel in acid. *Journal of Dental Research*. 1962;**41**:633-45.

33. Koulourides T, Reed JL, Jr. Effects of calcium, phosphate and fluoride ions on the rate of softening and dissolution of tooth enamel. *Archives of Oral Biology*. 1964;**9**:585-94.

34. Gray JA. Acid dissolution rate of sound and white-spot enamel treated with tin(ii) and fluoride compounds. *Journal of Dental Research*. 1965;**44**:493-501.

35. Gray JA. Kinetics of enamel dissolution during formation of incipient caries-like lesions. *Archives of Oral Biology*. 1966;**11**(4):397-422.

36. Higuchi WI, Mir NA, Patel PR, Becker JW, Hefferen JJ. Quantitation of enamel demineralization mechanisms. 3. A critical examination of the hydroxyapatite model. *Journal of Dental Research*. 1969;**48**(3):396-409.

37. Linge HG, Nancollas GH. Rotating-disk study of dissolution of dental enamel. *Calcified Tissue Research*. 1973;**12**(3):193-208.

38. Bishop DW, Eick JD, Nancollas GH, White WD. Dissolution kinetics of rotating-disks of sound and white spot enamel. *Journal of Dental Research*. 1974;**53**(FEB):198-.

39. White WD, Nancollas GH. A rotating-disk study of enamel dissolution in hedp solution under simulated white spot conditions. *Journal of Dental Research*. 1980;**59**(7):1180-6.

40. Barbour ME, Parker DM, Allen GC, Jandt KD. Human enamel dissolution in citric acid as a function of pH in the range 2.30 <= pH <= 6.30 - a nanoindentation study. *European Journal of Oral Sciences*. 2003;**111**(3):258-62.

41. Etienne M, Schulte A, Mann S, Jordan G, Dietzel LD, Schuhmann W. Constant-distance mode scanning potentiometry. 1. Visualization of calcium carbonate dissolution in aqueous solution. *Analytical Chemistry*. 2004;**76**(13):3682-8.

42. Finke M, Jandt KD, Parker DM. The early stages of native enamel dissolution studied with atomic force microscopy. *Journal of Colloid and Interface Science*. 2000;**232**(1):156-64.

43. Kato MT, Gutierrez Maria A, de Carvalho Sales-Peres SH, Buzalaf MAR. Effect of iron on the dissolution of bovine enamel powder in vitro by carbonated beverages. *Archives of Oral Biology*. 2007;**52**(7):614-7.

44. McGeouch C-A, Edwards MA, Mbogoro MM, Parkinson C, Unwin PR. Scanning electrochemical microscopy as a quantitative probe of acid-induced dissolution: Theory and application to dental enamel. *Analytical Chemistry*. 2010;**82**(22):9322-8.

45. Pyne A, Marks W, Picco LM, Dunton PG, Ulcinas A, Barbour ME, et al. High-speed atomic force microscopy of dental enamel dissolution in citric acid. *Archives of Histology and Cytology*. 2009;**72**(4-5):209-15.

46. Wang LJ, Tang RK, Bonstein T, Orme CA, Bush PJ, Nancollas GH. A new model for nanoscale enamel dissolution. *Journal of Physical Chemistry B*. 2005;**109**(2):999-1005.

47. Barbour ME, Parker DM, Allen GC, Jandt KD. Enamel dissolution in citric acid as a function of calcium and phosphate concentrations and degree of saturation with respect to hydroxyapatite. *European Journal of Oral Sciences*. 2003;**111**(5):428-33.

48. Laurance-Young P, Bozec L, Gracia L, Rees G, Lippert F, Lynch RJM, et al. A review of the structure of human and bovine dental hard tissues and their physicochemical behaviour in relation to erosive challenge and remineralisation. *Journal of Dentistry*. 2011;**39**(4):266-72.

49. Mellberg J. Hard-tissue substrates for evaluation of cariogenic and anti-cariogenic activity in situ. *Journal of Dental Research*. 1992;**71**.

50. Malinowski M, Duggal MS, Strafford SM, Toumba KJ. The effect on dental enamel of varying concentrations of fluoridated milk with a cariogenic challenge in situ. *Journal of Dentistry*.**40**(11):929-33.

51. Triller M. Fluoride as preventive agent of caries: Mechanisms, sources, risks. *Archives de Pédiatrie*. 1998;**5**(10):1149-52.

52. Parker AS, Patel AN, Al Botros R, Snowden ME, McKelvey K, Unwin PR, et al. Measurement of the efficacy of calcium silicate for the protection and repair of dental enamel. *Journal of Dentistry*.**42**:S21-S9.

53. Dong Z, Chang J, Deng Y, Joiner A. In vitro remineralization of acid-etched human enamel with Ca3SiO5. *Applied Surface Science*. 2010;**256**(8):2388-91.

54. Peld M, Tõnsuaadu K, Bender V. Sorption and desorption of Cd^{2+} and Zn^{2+} ions in apatite-aqueous systems. *Environmental Science & Technology*. 2004;**38**(21):5626-31.

55. Thuy TT, Nakagaki H, Kato K, Hung PA, Inukai J, Tsuboi S, et al. Effect of strontium in combination with fluoride on enamel remineralisation in vitro. *Archives of Oral Biology*. 2008;**53**(11):1017-22.

56. Dedhiya MG, Young F, Higuchi WI. Mechanism of hydroxyapatite dissolution. Synergistic effects of solution fluoride, strontium, and phosphate. *The Journal of Physical Chemistry*. 1974;**78**(13):1273-9.

57. Battistone GC, Feldman MH, Reba RC. The manganese content of human enamel and dentine. *Archives of Oral Biology*. 1967;**12**(10):1115-22.

58. Lynch RJM. Zinc in the mouth, its interactions with dental enamel and possible effects on caries; a review of the literature. *International Dental Journal*. 2011;**61**:46-54.

59. Söhnel O, Mullin JW. Precipitation of calcium carbonate. *Journal of Crystal Growth*. 1982;**60**(2):239-50.

60. Behrens G, Kuhn LT, Ubic R, Heuer AH. Raman spectra of vateritic calcium carbonate. *Spectroscopy Letters*. 1995;**28**(6):983-95.

61. Tlili MM, Amor MB, Gabrielli C, Joiret S, Maurin G, Rousseau P. Characterization of CaCO3 hydrates by micro-raman spectroscopy. *Journal of Raman Spectroscopy*. 2002;**33**(1):10-6.

62. Lowenstam HA, Weiner S. On biomineralization: Oxford University Press; 1989.

63. Davis ME. How life makes hard stuff. *Science*. 2004;**305**(5683):480.

64. Young JR, Didymus JM, Brown PR, Prins B, Mann S. Crystal assembly and phylogenetic evolution in heterococcoliths. *Nature*. 1992;**356**(6369):516-8.

65. Addadi L, Joester D, Nudelman F, Weiner S. Mollusk shell formation: A source of new concepts for understanding biomineralization processes. *Chemistry – A European Journal*. 2006;**12**(4):980-7.

66. Sommerdijk N, de With G. Biomimetic CaCO3 mineralization using designer molecules and interfaces. *Chemical Reviews*. 2008;**108**(11):4499-550.

67. Xyla AG, Mikroyannidis J, Koutsoukos PG. The inhibition of calcium carbonate precipitation in aqueous media by organophosphorus compounds. *Journal of Colloid and Interface Science*. 1992;**153**(2):537-51.

68. Heath CR, Leadbeater BCS, Callow ME. Effect of inhibitors on calcium carbonate deposition mediated by freshwater algae. *Journal of Applied Phycology*.**7**(4):367-80.

69. Matveenko BRSaLPRaIA. Mineralogical and geochemical characteristics of drinking water salt deposits. *IOP Conference Series: Earth and Environmental Science*. 2015;**27**(1):012042.

70. Hamza SM, Hamdona SK. Dissolution of calcium carbonate crystals: A constant-composition kinetic study. *Journal of the Chemical Society, Faraday Transactions*. 1992;**88**(18):2713-6.

71. Hart PW, Rudie AW. Mineral scale management, part i. Case studies. *Tappi Journal*. 2006;**5**(6):22.

72. Burroughs JE, Nowak JA. Composition and method for removing insoluble scale deposits from surfaces. Google Patents; 1976.

73. Coey JMD, Cass S. Magnetic water treatment. *Journal of Magnetism and Magnetic Materials*. 2000;**209**(1–3):71-4.

74. Wagterveld RM. Effect of ultrasound on calcium carbonate crystallization: TU Delft, Delft University of Technology; 2013.

75. Wang YW, Kim YY, Stephens CJ, Meldrum FC, Christenson HK. In situ study of the precipitation and crystallization of amorphous calcium carbonate (acc). *Crystal Growth & Design*. 2012;**12**(3):1212-7.

76. Wada N, Kanamura K, Umegaki T. Effects of carboxylic acids on the crystallization of calcium carbonate. *Journal of Colloid and Interface Science*. 2001;**233**(1):65-72.

77. Meldrum FC, Hyde ST. Morphological influence of magnesium and organic additives on the precipitation of calcite. *Journal of Crystal Growth*. 2001;**231**(4):544-58.

78. Butler MF, Glaser N, Weaver AC, Kirkland M, Heppenstall-Butler M. Calcium carbonate crystallization in the presence of biopolymers. *Crystal Growth & Design*. 2006;**6**(3):781-94.

79. Klepetsanis PG, Koutsoukos PG, Chitanu GC, Carpov A. The inhibition of calcium carbonate formation by copolymers containing maleic acid. In: Amjad Z, editor. Water soluble polymers: Solutions properties and applications. Boston, MA: Springer US; 2002. p. 117-29.

80. Mao Z, Huang J. Habit modification of calcium carbonate in the presence of malic acid. *Journal of Solid State Chemistry*. 2007;**180**(2):453-60.

81. Meldrum FC. Calcium carbonate in biomineralisation and biomimetic chemistry. *International Materials Reviews*. 2003;**48**(3):187-224.

82. Wehrmeister U, Jacob DE, Soldati AL, Loges N, Häger T, Hofmeister W. Amorphous, nanocrystalline and crystalline calcium carbonates in biological materials. *Journal of Raman Spectroscopy*. 2011;**42**(5):926-35.

83. Nehrke G, Poigner H, Wilhelms-Dick D, Brey T, Abele D. Coexistence of three calcium carbonate polymorphs in the shell of the antarctic clam laternula elliptica. *Geochemistry, Geophysics, Geosystems*. 2012;**13**(5):n/a-n/a.

84. Harroun SG, Bergman J, Jablonski E, Brosseau CL. Surface-enhanced raman spectroscopy analysis of house paint and wallpaper samples from an 18th century historic property. *Analyst*. 2011;**136**(17):3453-60.

85. Agarwal P, Berglund KA. In situ monitoring of calcium carbonate polymorphs during batch crystallization in the presence of polymeric additives using raman spectroscopy. *Crystal Growth & Design*. 2003;**3**(6):941-6.

86. Dekker C. Solid-state nanopores. *Nature Nanotechnology*. 2007;**2**(4):209-15.

87. Howorka S, Siwy Z. Nanopore analytics: Sensing of single molecules. *Chemical Society Reviews*. 2009;**38**(8):2360-84.

88. Siwy ZS, Davenport M. Making nanopores from nanotubes. *Nature Nanotechnology*. 2010;**5**(3):174-5.

89. Zhang B, Zhang Y, White HS. The nanopore electrode. *Analytical Chemistry*. 2004;**76**(21):6229-38.

90. Guo P, Martin CR, Zhao Y, Ge J, Zare RN. General method for producing organic nanoparticles using nanoporous membranes. *Nano Letters*. 2010;**10**(6):2202-6.

91. Han J, Fu J, Schoch RB. Molecular sieving using nanofilters: Past, present and future. *Lab on a Chip*. 2008;**8**(1):23-33.

92. Cheng LJ, Guo LJ. Nanofluidic diodes. *Chemical Society Reviews*. 2010;**39**(3):923-38.

93. Siwy ZS, Howorka S. Engineered voltage-responsive nanopores. *Chemical Society Reviews*. 2010;**39**(3):1115-32.

94. Harrell CC, Choi Y, Horne LP, Baker LA, Siwy ZS, Martin CR. Resistive-pulse DNA detection with a conical nanopore sensor. *Langmuir*. 2006;**22**(25):10837-43.

95. Kececi K, Sexton LT, Buyukserin F, Martin CR. Resistive-pulse detection of short dsdnas using a chemically functionalized conical nanopore sensor. *Nanomedicine (Lond)*. 2008;**3**(6):787-96.

96. Sexton LT, Horne LP, Martin CR. Developing synthetic conical nanopores for biosensing applications. *Molecular bioSystems*. 2007;**3**(10):667-85.

97. Ali M, Schiedt B, Neumann R, Ensinger W. Biosensing with functionalized single asymmetric polymer nanochannels. *Macromolecular Bioscience*. 2010;**10**(1):28-32.

98. Siwy Z, Behrends J, Fertig N, Fulinski A, Martin C, Neumann R, et al. Nanodevice for controlled charged particle flow and method for producing same. Google Patents; 2006.

99. Anne Spende and Nicolas Sobel and Manuela Lukas and Robert Zierold and Jesse CRaLGaISaJMMMaKNa. Tio 2 , sio 2 , and al 2 o 3 coated nanopores and nanotubes produced by ald in etched ion-track membranes for transport measurements. *Nanotechnology*. 2015;**26**(33):335301.

100. Eguizábal A, Sgroi M, Pullini D, Ferain E, Pina MP. Nanoporous pbi membranes by track etching for high temperature pems. *Journal of Membrane Science*. 2014;**454**:243-52.

101. Spohr R, Apel YP, Korchev Y, Siwy Z, Yoshida M. Method for etching at least one ion track to a pore in a membrane and electrolyte cell for preparing the membrane. Google Patents; 2006.

102. Wei C, Bard AJ, Feldberg SW. Current rectification at quartz nanopipet electrodes. *Analytical Chemistry*. 1997;**69**(22):4627-33.

103. Cervera J, Schiedt B, Neumann R, Mafé S, Ramírez P. Ionic conduction, rectification, and selectivity in single conical nanopores. *The Journal of Chemical Physics*. 2006;**124**(10):104706.

104. Innes L, Powell MR, Vlassiouk I, Martens C, Siwy ZS. Precipitation-induced voltage-dependent ion current fluctuations in conical nanopores. *The Journal of Physical Chemistry C*. 2010;**114**(18):8126-34.

105. Powell MR, Sullivan M, Vlassiouk I, Constantin D, Sudre O, Martens CC, et al. Nanoprecipitation-assisted ion current oscillations. *Nature Nano*. 2008;**3**(1):51-7.

106. Ying L. Applications of nanopipettes in bionanotechnology. *Biochemical Society Transactions*. 2009;**37**(Pt 4):702-6.

107. Klenerman D, Korchev Y. Potential biomedical applications of the scanned nanopipette. *Nanomedicine (Lond)*. 2006;**1**(1):107-14.

108. Actis P, Tokar S, Clausmeyer J, Babakinejad B, Mikhaleva S, Cornut R, et al. Electrochemical nanoprobes for single-cell analysis. *ACS Nano*. 2014;**8**(1):875-84.

109. McKelvey K, Perry D, Byers JC, Colburn AW, Unwin PR. Bias modulated scanning ion conductance microscopy. *Analytical Chemistry*. 2014;**86**(7):3639-46.

110. Perry D, Al Botros R, Momotenko D, Kinnear SL, Unwin PR. Simultaneous nanoscale surface charge and topographical mapping. *ACS Nano*. 2015;**9**(7):7266-76.

111. Sa N, Fu Y, Baker LA. Reversible cobalt ion binding to imidazole-modified nanopipettes. *Analytical Chemistry*. 2010;**82**(24):9963-6.

112. Fu Y, Tokuhisa H, Baker LA. Nanopore DNA sensors based on dendrimer-modified nanopipettes. *Chemical Communications (Cambridge, England)*. 2009(32):4877-9.

113. Umehara S, Karhanek M, Davis RW, Pourmand N. Label-free biosensing with functionalized nanopipette probes. *Proceedings of the National Academy of Sciences of the United States of America*. 2009;**106**(12):4611-6.

114. Actis P, Mak AC, Pourmand N. Functionalized nanopipettes: Toward label-free, single cell biosensors. *Bioanalytical reviews*. 2010;**1**(2-4):177-85.

115. Actis P, Jejelowo O, Pourmand N. Ultrasensitive mycotoxin detection by sting sensors. *Biosensors and Bioelectronics*. 2010;**26**(2):333-7.

116. Umehara S, Pourmand N, Webb CD, Davis RW, Yasuda K, Karhanek M. Current rectification with poly-l-lysine-coated quartz nanopipettes. *Nano Letters*. 2006;**6**(11):2486-92.

117. Vilozny B, Actis P, Seger RA, Pourmand N. Dynamic control of nanoprecipitation in a nanopipette. *ACS Nano*. 2011;**5**(4):3191-7.

118. Yusko EC, Billeh YN, Mayer M. Current oscillations generated by precipitate formation in the mixing zone between two solutions inside a nanopore. *Journal of physics Condensed Matter*. 2010;**22**(45):454127.

119. Oaki Y, Imai H. Experimental demonstration for the morphological evolution of crystals grown in gel media. *Crystal Growth & Design*. 2003;**3**(5):711-6.

120. Cai A, Xu X, Pan H, Tao J, Liu R, Tang R, et al. Direct synthesis of hollow vaterite nanospheres from amorphous calcium carbonate nanoparticles via phase transformation. *The Journal of Physical Chemistry C*. 2008;**112**(30):11324-30.

121. Weiner S, Addadi L. Acidic macromolecules of mineralized tissues: The controllers of crystal formation. *Trends in Biochemical Sciences*.**16**:252-6.

122. Naka K, Carney CK. Biomineralization i: Crystallization and self-organization process 2007.

123. Luquet G. Biomineralizations: Insights and prospects from crustaceans. *ZooKeys*. 2012(176):103-21.

124. Falini G, Albeck S, Weiner S, Addadi L. Control of aragonite or calcite polymorphism by mollusk shell macromolecules. *Science*. 1996;**271**(5245):67-9.

125. Teng HH, Dove PM, De Yoreo JJ. Kinetics of calcite growth: Surface processes and relationships to macroscopic rate laws. *Geochimica et Cosmochimica Acta*. 2000;**64**(2255-2266).

126. Berman A, Addadi L, Kvick Å, Leiserowitz L, Nelson M, Weiner S. Intercalation of sea urchin proteins in calcite: Study of a crystalline composite material. *Science*. 1990;**250**(4981):664-7.

127. Elhadj S, De Yoreo JJ, Hoyer JR, Dove PM. Role of molecular charge and hydrophilicity in regulating the kinetics of crystal growth. *Proceedings of the National Academy of Sciences*. 2006;**103**(51):19237-42.

128. Falini G, Fermani S, Tosi G, Dinelli E. Calcium carbonate morphology and structure in the presence of seawater ions and humic acids. *Crystal Growth & Design*. 2009;**9**(5):2065-72.

129. Rieger J, Thieme J, Schmidt C. Study of precipitation reactions by x-ray microscopy: CaCO3 precipitation and the effect of polycarboxylates. *Langmuir*. 2000;**16**(22):8300-5.

130. Walsh D, Kingston JL, Heywood BR, Mann S. Influence of monosaccharides and related molecules on the morphology of hydroxyapatite. *Journal of Crystal Growth*. 1993;**133**(1):1-12.

131. Wu W, Nancollas GH. Kinetics of nucleation and crystal growth of hydroxyapatite and fluorapatite on titanium oxide surfaces. *Colloids and Surfaces B: Biointerfaces*. 1997;**10**(2):87-94.

132. Koutsopoulos S. Kinetic study on the crystal growth of hydroxyapatite. *Langmuir*. 2001;**17**(26):8092-7.

133. Leite ER, Ribeiro C. Crystallization and growth of colloidal nanocrystals: Springer; 2011.

134. Frenkel J. A general theory of heterophase fluctuations and pretransition phenomena. *The Journal of Chemical Physics*. 1939;**7**(7):538-47.

135. Bennema P. Interpretation of the relation between the rate of crystal growth from solution and the relative supersaturation at low supersaturation. *Journal of Crystal Growth*. 1967;**1**(5):287-92.

136. Larson MA, Garside J. Solute clustering in supersaturated solutions. *Chemical Engineering Science*. 1986;**41**(5):1285-9.

137. Sangwal K. Additives and crystallization processes: From fundamentals to applications: Wiley; 2007.

138. Nývlt J. Kinetics of nucleation in solutions. *Journal of Crystal Growth*. 1968;**3–4**:377-83.

139. Boistelle R, Astier JP. Crystallization mechanisms in solution. *Journal of Crystal Growth*. 1988;**90**(1):14-30.

140. Gebauer D, Völkel A, Cölfen H. Stable prenucleation calcium carbonate clusters. *Science*. 2008;**322**(5909):1819-22.

141. Zhang TH, Liu XY. Nucleation: What happens at the initial stage? *Angewandte Chemie*. 2009;**121**(7):1334-8.

142. Clarkson JR, Price TJ, Adams CJ. Role of metastable phases in the spontaneous precipitation of calcium carbonate. *Journal of the Chemical Society, Faraday Transactions*. 1992;**88**(2):243-9.

143. Lacmann R, Herden A, Mayer C. Kinetics of nucleation and crystal growth. *Chemical Engineering & Technology*. 1999;**22**(4):279-89.

144. Bernstein J, Davey RJ, Henck J-O. Concomitant polymorphs. *Angewandte Chemie International Edition*. 1999;**38**(23):3440-61.

145. Cano H, Gabas N, Canselier JP. Experimental study on the ibuprofen crystal growth morphology in solution. *Journal of Crystal Growth*. 2001;**224**(3–4):335-41.

146. Ma CY, Wang XZ, Roberts KJ. Morphological population balance for modeling crystal growth in face directions. *AIChE Journal*. 2008;**54**(1):209-22.

147. Brittain HG. Polymorphism in pharmaceutical solids, second edition: CRC Press; 2009.

148. Mukuta T, Lee AY, Kawakami T, Myerson AS. Influence of impurities on the solution-mediated phase transformation of an active pharmaceutical ingredient. *Crystal Growth & Design*. 2005;**5**(4):1429-36.

149. Ostwald W. Studies upon the forming and changing solid bodies. 1897.

150. Kitamura M. Thermodynamic stability and transformation of pharmaceutical polymorphs. *Pure and Applied Chemistry*. 2005;**77**(3):581-91.

151. Kashchiev D. Thermodynamically consistent description of the work to form a nucleus of any size. *The Journal of Chemical Physics*. 2003;**118**(4):1837-51.

152. Burton W-K, Cabrera N, Frank F. The growth of crystals and the equilibrium structure of their surfaces. *Philosophical Transactions of the Royal Society of London A: Mathematical, Physical and Engineering Sciences*. 1951;**243**(866):299-358.

153. Giuffre AJ, Hamm LM, Han N, De Yoreo JJ, Dove PM. Polysaccharide chemistry regulates kinetics of calcite nucleation through competition of interfacial energies. *Proceedings of the National Academy of Sciences*. 2013;**110**(23):9261-6.

154. Petsev DN, Chen K, Gliko O, Vekilov PG. Diffusion-limited kinetics of the solution–solid phase transition of molecular substances. *Proceedings of the National Academy of Sciences*. 2003;**100**(3):792-6.

155. Habraken WJ, Tao J, Brylka LJ, Friedrich H, Bertinetti L, Schenk AS, et al. Ion-association complexes unite classical and non-classical

theories for the biomimetic nucleation of calcium phosphate. *Nature communications*. 2013;**4**:1507.

156. Cöelfen H, Antonietti M. Mesocrystals and nonclassical crystallization: Wiley; 2008.

157. Beniash E, Aizenberg J, Addadi L, Weiner S. Amorphous calcium carbonate transforms into calcite during sea urchin larval spicule growth. *Proceedings of the Royal Society B: Biological Sciences*. 1997;**264**(1380):461-5.

158. Gong YU, Killian CE, Olson IC, Appathurai NP, Amasino AL, Martin MC, et al. Phase transitions in biogenic amorphous calcium carbonate. *Proceedings of the National Academy of Sciences*. 2012;**109**(16):6088-93.

159. Politi Y, Arad T, Klein E, Weiner S, Addadi L. Sea urchin spine calcite forms via a transient amorphous calcium carbonate phase. *Science*. 2004;**306**(5699):1161-4.

160. Killian CE, Metzler RA, Gong Y, Olson IC, Aizenberg J, Politi Y, et al. Mechanism of calcite co-orientation in the sea urchin tooth. *Journal of the American Chemical Society*. 2009;**131**(51):18404-9.

161. Beniash E, Metzler RA, Lam RS, Gilbert P. Transient amorphous calcium phosphate in forming enamel. *Journal of Structural Biology*. 2009;**166**(2):133-43.

162. Mahamid J, Sharir A, Addadi L, Weiner S. Amorphous calcium phosphate is a major component of the forming fin bones of zebrafish: Indications for an amorphous precursor phase. *Proceedings of the National Academy of Sciences*. 2008;**105**(35):12748-53.

163. Dillaman R, Hequembourg S, Gay M. Early pattern of calcification in the dorsal carapace of the blue crab, callinectes sapidus. *Journal of Morphology*. 2005;**263**(3):356-74.

164. Weiss IM, Tuross N, Addadi L, Weiner S. Mollusc larval shell formation: Amorphous calcium carbonate is a precursor phase for aragonite. *Journal of Experimental Zoology*. 2002;**293**(5):478-91.

165. Fang P-A, Conway JF, Margolis HC, Simmer JP, Beniash E. Hierarchical self-assembly of amelogenin and the regulation of biomineralization at the nanoscale. *Proceedings of the National Academy of Sciences*. 2011;**108**(34):14097-102.

166. Penn RL, Banfield JF. Imperfect oriented attachment: Dislocation generation in defect-free nanocrystals. *Science*. 1998;**281**(5379):969-71.

167. Li D, Nielsen MH, Lee JRI, Frandsen C, Banfield JF, De Yoreo JJ. Direction-specific interactions control crystal growth by oriented attachment. *Science*. 2012;**336**(6084):1014-8.

168. Gower LB, Odom DJ. Deposition of calcium carbonate films by a polymer-induced liquid-precursor (pilp) process. *Journal of Crystal Growth*. 2000;**210**(4):719-34.

169. Li M, Schnablegger H, Mann S. Coupled synthesis and self-assembly of nanoparticles to give structures with controlled organization. *Nature*. 1999;**402**(6760):393-5.

170. Schwahn D, Ma Y, Cölfen H. Mesocrystal to single crystal transformation of d,l-alanine evidenced by small angle neutron scattering. *The Journal of Physical Chemistry C*. 2007;**111**(8):3224-7.

171. Cölfen H, Antonietti M. Mesocrystals: Inorganic superstructures made by highly parallel crystallization and controlled alignment. *Angewandte Chemie International Edition*. 2005;**44**(35):5576-91.

172. Song RQ, Cölfen H. Mesocrystals—ordered nanoparticle superstructures. *Advanced Materials*. 2010;**22**(12):1301-30.

173. Boneschanscher M, Evers W, Geuchies J, Altantzis T, Goris B, Rabouw F, et al. Long-range orientation and atomic attachment of nanocrystals in 2d honeycomb superlattices. *Science*. 2014;**344**(6190):1377-80.

174. Lupulescu AI, Rimer JD. In situ imaging of silicalite-1 surface growth reveals the mechanism of crystallization. *Science*. 2014;**344**(6185):729-32.

175. Chen Q, Cho H, Manthiram K, Yoshida M, Ye X, Alivisatos AP. Interaction potentials of anisotropic nanocrystals from the trajectory sampling of particle motion using in situ liquid phase transmission electron microscopy. *ACS Central Science*. 2015;**1**(1):33-9.

176. Nielsen MH, Aloni S, De Yoreo JJ. In situ TEM imaging of CaCO3 nucleation reveals coexistence of direct and indirect pathways. *Science*. 2014;**345**(6201):1158-62.

177. Gal A, Kahil K, Vidavsky N, DeVol RT, Gilbert PU, Fratzl P, et al. Particle accretion mechanism underlies biological crystal growth from an amorphous precursor phase. *Advanced Functional Materials*. 2014;**24**(34):5420-6.

178. Burrows ND, Hale CR, Penn RL. Effect of pH on the kinetics of crystal growth by oriented aggregation. *Crystal Growth & Design*. 2013;**13**(8):3396-403.

179. Beniash E, Aizenberg J, Addadi L, Weiner S. Amorphous calcium carbonate transforms into calcite during sea urchin larval spicule growth. *Proceedings of the Royal Society of London B: Biological Sciences*. 1997;**264**(1380):461-5.

180. Pichon BP, Bomans PHH, Frederik PM, Sommerdijk N. A quasi-time-resolved cryotem study of the nucleation of CaCO3 under langmuir monolayers. *Journal of the American Chemical Society*. 2008;**130**(12):4034-40.

181. Lee JRI, Han TYJ, Willey TM, Wang D, Meulenberg RW, Nilsson J, et al. Structural development of mercaptophenol self-assembled monolayers and the overlying mineral phase during templated CaCO3 crystallization from a transient amorphous film. *Journal of the American Chemical Society*. 2007;**129**(34):10370-81.

182. Demichelis R, Raiteri P, Gale JD, Quigley D, Gebauer D. Stable prenucleation mineral clusters are liquid-like ionic polymers. *Nature Communications*. 2011;**2**:590.

183. Kim Y-Y, Schenk AS, Ihli J, Kulak AN, Hetherington NBJ, Tang CC, et al. A critical analysis of calcium carbonate mesocrystals. *Nature Communications*. 2014;**5**.

184. Ihli J, Kulak AN, Meldrum FC. Freeze-drying yields stable and pure amorphous calcium carbonate (acc). *Chemical Communications*. 2013;**49**(30):3134-6.

185. Mann S, Heywood BR, Rajam S, Birchall JD. Controlled crystallization of caco3 under stearic-acid monolayers. *Nature*. 1988;**334**(6184):692-5.

186. Nickell S, Kofler C, Leis AP, Baumeister W. A visual approach to proteomics. *Nature Reviews Molecular Cell Biology*. 2006;**7**(3):225-30.

187. Pouget EM, Bomans PHH, Goos JACM, Frederik PM, de With G, Sommerdijk NAJM. The initial stages of template-controlled CaCO3 formation revealed by cryo-TEM. *Science*. 2009;**323**(5920):1455-8.

188. Michel FM, MacDonald J, Feng J, Phillips BL, Ehm L, Tarabrella C, et al. Structural characteristics of synthetic amorphous calcium carbonate. *Chemistry of Materials*. 2008;**20**(14):4720-8.

189. Quigley D, Rodger PM. Free energy and structure of calcium carbonate nanoparticles during early stages of crystallization. *Journal of Chemical Physics*. 2008;**128**(22):221101.

190. Wang Y-W, Christenson HK, Meldrum FC. Confinement increases the lifetimes of hydroxyapatite precursors. *Chemistry of Materials*. 2014;**26**(20):5830-8.

191. Schenk AS, Albarracin EJ, Kim Y-Y, Ihli J, Meldrum FC. Confinement stabilises single crystal vaterite rods. *Chemical Communications*. 2014;**50**(36):4729-32.

192. Verch A, Côté AS, Darkins R, Kim Y-Y, van de Locht R, Meldrum FC, et al. Correlation between anisotropy and lattice distortions in single crystal calcite nanowires grown in confinement. *Small*. 2014;**10**(13):2697-702.

193. Stephens CJ, Ladden SF, Meldrum FC, Christenson HK. Amorphous calcium carbonate is stabilized in confinement. *Advanced Functional Materials*. 2010;**20**(13):2108-15.

194. De Yoreo JJ, Gilbert PUPA, Sommerdijk NAJM, Penn RL, Whitelam S, Joester D, et al. Crystallization by particle attachment in synthetic, biogenic, and geologic environments. *Science*. 2015;**349**(6247).

195. Yin H, Ji B, Dobson PS, Mosbahi K, Glidle A, Gadegaard N, et al. Screening of biomineralization using microfluidics. *Analytical Chemistry*. 2008;**81**(1):473-8.

196. Glater J, York J, Campbell K, Spiegler K, Laird A. Principles of desalination. *Part B KS Spiegler, ADK Laird (Eds)(2nd ed) Academic Press, New York*. 1980:627.

197. MacAdam J, Parsons SA. Calcium carbonate scale formation and control. *Re/Views in Environmental Science & Bio/Technology*. 2004;**3**(2):159-69.

198. Meyer HJ. The influence of impurities on the growth rate of calcite. *Journal of Crystal Growth*. 1984;**66**(3):639-46.

199. Roques H. Chemical water treatment: VCH Publishers; 1996.

200. Müller-Steinhagen H, Engineers IoC. Heat exchanger fouling: Mitigation and cleaning technologies: Publico Publications; 2000.

201. Ihli J, Kim Y-Y, Noel EH, Meldrum FC. The effect of additives on amorphous calcium carbonate (acc): Janus behavior in solution and the solid state. *Advanced Functional Materials*. 2013;**23**(12):1575-85.

202. Bard AJ, Faulkner LR. Electrochemical methods: Fundamentals and applications: Wiley; 2000.

203. Atkins P, De Paula J. Atkins' physical chemistry. OUP Oxford; 2014.

204. Mertz J. Introduction to optical microscopy. Roberts and Company Publishers; 2010.

205. Chartier G. introduction to optics Pearson; 2005

206. Binning G, Rohrer H, Gerber C, Weibel E. Surface studies by scanning tunneling microscopy. *Physical Review Letters*. 1982;**49**(1):57-61.

207. Binnig GK. Atomic-force microscopy. *Physica Scripta*. 1987;**T19A**:53-4.

208. Bard AJ, Fan FRF, Kwak J, Lev O. Scanning electrochemical microscopy - introduction and principles. *Analytical Chemistry*. 1989;**61**(2):132-8.

209. Hansma PK, Drake B, Marti O, Gould SAC, Prater CB. The scanning ion-conductance microscope. *Science*. 1989;**243**(4891):641-3.

210. Ebejer N, Schnippering M, Colburn AW, Edwards MA, Unwin PR. Localized high resolution electrochemistry and multifunctional imaging: Scanning electrochemical cell microscopy. *Analytical Chemistry*. 2010;**82**(22):9141-5.

211. Buchler M, Kelley SC, Smyrl WH. Scanning electrochemical microscopy with shear force feedback - investigation of the lateral resolution of different experimental configurations. *Electrochemical and Solid State Letters*. 2000;**3**(1):35-8.

212. McKelvey K, Edwards MA, Unwin PR. Intermittent contact-scanning electrochemical microscopy (ic-secm): A new approach for tip positioning and simultaneous imaging of interfacial topography and activity. *Analytical Chemistry*. 2010;**82**(15):6334-7.

213. Meyer E. Atomic force microscopy. *Progress in Surface Science*. 1992;**41**(1):3-49.

214. Kuznetsov YG, Malkin AJ, McPherson A. Afm studies of the nucleation and growth mechanisms of macromolecular crystals. *Journal of Crystal Growth*. 1999;**196**(2–4):489-502.

215. McPherson A, Malkin A, Kuznetsov YG, Plomp M. Atomic force microscopy applications in macromolecular crystallography. *Acta Crystallographica Section D*. 2001;**57**:1053-60.

216. Binnig G, Quate CF, Gerber C. Atomic force microscope. *Physical Review Letters*. 1986;**56**(9):930-3.

217. Hembacher S, Giessibl FJ, Mannhart J, Quate CF. Revealing the hidden atom in graphite by low-temperature atomic force microscopy. *Proceedings of the National Academy of Sciences*. 2003;**100**(22):12539-42.

218. Akihiro Torii and Minoru Sasaki and Kazuhiro Hane and Shigeru O. A method for determining the spring constant of cantilevers for atomic force microscopy. *Measurement Science and Technology*. 1996;**7**(2):179.

219. Albrecht TR, Grutter P, Horne D, Rugar D. Frequency-modulation detection using high-q cantilevers for enhanced force microscope sensitivity. *Journal of Applied Physics*. 1991;**69**(2):668-73.

220. Steven RAaHAS. A review of power harvesting using piezoelectric materials (2003–2006). *Smart Materials and Structures*. 2007;**16**(3):R1.

221. Polla DL, Francis LF. Processing and characterization of piezoelectric materials and integration into microelectromechanical systems. *Annual Review of Materials Science*. 1998;**28**(1):563-97.

222. Rushbrooke GS, Wood PJ. On the curie points and high temperature susceptibilities of heisenberg model ferromagnetics. *Molecular Physics*. 1958;**1**(3):257-83.

223. Sodano HA, Inman DJ, Park G. A review of power harvesting from vibration using piezoelectric materials. *Shock and Vibration Digest*. 2004;**36**(3):197-206.

224. Binnig G, Smith DPE. Single-tube three-dimensional scanner for scanning tunneling microscopy. *Review of Scientific Instruments*. 1986;**57**(8):1688-9.

225. Chen C-C, Zhou Y, Baker LA. Scanning ion conductance microscopy. *Annual Review of Analytical Chemistry*. 2012;**5**(1):207-28.

226. Morris CA, Friedman AK, Baker LA. Applications of nanopipettes in the analytical sciences. *Analyst*. 2010;**135**(9):2190-202.

227. Novak P, Li C, Shevchuk AI, Stepanyan R, Caldwell M, Hughes S, et al. Nanoscale live-cell imaging using hopping probe ion conductance microscopy. *Nat Meth*. 2009;**6**(4):279-81.

228. Takahashi Y, Murakami Y, Nagamine K, Shiku H, Aoyagi S, Yasukawa T, et al. Topographic imaging of convoluted surface of live cells by scanning ion conductance microscopy in a standing approach mode. *Physical Chemistry Chemical Physics*. 2010;**12**(34):10012-7.

229. Shevchuk AI, Gorelik J, Harding SE, Lab MJ, Klenerman D, Korchev YE. Simultaneous measurement of Ca2+ and cellular dynamics:

Combined scanning ion conductance and optical microscopy to study contracting cardiac myocytes. *Biophysical Journal*. 2001;**81**(3):1759-64.

230. Oesterle A. What is “filamented” glass & who needs it? Available from: http://www.sutter.com/MICROPIPETTE/glass.html.

231. Kwak J, Bard AJ. Scanning electrochemical microscopy. Apparatus and two-dimensional scans of conductive and insulating substrates. *Analytical Chemistry*. 1989;**61**(17):1794-9.

232. Macpherson JV, Unwin PR. Combined scanning electrochemical−atomic force microscopy. *Analytical Chemistry*. 2000;**72**(2):276-85.

233. Unwin P, Ebejer N, inventors; Univ Warwick; Unwin P; Ebejer N, assignee. Scanning electrochemical cell microscopy (seccm) apparatus for direct amperometric imaging, adjusts position of pipet so as to control separation between tip of pipet and surface of interest patent WO2012020264-A1; US2013140191-A1; EP2603801-A1.

234. Ebejer N, Guell AG, Lai SCS, McKelvey K, Snowden ME, Unwin PR. Scanning electrochemical cell microscopy: A versatile technique for nanoscale electrochemistry and functional imaging. *Annual Review of Analytical Chemistry (Palo Alto, Calif)*. 2013;**6**:329-51.

235. Güell AG, Ebejer N, Snowden ME, McKelvey K, Macpherson JV, Unwin PR. Quantitative nanoscale visualization of heterogeneous electron transfer rates in 2d carbon nanotube networks. *Proceedings of the National Academy of Sciences*. 2012.

236. McMullan D. Scanning electron microscopy 1928–1965. *Scanning*. 1995;**17**(3):175-85.

237. Gardiner DJ, Bowley HJ, Graves PR, Gerrard DL, Louden JD, Turrell G. Practical raman spectroscopy: Springer Berlin Heidelberg; 2012.

238. Cuscó R, Guitián F, Aza Sd, Artús L. Differentiation between hydroxyapatite and β-tricalcium phosphate by means of μ-raman spectroscopy. *Journal of the European Ceramic Society*. 1998;**18**(9):1301-5.

239. de Aza PN, Santos C, Pazo A, de Aza S, Cuscó R, Artús L. Vibrational properties of calcium phosphate compounds. 1. Raman spectrum of β-tricalcium phosphate. *Chemistry of Materials*. 1997;**9**(4):912-5.

240. Sherif E-SM, Erasmus RM, Comins JD. Corrosion of copper in aerated synthetic sea water solutions and its inhibition by 3-amino-1,2,4-triazole. *Journal of Colloid and Interface Science*. 2007;**309**(2):470-7.

241. Snowden ME, Gueell AG, Lai SCS, McKelvey K, Ebejer N, O'Connell MA, et al. Scanning electrochemical cell microscopy: Theory and experiment for quantitative high resolution spatially-resolved voltammetry and simultaneous ion-conductance measurements. *Analytical Chemistry*. 2012;**84**(5):2483-91.

242. Babuška I, Banerjee U, Osborn JE. Generalized finite element methods—main ideas, results and perspective. *International Journal of Computational Methods*. 2004;**1**(01):67-103.

243. Dokoumetzidis A, Macheras P. A century of dissolution research: From Noyes and Whitney to the biopharmaceutics classification system. *International Journal of Pharmaceutics*. 2006;**321**(1-2):1-11.

244. Orr JC, Fabry VJ, Aumont O, Bopp L, Doney SC, Feely RA, et al. Anthropogenic ocean acidification over the twenty-first century and its impact on calcifying organisms. *Nature*. 2005;**437**(7059):681-6.

245. Bjorklund RB, Arwin H. Ellipsometric study of anionic surfactant adsorption on apatite and calcite ore surfaces. *Langmuir*. 1992;**8**(7):1709-14.

246. Smith DC, Simon M, Alldredge AL, Azam F. Intense hydrolytic enzyme-activity on marine aggregates and implications for rapid particle dissolution. *Nature*. 1992;**359**(6391):139-42.

247. Azarmi S, Roa W, Lobenberg R. Current perspectives in dissolution testing of conventional and novel dosage forms. *International Journal of Pharmaceutics*. 2007;**328**(1):12-21.

248. Demadis KD, Lykoudis P, Raptis RG, Mezei G. Phosphonopolycarboxylates as chemical additives for calcite scale dissolution and metallic corrosion inhibition based on a calcium-phosphonotricarboxylate organic-inorganic hybrid. *Crystal Growth and Design*. 2006;**6**(5):1064-7.

249. Desarnaud J, Grauby O, Bromblet P, Vallet J-M, Baronnett A. Growth and dissolution of crystal under load: New experimental results on kcl. *Crystal Growth and Design*. 2013;**13**(3):1067-74.

250. Kameda J, Sugimori H, Murakami T. Modification to the crystal structure of chlorite during early stages of its dissolution. *Physics and Chemistry of Minerals*. 2009;**36**(9):537-44.

251. Mauldin TC, Kessler MR. Enhanced bulk catalyst dissolution for self-healing materials. *Journal of Materials Chemistry*. 2010;**20**(20):4198-206.

252. Peruffo M, Mbogoro MM, Edwards MA, Unwin PR. Holistic approach to dissolution kinetics: Linking direction-specific microscopic fluxes, local mass transport effects and global macroscopic rates from gypsum etch pit analysis. *Physical Chemistry Chemical Physics*. 2013;**15**(6):1956-65.

253. Yu H-D, Yang D, Wang D, Han M-Y. Top-down fabrication of calcite nanoshoot arrays by crystal dissolution. *Advanced Materials*. 2010;**22**(29):3181-4.

254. Unwin PR, Macpherson JV. New strategies for probing crystal dissolution kinetics at the microscopic level. *Chemical Society Reviews*. 1995;**24**(2):109-19.

255. R. Unwin P. The marlow medal lecture: Dynamic electrochemistry as a quantitative probe of interfacial physicochemical processes. *Journal of the Chemical Society, Faraday Transactions*. 1998;**94**(21):3183-95.

256. Phillips RW, Van Huysen G. The chemistry of tooth tissues. *Journal of Chemical Education*. 1946;**23**(12):579.

257. Kwon K-Y, Wang E, Chung A, Chang N, Lee S-W. Effect of salinity on hydroxyapatite dissolution studied by atomic force microscopy. *Journal of Physical Chemistry C*. 2009;**113**(9):3369-72.

258. Scheckel KG, Ryan JA. Effects of aging and pH on dissolution kinetics and stability of chloropyromorphite. *Environmental Science & Technology*. 2002;**36**(10):2198-204.

259. Dorozhkin SV. A review on the dissolution models of calcium apatites. *Progress in Crystal Growth and Characterization of Materials*. 2002;**44**(1):45-61.

260. Wu M-S, Higuchi WI, Fox JL, Friedman M. Kinetics and mechanism of hydroxyapatite crystal dissolution in weak acid buffers using the rotating disk method. *Journal of Dental Research*. 1976;**55**(3):496-505.

261. Wu MS, Higuchi WI, Fox JL, Friedman M. Kinetics and mechanism of hydroxyapatite crystal dissolution in weak acid buffers using rotating-disk method. *Journal of Dental Research*. 1976;**55**(3):496-505.

262. Nancollas GH, Sawada K, Schuttringer E. Mineralization reactions involving calcium carbonates and phosphates. In: Westbroek P, de Jong EW, editors. Biomineralization and biological metal accumulation: Springer Netherlands; 1983. p. 155-69.

263. Voegel JC, Frank RM. Stages in dissolution of human enamel crystals in dental-caries. *Calcified Tissue Research*. 1977;**24**(1):19-27.

264. Johnson NW, Poole DFG, Tyler JE. Factors affecting differential dissolution of human enamel in acid and edta - scanning electron microscope study. *Archives of Oral Biology*. 1971;**16**(4):385-94.

265. Qin L, Zhang W, Lu J, Stack AG, Wang L. Direct imaging of nanoscale dissolution of dicalcium phosphate dihydrate by an organic ligand: Concentration matters. *Environmental Science & Technology*. 2013;**47**(23):13365-74.

266. Ma QY, Logan TJ, Traina SJ, Ryan JA. Effects of NO3-, Cl-, F-, SO42-, and CO32- on Pb2+ immobilization by hydroxyapatite. *Environmental Science & Technology*. 1994;**28**(3):408-18.

267. Tanizawa Y, Sawamura K, Suzuki T. Reaction characteristics of dental and synthetic apatites with Fe2 + and Fe3 + ions. *Journal of the Chemical Society, Faraday Transactions*. 1990;**86**(7):1071-5.

268. Martin RD, Beeston MA, Unwin PR, Laing ME. Rotating-disc electrode voltammetry as a probe of adsorption rates on solid particles in liquids - application to zn-ii adsorption at the hydroxyapatite aqueous interface. *Journal of the Chemical Society, Faraday Transactions*. 1994;**90**(20):3109-15.

269. Kwon K-Y, Wang E, Nofal M, Lee S-W. Microscopic study of hydroxyapatite dissolution as affected by fluoride ions. *Langmuir*. 2011;**27**(9):5335-9.

270. Wang X, Klocke A, Mihailova B, Tosheva L, Bismayer U. New insights into structural alteration of enamel apatite induced by citric acid and sodium fluoride solutions. *Journal of Physical Chemistry B*. 2008;**112**(29):8840-8.

271. Loher S, Stark WJ, Maciejewski M, Baiker A, Pratsinis SE, Reichardt D, et al. Fluoro-apatite and calcium phosphate nanoparticles by flame synthesis. *Chemistry of Materials*. 2005;**17**(1):36-42.

272. Honda Y, Anada T, Morimoto S, Shiwaku Y, Suzuki O. Effect of Zn2+ on the physicochemical characteristics of octacalcium phosphate and its hydrolysis into apatitic phases. *Crystal Growth and Design*. 2011;**11**(5):1462-8.

273. Chin KOA, Nancollas GH. Dissolution of fluorapatite. A constant-composition kinetics study. *Langmuir*. 1991;**7**(10):2175-9.

274. Mohammed NR, Mneimne M, Hill RG, Al-Jawad M, Lynch RJM, Anderson P. Physical chemical effects of zinc on in vitro enamel demineralization. *Journal of Dentistry*. 2014;**42**(9):1096-104.

275. Snowden ME, Guell AG, Lai SCS, McKelvey K, Ebejer N, O'Connell MA, et al. Scanning electrochemical cell microscopy: Theory and experiment for quantitative high resolution spatially-resolved voltammetry and simultaneous ion-conductance measurements. *Analytical Chemistry*. 2012;**84**(5):2483-91.

276. McKelvey K, O'Connell MA, Unwin PR. Meniscus confined fabrication of multidimensional conducting polymer nanostructures with scanning electrochemical cell microscopy (seccm). *Chemical Communications*. 2013;**49**(29):2986-8.

277. Kinnear SL, McKelvey K, Snowden ME, Peruffo M, Colburn AW, Unwin PR. Dual-barrel conductance micropipet as a new approach to the study of ionic crystal dissolution kinetics. *Langmuir*. 2013;**29**(50):15565-72.

278. Parker AS, Patel AN, Al Botros R, Snowden ME, McKelvey K, Unwin PR, et al. Measurement of the efficacy of calcium silicate for the protection and repair of dental enamel. *Journal of Dentistry*. 2014; **Supplement 1, 42**(0):S21-S9.

279. Chen C-H, Meadows KE, Cuharuc A, Lai SCS, Unwin PR. High resolution mapping of oxygen reduction reaction kinetics at polycrystalline platinum electrodes. *Physical Chemistry Chemical Physics*. 2014;**16**(34):18545-52.

280. Lide DR. Crc handbook of chemistry and physics, 90th edition: Taylor & Francis; 2009.

281. Brown PW, Constantz B. Hydroxyapatite and related materials: CRC Press; 1994. 317 p.

282. Petersen PE, Bourgeois D, Ogawa H, Estupinan-Day S, Ndiaye C. The global burden of oral diseases and risks to oral health. *Bulletin of The World Health Organization*. 2005;**83**:661-9.

283. Stamm JW. Multi-function toothpastes for better oral health: A behavioural perspective. *International Dental Journal*. 2007;**57**(S5):351-63.

284. Joiner A, Schäfer F, Hornby K, Long M, Evans M, Beasley T, et al. Enhanced enamel benefits from a novel fluoride toothpaste. *International Dental Journal*. 2009;**59**(S4):244-53.

285. Duggal MS, Nikolopoulou A, Tahmassebi JF. The additional effect of ozone in combination with adjunct remineralisation products on inhibition of demineralisation of the dental hard tissues in situ. *Journal of Dentistry*.**40**(11):934-40.

286. Faller RV, Eversole SL, Tzeghai GE. Enamel protection: A comparison of marketed dentifrice performance against dental erosion. *American Journal of Dentistry*. 2011;**24**(4):205-10.

287. Poggio C, Lombardini M, Colombo M, Bianchi S. Impact of two toothpastes on repairing enamel erosion produced by a soft drink: An afm in vitro study. *Journal of Dentistry*. 2010;**38**(11):868-74.

288. Whitford GM, Wasdin JL, Schafer TE, Adair SM. Plaque fluoride concentrations are dependent on plaque calcium concentrations. *Caries Research*. 2002;**36**(4):256-65.

289. Duckworth RM, Morgan SN, Burchell CK. Fluoride in plaque following use of dentifrices containing sodium monofluorophosphate. *Journal of Dental Research*. 1989;**68**(2):130-3.

290. Li L, Pan H, Tao J, Xu X, Mao C, Gu X, et al. Repair of enamel by using hydroxyapatite nanoparticles as the building blocks. *Journal of Materials Chemistry*. 2008;**18**(34):4079-84.

291. Tschoppe P, Zandim DL, Martus P, Kielbassa AM. Enamel and dentine remineralization by nano-hydroxyapatite toothpastes. *Journal of Dentistry*. 2011;**39**(6):430-7.

292. Burwell AK, Litkowski LJ, Greenspan DC. Calcium sodium phosphosilicate (novamin): Remineralization potential. *Advances in Dental Research*. 2009;**21**(1):35-9.

293. Buscemi PJ, Hench LL. Method of bonding a bioglass to metal. Google Patents; 1979.

294. Gendreau L, Barlow APS, Mason SC. Overview of the clinical evidence for the use of novamin in providing relief from the pain of dentin hypersensitivity. *The Journal of clinical dentistry*. 2011;**22**(3):90-5.

295. Litkowski LJ, Quinlan KB, McDonald NJ. Teeth hypersensitivity reduction by a novel bioglass (r) dentifrice. *Journal of Dental Research*. 1998;**77**:199-.

296. Wang Y, Li X, Chang J, Wu C, Deng Y. Effect of tricalcium silicate (Ca3SiO5) bioactive material on reducing enamel demineralization: An in vitro pH-cycling study. *Journal of Dentistry*. 2012;**40**(12):1119-26.

297. Barbour ME, Parker DM, Jandt KD. Enamel dissolution as a function of solution degree of saturation with respect to hydroxyapatite: A nanoindentation study. *Journal of Colloid and Interface Science*. 2003;**265**(1):9-14.

298. Iijima M, Hayashi K, Moriwaki Y. Effects of the Ca2+ and po43- ion flow on the lengthwise growth of octacalcium phosphate in a model system of enamel crystal formation with controlled ionic diffusion. *Journal of Crystal Growth*. 2002;**234**(2-3):539-44.

299. Wang L, Tang R, Bonstein T, Orme CA, Bush PJ, Nancollas GH. A new model for nanoscale enamel dissolution. *The Journal of Physical Chemistry B*. 2004;**109**(2):999-1005.

300. LeGeros RZ. Calcium phosphates in oral biology and medicine: Karger; 1991.

301. Sun Y, Li X, Deng Y, Sun JN, Tao D, Chen H, et al. Mode of action studies on the formation of enamel minerals from a novel toothpaste containing calcium silicate and sodium phosphate salts. *Journal of Dentistry*. 2014;**42, Supplement 1**:S30-S8.

302. Simkiss K, Wilbur KM. Biomineralization: Elsevier; 2012.

303. Nudelman F, Sommerdijk NA. Biomineralization as an inspiration for materials chemistry. *Angewandte Chemie International Edition*. 2012;**51**(27):6582-96.

304. Blagden N, De Matas M, Gavan P, York P. Crystal engineering of active pharmaceutical ingredients to improve solubility and dissolution rates. *Advanced Drug Delivery Reviews*. 2007;**59**(7):617-30.

305. Amjad Z. Mineral scale formation and inhibition: Springer Science & Business Media; 2013.

306. Wang S-S, Xu A-W. Amorphous calcium carbonate stabilized by a flexible biomimetic polymer inspired by marine mussels. *Crystal Growth & Design*. 2013;**13**(5):1937-42.

307. Rodríguez-Navarro AB, Marie P, Nys Y, Hincke MT, Gautron J. Amorphous calcium carbonate controls avian eggshell mineralization: A new paradigm for understanding rapid eggshell calcification. *Journal of Structural Biology*. 2015;**190**(3):291-303.

308. Miyazaki Y, Reimer JD. A new genus and species of octocoral with aragonite calcium-carbonate skeleton (octocorallia, helioporacea) from okinawa, japan. *ZooKeys*. 2015(511):1.

309. Xue X, Penn RL, Leite ER, Huang F, Lin Z. Crystal growth by oriented attachment: Kinetic models and control factors. *CrystEngComm*. 2014;**16**(8):1419-29.

310. Schwahn D, Ma Y, Cölfen H. Mesocrystal to single crystal transformation of d, l-alanine evidenced by small angle neutron scattering. *The Journal of Physical Chemistry C*. 2007;**111**(8):3224-7.

311. Lee I, Han SW, Choi HJ, Kim K. Nanoparticle-directed crystallization of calcium carbonate. *Advanced Materials*. 2001;**13**(21):1617-20.

312. Loste E, Meldrum FC. Control of calcium carbonate morphology by transformation of an amorphous precursor in a constrained volume. *Chemical Communications*. 2001(10):901-2.

313. Loste E, Wilson RM, Seshadri R, Meldrum FC. The role of magnesium in stabilising amorphous calcium carbonate and controlling calcite morphologies. *Journal of Crystal Growth*. 2003;**254**(1):206-18.

314. Gratz AJ, Hillner PE. Poisoning of calcite growth viewed in the atomic force microscope (afm). *Journal of Crystal Growth*. 1993;**129**(3):789-93.

315. Walters DA, Smith BL, Belcher AM, Paloczi GT, Stucky GD, Morse DE, et al. Modification of calcite crystal growth by abalone shell proteins: An atomic force microscope study. *Biophysical Journal*. 1997;**72**(3):1425.

316. Kalb J, Spaepen F, Wuttig M. Atomic force microscopy measurements of crystal nucleation and growth rates in thin films of amorphous te alloys. *Applied Physics Letters*. 2004;**84**(25):5240-2.

317. Rode S, Oyabu N, Kobayashi K, Yamada H, Kühnle A. True atomic-resolution imaging of (1014) calcite in aqueous solution by frequency modulation atomic force microscopy. *Langmuir*. 2009;**25**(5):2850-3.

318. Smeets PJ, Cho KR, Kempen RG, Sommerdijk NA, De Yoreo JJ. Calcium carbonate nucleation driven by ion binding in a biomimetic matrix revealed by in situ electron microscopy. *Nature Materials*. 2015.

319. Kontoyannis CG, Vagenas NV. Calcium carbonate phase analysis using xrd and ft-raman spectroscopy. *Analyst*. 2000;**125**(2):251-5.

320. Wehrmeister U, Jacob D, Soldati A, Loges N, Häger T, Hofmeister W. Amorphous, nanocrystalline and crystalline calcium carbonates in biological materials. *Journal of Raman Spectroscopy*. 2011;**42**(5):926-35.

321. Nehrke G, Poigner H, Wilhelms-Dick D, Brey T, Abele D. Coexistence of three calcium carbonate polymorphs in the shell of the antarctic clam laternula elliptica. *Geochemistry, Geophysics, Geosystems*. 2012;**13**(5).

322. Dickinson SR, McGrath K. Quantitative determination of binary and tertiary calcium carbonate mixtures using powder x-ray diffraction. *Analyst*. 2001;**126**(7):1118-21.

323. Pouget EM, Bomans PH, Goos JA, Frederik PM, Sommerdijk NA. The initial stages of template-controlled CaCO3 formation revealed by cryo-TEM. *Science*. 2009;**323**(5920):1455-8.

324. Pichon BP, Bomans PH, Frederik PM, Sommerdijk NA. A quasi-time-resolved cryotem study of the nucleation of CaCO3 under langmuir monolayers. *Journal of the American Chemical Society*. 2008;**130**(12):4034-40.

325. Quigley D, Rodger PM. Free energy and structure of calcium carbonate nanoparticles during early stages of crystallization. *The Journal of Chemical Physics*. 2008;**128**(22):221101.

326. Edwards MA, German SR, Dick JE, Bard AJ, White HS. High-speed multipass coulter counter with ultrahigh resolution. *ACS Nano*. 2015;**9**(12):12274-82.

327. Yuill EM, Shi W, Poehlman J, Baker LA. Scanning electrospray microscopy with nanopipettes. *Analytical Chemistry*. 2015.

328. Perry D, Paulose Nadappuram B, Momotenko D, Voyias PD, Page A, Tripathi G, et al. Surface charge visualization at viable living cells. *Journal of the American Chemical Society*. 2016.

329. Ivanov AP, Actis P, Jönsson P, Klenerman D, Korchev Y, Edel JB. On-demand delivery of single DNA molecules using nanopipets. *ACS Nano*. 2015;**9**(4):3587-95.

330. Liu S-T, Nancollas GH. The crystal growth of calcium sulfate dihydrate in the presence of additives. *Journal of Colloid and Interface Science*. 1973;**44**(3):422-9.

331. Ceyhan AA, Bulutcu AN. The effect of surface charge and kno 3 additive on the crystallization of potassium chloride. *Journal of Crystal Growth*. 2011;**327**(1):110-6.

332. Salvalaglio M, Vetter T, Giberti F, Mazzotti M, Parrinello M. Uncovering molecular details of urea crystal growth in the presence of additives. *Journal of the American Chemical Society*. 2012;**134**(41):17221-33.

333. Ilevbare GA, Liu H, Edgar KJ, Taylor LS. Impact of polymers on crystal growth rate of structurally diverse compounds from aqueous solution. *Molecular Pharmaceutics*. 2013;**10**(6):2381-93.

334. Ilevbare GA, Liu H, Edgar KJ, Taylor LS. Understanding polymer properties important for crystal growth inhibition impact of chemically diverse polymers on solution crystal growth of ritonavir. *Crystal Growth & Design*. 2012;**12**(6):3133-43.

335. Li X, Gao B, Yue Q, Ma D, Rong H, Zhao P, et al. Effect of six kinds of scale inhibitors on calcium carbonate precipitation in high salinity wastewater at high temperatures. *Journal of Environmental Sciences*. 2015;**29**:124-30.

336. Amjad Z, Koutsoukos PG. Evaluation of maleic acid based polymers as scale inhibitors and dispersants for industrial water applications. *Desalination*. 2014;**335**(1):55-63.

337. Perry D, Momotenko D, Lazenby RA, Kang M, Unwin PR. Characterization of nanopipettes. *Analytical Chemistry*. 2016.

338. Nadappuram BP, McKelvey K, Al Botros R, Colburn AW, Unwin PR. Fabrication and characterization of dual function nanoscale pH-scanning ion conductance microscopy (SICM) probes for high resolution pH mapping. *Analytical Chemistry*. 2013;**85**(17):8070-4.